KANSAS GEOLOGICAL SURVEY
OPEN-FILE REPORT 87-6

SALTWATER INTRUSION INTO ALLUVIAL AQUIFERS: AN EVALUATION OF FIELD METHODS AND GROUND-WATER MODELING TECHNIQUES

By

J. Sadeghipour, P. A. Macfarlane,
C. D. McElwee, and M. W. Kemblowski

Kansas Geological Survey
1930 Constant Avenue
University of Kansas
Lawrence, KS 66047-3726

Saltwater Intrusion into Alluvial Aquifers: An Evaluation of Field Methods and Ground-water Modeling Techniques

by

J. Sadeghipour, P. A. Macfarlane,
C. D. McElwee, and M. W. Kemblowski

Kansas Geological Survey
University of Kansas
Lawrence, Kansas

Open File Report #87-6

March 1987

TABLE OF CONTENTS

LIST OF FIGURES

LIST OF TABLES

Table Page

ACKNOWLEDGMENTS

This research was supported in part by the U.S. Department of the Interior under Grant #14-08-0001-G-1066.

Through this project, graduate assistantships were provided to several graduate students at the University of Kansas who also contributed to the implementation of the ideas presented here. In particular, Mr. Gary Costanzo in his capacity as a graduate research assistant was instrumental in the field collection of hydrogeologic data.

Our special appreciation goes to Pam Wright who patiently typed several versions of this report. The efforts of the Graphic Arts Section of the Kansas Geological Survey and, in particular, Renate Hensiek and Wanda Heberling in their preparation of the figures are greatly appreciated.

EXECUTIVE SUMMARY

The encroachment of saltwater into freshwater formations and eventually into surface waters is the major natural cause of water pollution in the Smoky Hill River in north-central Kansas. The Smoky Hill River valley aquifer system consists of a shallow freshwater layer underlain by an aquitard referred to as the Wellington Formation and a bedrock aquifer consisting of the Herrington Member of the Nolans Limestone. The alluvial aquifer contains a fining-upward sequence of alluvial sediments that range in texture from coarse sands and gravels to silt and clay. The Wellington Formation consists of fractured and weathered Wellington shales. The bedrock units in the Herrington Member of the Nolans Limestone consist mainly of fractured and solutioned gypsiferous dolomites and dolomitic shales.

Recharge to the alluvial aquifer comes from: (1) precipitation falling to the land surface and percolating through the unsaturated zone to the water table, (2) lateral infiltration from the Smoky Hill River when streamflow is high, and (3) vertical leakage through the Wellington shales from the bedrock formations. Discharge from the alluvial aquifer is to the stream under most streamflow conditions and into the bedrock during floods and high-flows.

Shallow ground waters occur in the alluvial and terrace deposits of the Smoky Hill River valley under unconfined (water-table) conditions. The chemical quality of ground water from the alluvial and terrace deposits varies widely and depends on the spatial distribution and relative amounts of recharge to these deposits from precipitation and bedrock sources. The high chloride ground waters are generally found near the base of the alluvial aquifer. The saline waters have resulted from natural dissolution of salt and gypsum units in the deep bedrock formations. The saline ground waters have

moved upward through conduits created by fracturing of the shales and solution cavities in the bedded evaporites in the Wellington Formation.

Detailed field investigation of the saltwater-intrusion process was conducted at a site located in the Smoky Hill River valley near the town of Solomon along a six-mile reach of the stream. Fluid pressures, stream levels and water-table elevations were measured at a network of monitoring sites to determine the ground-water flow conditions. For the most part, ground water discharges to the stream at the field site except during floods and high-flows, when high stream stage results in the reversal of hydraulic gradient and recharge of the aquifer. The slope of water table near the river is determined to be steeper on the west bank than on the east bank. This asymmetry results because the stream is perpendicular to the regional flow directions. West of the river the ground-water flow pattern is distinctly affected by the heterogeneity of the sediments. Due to the high permeability of the sands and gravels, the aquifer responds rather quickly to the rise of the stream stage. The recovery of the aquifer to the pre-flood condition is slower, however, mainly because the aquifer continues to be affected by the residual recharge from percolation of precipitation after the stream stage has declined.

The shape and configuration of the saltwater-dispersive zone at the field site is very much influenced by the temporal changes in the stream-aquifer conditions. These changes may result from variations in stream discharge or may be caused by the water-table rise due to increased natural ground-water recharge. The whole spectrum of the saltwater-intrusion zone and its response to the stream-aquifer conditions was determined by frequent observations of the stream stage, water-table elevations and the saltwater-intrusion zone. Generally, the top of the saltwater-intrusion zone is located on the east side of the river, asymmetrical with respect to the center line of the river. The thickness of the saltwater-dispersive zone, assumed to be the area between the 2,000 and 100,000 ppm total dissolved solids (TDS) lines, is approximately 15 to 20 ft during low streamflow conditions. Farther from the river, the dispersive zone shrinks down to a narrow strip which can be regarded as a sharp interface. During high flows, the top of the dispersive zone is depressed and the extent of the saltwater-intrusion zone is reduced.

Monitoring saltwater upconing at the field site was achieved with the use of borehole geophysical logging, collection and analysis of chemical quality samples and a new differential-pressure method. The differential-pressure method proposed in this study uses a pressure transducer to measure pressure differentials over a series of small intervals in the continuously screened wells. The vertical ground-water density variation is then computed from the pressure differentials and converted into TDS, provided the relationship between ground-water density and TDS is known.

Among the techniques utilized for saltwater-intrusion zone monitoring, the geophysical and the differential-pressure methods are less costly and easier to implement than the chemical-quality analysis. Generally, the analysis of chemical-quality samples, while providing more reliable results, requires a considerable amount of laboratory work and also results only in point estimates of chemical characteristics. For a sharp saltwater-freshwater contact zone, the location of the interface may fall in between the two distant sampling points and, therefore, may not be detected by the results of chemical-quality sampling. The borehole geophysical techniques have some drawbacks also. For instance, the logging tool may not be sensitive enough to detect small changes in the fluid resistivity. Similarly, a disadvantage of the differential-pressure method may be the inability of recognizing small changes in pressure associated with small changes in fluid density.

In general, depending on the nature of the saltwater-intrusion problem being investigated and the level of accuracy required, one of the techniques mentioned above may be more effective than the others. The choice of which technique to use can be made after utilizing a combination of these techniques during the initial stages of the project and comparing the results.

Other field activities include a number of slug tests to determine the hydraulic-conductivity variation along the field cross section and geoelectric surveys to determine the lateral extent of the saltwater upconing. The hydraulic-conductivity estimates vary widely over the field cross section and are shown to be log-normally distributed. The results of the surface geoelectric surveys indicate two areas where saline waters can be detected at shallow depths. One body of saltwater parallels the course of the river and then crosses the river near the line of monitoring sites. The second body of saline water is characterized by a north-south-trending area of low apparent resistivities east of the river. The results of the apparent resistivity surveys were confirmed by the differential-pressure measurements.

Modeling saltwater intrusion in ground water requires, in an ideal case, incorporating the effects of complicated physiochemical processes, the complete description of which may not be mathematically tractable. To reduce complexity of the problem, in practice, saltwater and freshwater are commonly assumed to be immiscible fluids separated by a sharp interface. Accordingly, the potential-flow theory can be applied to the saltwater zone and freshwater zone separately requiring also that the pressure and flux be continuous across the interface boundary. Incorporation of the interface-boundary condition,

the most difficult task of a sharp interface model, can be achieved with relative ease using the technique of boundary-element method.

To solve the interface-upconing problem, this study proposes a new implicit approximation of the interface-motion equation combined with the boundary-element solution of the freshwater- and saltwater-continuity equations. The proposed model does not use the Dupuit approximation, thus providing better results for the cases in which the vertical component of the flow is significant. The model is capable of handling steady, unsteady, stable and unstable saltwater for upconing problems. The model results were confirmed with the experimental results of a problem of saltwater upconing under a drain. Note that because of the assumption of a sharp interface, the model is applicable only to situations characterized with a narrow dispersive zone. In alluvial aquifers, this assumption is usually not satisfied in the close vicinity of the river channel where fluctuations in the stream stage tend to extend the dispersive zone over large areas.

We investigated the impact of the Dupuit-Forchheimer approximation on the saltwater-upconing simulations. Our analysis indicates that if the sinks and sources are of a vertical size comparable with the thickness of the freshwater zone, the location of the interface calculated by the "Dupuit" model will give satisfactory results, even though a strong vertical flow may exist in some regions. However, when the size of the sink is small compared to the thickness of the freshwater zone, the Dupuit approximation may cause substantial errors in the estimation of the interface motion.

An attempt was made to make a simplified description of the dispersive zone using the concept of boundary-layer approximation. The simplification involves dividing the aquifer domain into three separate zones, namely, a freshwater zone, a transition (dispersive) zone and a saltwater zone. The concentration in the transition zone varies from that of the saltwater at the bottom to that of the freshwater at the top. The flow in each zone is assumed to be described by the Dupuit-Forchheimer approximation. Based on this approximation, the pertinent governing equations were derived and solved numerically with the use of finite-difference technique. Application of the model to a cross section of the Smoky Hill River valley verifies the occurrence of unstable upconing at this site. The results of model simulations indicate that advective transport is the predominant saltwater-upconing mechanism in this case.

In reality, saltwater and freshwater are miscible fluids and can become mixed and distributed in a dispersive zone of variable salinity. A complete mathematical description of a miscible flow system is obtained by the coupled equations of the fluid continuity, Darcy velocity, solute transport and a constitutive equation relating fluid density to the salt concentration. The solution of these equations as achieved with the use of an efficient finite-element model. The proposed model preserves the continuity of the velocity field across the elemental boundaries and results in accurate estimates of velocities that are extremely important in simulation of advective-dominated transport problems. The model was applied to a saltwater-intrusion problem and its results were confirmed with available analytical and numerical solutions. Application of the model to the field problems may encounter difficulty mainly because of the lack of sufficient data and also because of the poorly defined transport theory in complex hydrogeologic environments.

1. INTRODUCTION

1.1 Significance of Work

The encroachment of saltwater into freshwater formations, and eventually into surface waters, is the major natural cause of water pollution in many areas of the United States. The intrusion of saltwater may be accelerated or decreased by applying various stresses to the system (deepening a river course, irrigation pumping, saltwater pumping, etc.). Although the literature contains considerable documentation and analysis of these problems in oil reservoirs and coastal aquifers, very little effort has been directed toward studying the mechanism of saltwater encroachment in alluvial-valley systems. Evaluation and testing of appropriate mathematical models and associated numerical codes, along with analysis of field data, would extend the knowledge and understanding of the saltwater-encroachment phenomenon and result in creation of efficient numerical techniques for the prediction of the saltwater intrusion.

1.2 Scope of the Study

The principal objectives of the project were: (1) to conduct a comprehensive field investigation of saltwater intrusion in an alluvial-aquifer system, and (2) to evaluate the suitability of mathematical models for prediction of the location, extent and severity of the naturally occurring saltwater intrusion in alluvial-aquifer systems.

The field investigation involves characterizing in a detailed manner the hydrogeology and chemical quality of ground waters in the alluvial and underlying bedrock formations at a selected field site. Furthermore, the suitability of several hydrogeologic and geophysical techniques for monitoring saline ground waters were evaluated on the basis of their field performance.

From analysis of the field investigation, an integrated field approach was suggested for studying saltwater-intrusion occurrence in stream-aquifer systems.

To achieve the second objective, several computer models including a sharp-interface model, an approximate transition-zone model and a density-dependent solute-transport model were developed and tested on an actual aquifer and realistically designed hypothetical examples. Because sharp-interface models are frequently based on the Dupuit assumption, we will also establish under what circumstances the Dupuit approximation is acceptable and what corrections should be made to account for the vertical component of flow in the vicinity of partially penetrating sinks and sources.

1.3 Field Investigations

As indicated before, the primary purpose of the field investigation is to provide actual observations on saltwater-intrusion occurrence in a stream-aquifer system. The site chosen for this analysis is located in the Smoky Hill River valley along a six-mile reach of the stream. Previous investigations of the area by the U.S. Geological Survey and the Kansas Water Office demonstrated that saltwater intrusion was a major cause of water-quality degradation in the Smoky Hill River.

During the course of the field investigation, special attention was given to the consideration of the following factors: source of the saltwater, the hydrogeological structure of the intrusion area, and the governing physical mechanisms of the intrusion process. These factors are to some extent interdependent; for example the hydrogeological structure influences the way the saltwater flows towards a river. Therefore, the field data must be collected such that the importance of these factors is clearly reflected by the field observations. This task may be accomplished with relative ease, since the area of saltwater upconing is usually limited to a narrow corridor along a river. Thus, the areal extent of the problem is relatively small. Due to the nature of the problem, mainly the vertical variations of the density and pressure, vertical averages of investigated quantities do not contain sufficient information about the system. For that reason the observation network was designed in a way which provides information about the vertical and areal distribution of the important quantities. These quantities are a) pressure, which is the governing force of ground-water flow; b) density, which contributes to the flow potential and is related to the concentration; c) sodium-chloride concentration, whose distrituion indicates the location of the saltwater and freshwater zones and the transition zone between them; and d) ground-water free-surface elevation. These quantities were measured directly or indirectly in the network of well nests, thus providing information about their spatial and time distributions.

In order to estimate the amount of the salt entering the river, the seepage rate and the concentration of the inflowing fluids must be measured along the river course in the intrusion area. These measurements were obtained using seepage runs and water-quality sampling.

Our field investigation also involves using a combination of hydrogeologic and geophysical techniques along with data from a monitoring-network design to develop a three-dimensional view of the saltwater-intrusion area. A cursory examination of the literature indicates that field investigations of this type usually involve intensive drilling and monitoring programs. It will be shown, however, that a judicious design of the monitoring network combined with existing techniques can significantly reduce the need of these large-scale projects without sacrificing the goals of an overall monitoring program.

1.4 Saltwater-intrusion Modeling

The modeling of the saltwater-intrusion mechanism, which will follow the field data-collection phase, is quite complicated in itself. The governing forces of this phenomenon are: a) the convergent flow of ground water towards the river, which "pulls up" the saltwater in the direction of the flow, b) gravity, which "pulls down" the saltwater because of its higher specific weight, and c) hydrodynamic dispersion, which causes the mixing and spreading of particles from higher to lower concentrations.

The model, which includes all these factors, and that perhaps best describes the problem is the hydrodynamic dispersion - ground-water-flow model with variable density. Unfortunately, the equations of this model are difficult to solve. However, if we assume that the transition zone is relatively narrow, we can simplify the problem using the sharp-interface cross sectional model. The equations of the sharp-interface model can be solved relatively accurately with the use of numerical techniques.

One can go further and assume that the Dupuit approximation is acceptable in the analysis of this problem, i.e. that the ground-water flow is basically horizontal and the vertical component is negligible. This assumption has been used for simulating sea-water intrusion. The impact of these assumptions may be to some extent evaluated by comparison of simulation results with field measurements.

Although the original intent of the project was to concentrate on evaluation of sharp-interface saltwater-intrusion models, during the field investigation it became apparent that the contacting zone between freshwater and saltwater was not sharp. Rather a thick dispersive (or transition) zone existed beneath the Smoky Hill River in the alluvial aquifer. This observation lead us to the development of two additional models that take into consideration the effects of dispersion.

The first model uses an approximate description of the transition zone in terms of a boundary-layer approach. The mathematical formulation and numerical solution procedure associated with this approach are developed and applied to a situation typical of the Smoky Hill River cross section.

The second model is based on simultaneous solution of the ground-water flow and solute-transport equations in a variable density miscible-flow system. This model represents the most complete mathematical description of a saltwater/freshwater system. The usefulness of this model will also be demonstrated with several examples.

As indicated above, the modeling of saltwater intrusion presented in this report will cover a wide range of models from a sharp-interface approach and a transition-zone approximation to a complete description of the ground-water system with a density-dependent solute-transport model.

1.5 Contents of the Report

The results of our research on saltwater-intrusion field procedures and modeling techniques are presented in this report and divided into two parts. The first part, Sections 2 through 6, deals exclusively with the field investigation at the Smoky Hill River cross section in north-central Kansas. In this part we evaluate the effectiveness of several different field measurement techniques that can be used for detection of the saltwater-intrusion zone. Major findings from the field investigation are summarized at the end of Section 6.

Section 7 starts the discussion on mathematical modeling of the saltwater intrusion by introducing first, the commonly used sharp-interface approach; and then, the more rigorous but also more realistic, miscible-flow approach. In Section 8, a new implicit approximation of the sharp-interface motion equation is developed with the use of the boundary-element method. In dealing with the sharp-interface approximation, Section 9 establishes under what circumstances the Dupuit-Forchheimer approximation is acceptable and how the errors due to its use may be corrected. In Section 10, the concepts of the boundary-layer approximation and potential-flow theory are combined for the development of a simplified description of the dispersive zone. Finally, in Section 11 a density-dependent solute-transport model is developed to analyze situations characterized with a relatively wide dispersive zone.

Appendices A and B contain the chemical-quality data collected in the field and the description of the geologic units at the field cross section.

2. PREVIOUS RELATED WORK

Before proceeding to describe the detailed field investigation performed at the Smoky Hill River valley, it is imperative to discuss several previous studies that also dealt with saltwater-intrusion problems. In particular, the studies conducted in the vicinity of the Smoky Hill River serve as guides for selection of an appropriate field site and also greatly influence the design of the monitoring network.

2.1 Previous field investigations of saltwater intrusion - a Review and Evaluation of Field Methods

Field investigations of saltwater intrusion have been conducted in many coastal freshwater aquifers and stream/aquifer systems throughout the world. Most of these studies have relied on using hydrologic and geochemical data collected from networks of piezometers. Typcially, ground-water chemical-quality data and bottom-hole pressures are used to develop an understanding of the hydrogeology of the saltwater-intrusion area and to describe the transient changes in the nature of the intrusion zone. Several examples of the field investigations are worth mentioning here.

Saltwater intrusion into the Biscayne aquifer of southeastern Florida was extensively studied by Kohout (1960). In this study a network of monitoring sites were installed along two selected cross sections of the aquifer to define the shape and extent of the saltwater intrusion into the freshwater aquifer. Each monitoring site consisted of two to 12 piezometers screened at various levels in the approximately 110-ft-thick carbonate aquifer. From the field observations, Kohout (1960) found that the saltwater front was dynamically stable at a point seaward of a position predicted by the Ghyben-Herzberg relation. General flow directions in the Biscayne aquifer were determined based on the distribution of hydraulic head as defined by Lusczynski (1961). The variation of chloride concentration along the cross sections verified that due to the dispersion effects, a relatively thick transition zone separates the fresh and saline waters in this aquifer.

The natural discharge of saline ground waters into stream/aquifer systems of the Great Bend Prairie of Kansas was studied by Cobb (1980). He utilized existing data and data from a ground-water chemical-quality network of piezometers constructed during his study to identify areas in the shallow freshwater aquifer and in the bedrock aquifers of the Lower Permian where saline ground waters were present. Each monitoring site in the network consisted of three piezometers screened at various intervals in the shallow and bedrock aquifers. Cobb (1980) found that saltwater remained near the bedrock surface in the alluvial aquifer except near major gaining streams where low-quality ground waters are present at shallow depths beneath the stream bottom. Concentration profiles along several cross sections of the alluvial aquifer prepared from an analysis of water samples in the study area indicated that a relatively wide transition zone existed at the contact of fresh and saline ground waters. The direction of vertical-flow components between nearby piezometers in the alluvial and bedrock aquifers was determined by the method of McElwee and Macfarlane (1980).

Benz et al. (1961) investigated an occurrence of saline ground water in the Red River valley of North Dakota and found that salt-affected areas consistently had a high water table, poor drainage conditions, and saline artesian waters. Similar chemical composition of shallow waters in the glacial drift and deeper artesian waters indicated to the authors that waters from the Dakota Formation were the primary source of salt. Upward vertical-flow gradients were found in the shallow alluvial aquifer by comparing the static water levels of four piezometers installed at different depths at three monitoring sites. The total dissolved solids of ground waters in the alluvium were found to range from 2900 to 31,000 ppm.

More recently, borehole and surface geophysical methods have been used for mapping variations of ground-water chemical quality and for monitoring saltwater-intrusion areas. Borehole methods are attractive because measurements can be made continuously in the portion of the aquifer penetrated by the borehole and because the need for geochemical analysis of water samples is minimized. These advantages significantly reduce the costs of monitoring saltwater-intruded areas. However, Rushton (1980) and Kohout (1980) have shown that the freshwater/saltwater transition zone in an open borehole does not always coincide with the transition zone in the aquifer. This discrepency is usually seen in low-permeability aquifers with a significant vertical component of hydraulic gradient in the saltwater zone. Under such conditions the open borehole "short circuits the head difference and water laterally enters the deep part of the hole and flows vertically up the borehole and discharges in the shallow part of the hole" (p. 192; Kohout, 1980). To alleviate this problem, Tellam et al. (1986) made conductivity measurements on pore waters of core samples collected during drilling to develop fluid-conductivity profiles of the bedrock aquifer at several sites. Because core samples are collected only once, continuous or future saltwater monitoring will not be possible using this techique.

The use of bulk formation resistivity measurements from borehole logging for detection of saltwater may be problematic in that the measurements are only empirically related to the resistivity of the pore waters through Archie's Law (Doveton, 1986). Because bulk resistivity is also affected by the presence of conducting minerals such as clay, the relationship between bulk resistivity and ground-water chemical quality must be defined and carefully evaluated on a site-by-site basis.

Surface geophysical techniques, principally direct-current resistivity and electromagnetic methods, have been used to map the lateral extent of saltwater-intrusion zones. These methods have had varying degrees of success and are usually applied along with other means of developing hydrogeologic information in the field. The results of surveys conducted in the Netherlands have been summarized by Van Dam and Muelenkamp (1967). They found that bulk resistivity is closely related to ground-water chemical quality. They were able to compute calibration curves to estimate ground-water salinity in sandy deposits. In a similar study Lazrey (1972) evaluated the effectiveness of resistivity profiling, resistivity sounding and induced-polarization techniques as tools for delineating saltwater-intrusion areas in New Brunswick, Canada. He concluded that saltwater intrusion into sandstones could be easily detected by resistivity profiling because of a large contrast between saltwater- and freshwater-saturated sediments. In contrast, some shaley formations were found to have resistivities as low as the saltwater-saturated sandstones. He found that induced-polarization soundings helped to differentiate between saltwater-saturated sandstones and shaley formations. More closely related to the present investigation, Zohdy and Jackson (1973) evaluated the usefulness of direct-current resistivity methods in the recognition of natural brines and determination of depth to a freshwater/saltwater interface in a complex geologic system consisting of interbedded Permian shales, sandstones and evaporites. They interpreted the vertical electrical soundings by curve matching and automatic interpretation methods and concluded that the resistivity method is useful where the freshwater/saltwater interface lies above the gypsum in the subsurface and where the effective relative conductance of the brine-saturated layers below the gypsum is large. In areas where high-resistivity anhydrite beds lie directly beneath the interface, the exact location of the interface was difficult to detect. In addition alternating beds of shale and dolomite were found to show the presence of brine because of the alternations of very low and very high resistivity. Macfarlane and Ackerman (1983) used vertical electrical sounding techniques to map the top of the freshwater/saltwater interface beneath two lines of soundings in the Great Bend Prairie of Kansas. They demonstrated that upconing is taking place beneath Rattle Snake Creek at two locations within the study area. In this study, the top of the interface, was identified from the interpreted vertical electrical soundings and ground-water chemical-quality data. The position of the interface was easily determined in the shallow subsurface but could not be distinguished from the Permian shale bedrock beneath the aquifer where the thickness of saltwater near the bottom of the unconsolidated sediments is small.

2.2 Previous Field Investigations in the Vicinity of the Study Area

The regional geologic setting and ground water in the Smoky Hill River valley has been studied by Latta (1949). He found a wide variation in ground-water chemical quality in the alluvial aquifer in the vicinity of the field site. Chloride concentrations in excess of 10,000 ppm were recorded in some of the ground water samples collected by Latta (1949). The saline brines are found mostly in the deeper parts of the alluvial aquifer. The saline waters were resulting from the dissolution of evaporites in the underlying Wellington Formation.

Gogel (1981) reported on the discharge of saltwater from the Permian Wellington Formation into freshwater aquifers and streams in central Kansas. Infiltration of freshwater primarily from overlying unconsolidated deposits has dissolved salt and evaporite deposits in the Wellington Formation resulting in the formation of a discontinuous zone of solution cavities and collapsed beds containing large quantities of saltwater. This zone within the Wellington Formation has been named the Wellington aquifer by Gogel (1981). As a part of the field investigation, Gogel (1981) installed a series of single piezometers screened in the Wellington aquifer to determine lateral ground-water flow direction. Additionally, seepage and salinity measurements were made in several streams in central Kansas to locate the areas affected by saltwater inflow from the Wellington aquifer. Gogel (1981) found that there is hydraulic connection between the underlying Wellington aquifer and the overlying stream/aquifer systems in the Solomon-New Cambria area in the Smoky Hill River valley. In this area, the potentiometric surface of the Wellington aquifer is higher than the water table in the alluvial aquifer and therefore, saltwater discharges through fractures and sink holes in the overlying shale to the alluvial aquifer.

Gillespie and Hargadine (1981) performed a further field investigation of the saltwater discharge from the Wellington aquifer to the stream/aquifer system between Salina and Abilene, Kansas. During this field investigation which was conducted on an areal basis, a monitoring network of piezometers was established in the Wellington aquifer, the bedrock aquifer in the Herrington Member of the Nolans Limestone, and lower part of the alluvial aquifer. The brine from the Wellington aquifer was indicated to be moving up through a leaky confining layer beneath the alluvial aquifer through fractures and collapsed structures. The brine-discharge rate through the leaky confining layer was estimated to range from 0.3 to 0.8 cfs. Gillespie and Hargadine (1981) reported that the chloride concentration of the Smoky Hill River increased approximately 800 mg/L between New Cambria and Sand Springs at base-flow condition during 1976-77.

Additionally, Gillespie and Hargadine (1981) installed a line of continuously screened wells in the alluvial aquifer in the vicinity of the river to observe saltwater upconing beneath the Smoky Hill River at a specific site. The site was chosen after these investigators conducted a series of seepage and salinity surveys in the reach of the river near their proposed area of the detailed study. At this location chloride in the surface waters increases rapidly at base-flow conditions. A borehole fluid-conductivity logger was used to show variations in ground-water chemical quality and to outline the saltwater-intrusion zone on the west side of the river. The results of the surveys showed that upconing was taking place in the alluvial aquifer.

3. LOCATION AND HYDROGEOLGOIC SETTING OF THE FIELD SITE

3.1 Geographic Location of the Field Site and Major Features

The field site is located in the Smoky Hill River valley near the western edge of the Flint Hills physiographic province and upstream from the confluence with the Solomon River (Schoewe, 1949). Figure 3.1 shows the geographic location of the study area. The boundary between Saline and Dickinson counties extends in a north-south direction through the field site. The town of Solomon, Kansas, is located north of the site. The valley of the Smoky Hill River is approximately 1.5 miles wide and the river occupies the center of the valley and meanders considerably. The valley is relatively flat except for old meander scars and terraces. Low bluffs composed of Lower Permian bedrock (Wellington Formation) flank the valley sides. The Solomon River joins the Smoky Hill River less than 0.5 mile downstream from the northern edge of the field site. The field site covers approximately 1.4 mi^2 (3.6 km^2) of the valley on the east and west banks of the river (at the location the river is oriented north-south).

3.2 Regional Geology

Rocks of Lower Cretaceous sand and Lower Permian age crop out in the upland areas outside and underlie the Smoky Hill River valley in the vicinity of the field site and the surrounding area (Figure 3.1). Rock units of the Chase and Sumner groups are represented in western Dickinson and eastern Saline counties. These near-surface units are from oldest to youngest: the Herrington Member of the Nolans Limestone and the Wellington Formation.

The Herrington Member of the Nolans Limestone crops out in the low bluffs that flank the Smoky Hill River valley south and east of Abilene. This unit is in the subsurface beneath the field site at Solomon. At the surface the

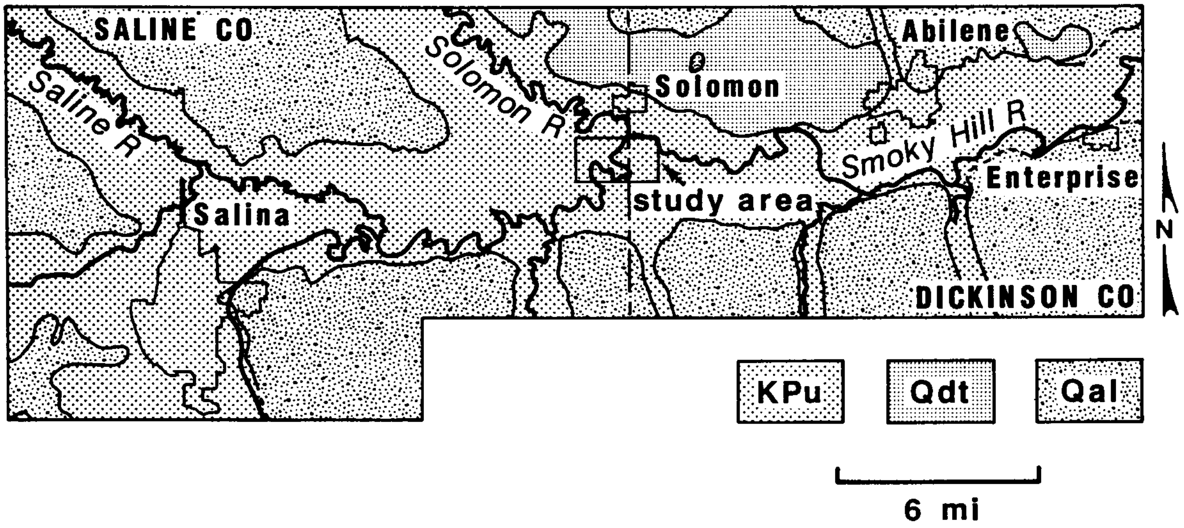

Figure 3.1 Location and surface geology of the Smoky Hill River Valley near the study area.

Herrington consists of bedded yellowish-tan to gray fossiliferous dolomitic limestone and thin interbedded tan shales. Samples of the limestone from the near surface frequently contain nodes partially or completely filled with quartz or contain small cavities ranging in size from 0.5-inches (1.25-cm) diameter to pinpoint size. These cavities are generally abundant and give the rock a very porous appearance. Bedding in the limestone beds is indicated by fossiliferous and nonfossiliferous zones and distributed zones of solution cavities and coloration along planes parallel to the bounding surfaces of the limestone beds. Fossil mollusks and other fossil debris are common. Total thickness on the outcrop ranges from 6 to 10 feet.

The Wellington Formation crops out in the valley walls and hills of the Smoky Hill River valley in eastern Saline and western Dickinson counties and underlies the alluvium at the field site. The Wellington Formation, due to its primary lithology, is poorly exposed in road ditches and isolated road cuts in the vicinity of the field site. The Wellington consists primarily of gray to tan shale and in the near surface contains extensive box-work structures and cemented sand-filled joints and cavities. Weathering at the surface frequently erodes the shale leaving the box-work structures and calcite-filled geodes. Joints are often filled with calcite-cemented medium- to coarse-grained sand and gravel. The gravels range up to 0.5 inches (1.25 cm) in size. These fillings may be associated with the Pleistocene-age Abilene conglomerate (Zeller, 1968). Good exposures of these sand-filled joints are located in a road cut at the west edge of Abilene in SW 1/4, SW 1/4, sec. 9, T. 13 S., R. 2 E. The Wellington also contains thick to thin discontinous zones of evaporites and dolomitic limestone; these are generally not found in surface exposures. To the west of the field site in the Saline area, the Wellington has been subdivided into a lower unnamed member, the Hutchinson salt, and an upper unnamed member (Gillespie and Hargadine, 1981; Gogel, 1981).

Pleistocene and Recent age unconsolidated deposits can be found in the Smoky Hill River valley and in the upland areas outside of the valley in eastern Saline and western Dickinson counties. These deposits include undifferentiated alluvial and terrace deposits and dune sands. The alluvium and terrace deposits consist of variable thicknesses of gravel, sand, silt and clay in a fining-upward sequence. Occasionally, the sands and gravels at the base of the alluvium are cemented with calcium carbonate. Thin patches of cemented Abilene conglomerate were found during this investigation in upland areas south of the Smoky Hill River and west of Abilene. An extensive area of dune sand is located between Solomon and Abilene north of the river valley. These deposits, described by Latta (1949), consist of fine to medium eolian quartz sand overlying terrace deposits. Thicknesses range from featheredge at the extremities to 15 feet.

3.3 Regional Ground-water Conditions

Regional ground-water conditions in the Wellington Formation and the alluvial aquifer of the Smoky Hill River valley are described here to fully understand the cause of the saltwater occurrence in and around the field site.

3.3.1 The Wellington Aquifer

The Wellington aquifer consists of fractured shales in the Wellington Formation that contain highly saline ground waters (Figure 3.2). The brine-saturated fractured shales have resulted from the solution of salt along the up-dip edge of the Hutchinson Salt Member of the Wellington Formation and subsidence or collapse of the overlying shales. A further development of the aquifer system occurs east of Salina and is caused by the solution of

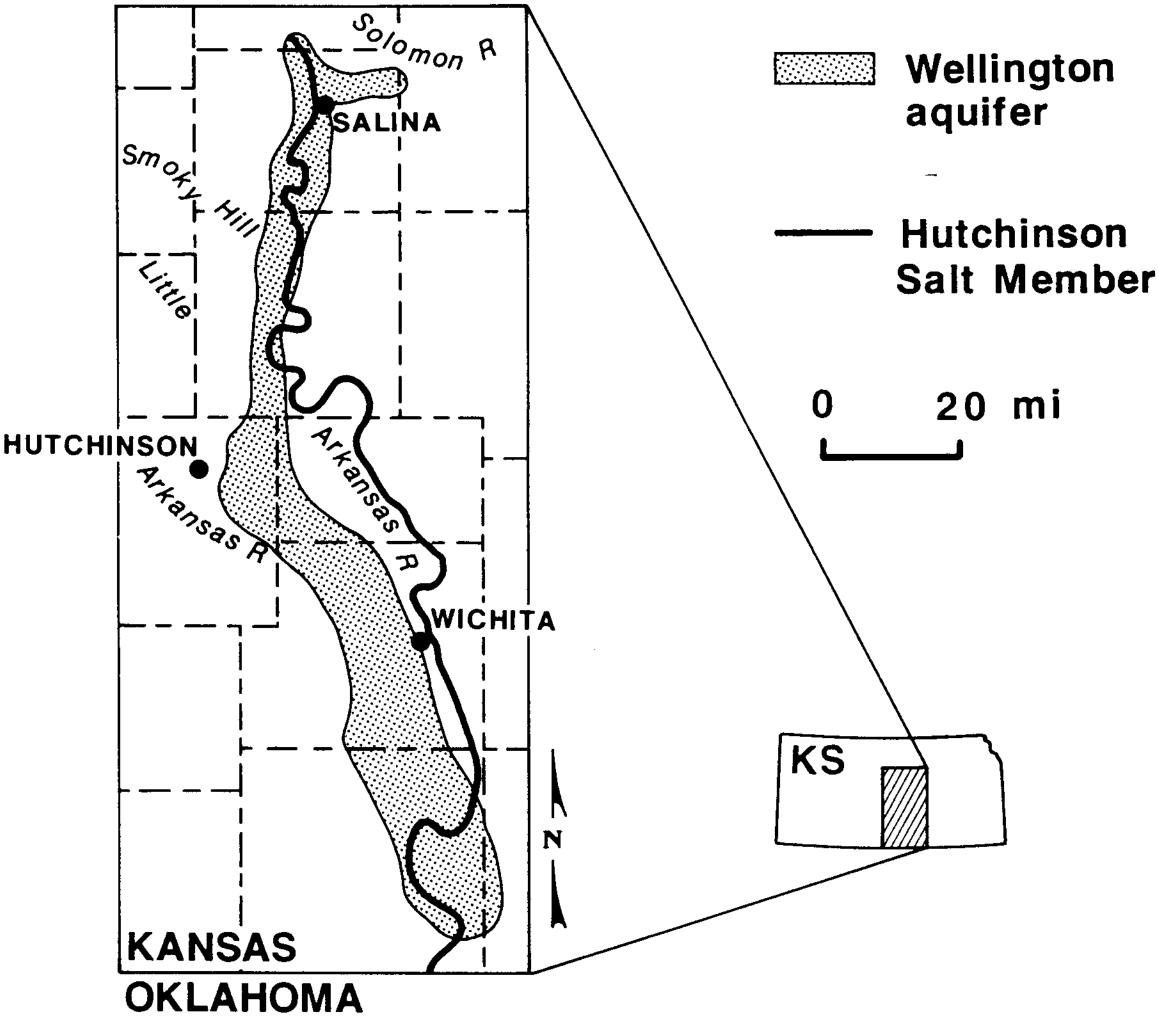

Figure 3.2 Location and extent of the Wellington aquifer in Kansas; after Gogel (1981).

evaporites in the lower part of the Wellington Formation (Figure 3.3). Dissolution of the salt and the evaporites is caused by the movement of shallow ground waters into the fractured Wellington shales.

The bedrock system has been studied extensively by Gogel (1981) and Gillespie and Hargadine (1981). The ground-water flow in the Wellington aquifer is to the north or south away from a potentiometric high located in Reno County, near Hutchinson. Ground waters in the Wellington aquifer move northward or southward through fractured shales to the discharge areas. The discharge points for the Wellington aquifer are located in the Smoky Hill River valley near Solomon and in the Arkansas River valley near Geuda Springs. Gillespie and Hargadine (1981) mapped many collapse fractures associated with the Wellington aquifer in the Solomon area. According to this study, saline ground waters are being discharged to the alluvium through breech points in the confining layer. Ground-water discharge to shallower stream/aquifer systems occurs where the vertical hydraulic gradient is upward from the Wellington aquifer. Gillespie and Hargadine (1981) found that the potentiometric surface (freshwater equivalent) in the Wellington aquifer was higher in elevation than that in the alluvial aquifer east of New Cambria in the Smoky Hill River valley. Gogel (1981) found that total dissolved solids of the ground water in the Wellington aquifer ranged from 70,000 mg/L to 328,000 mg/L for a limited number of samples. Gillespie and Hargadine (1981) found that the chloride concentration of ground waters from the Wellington aquifer ranged from 11,000 to 89,000 mg/L (approximate total dissolved solids range of 20,000 to 162,000 mg/L) in the vicinity of Solomon, Kansas.

3.3.2 The Smoky Hill River Valley Between Salina and Enterprise

Shallow ground waters occur in alluvial and terrace deposits of the Smoky Hill River valley under unconfined (water-table) conditions. Recharge to the

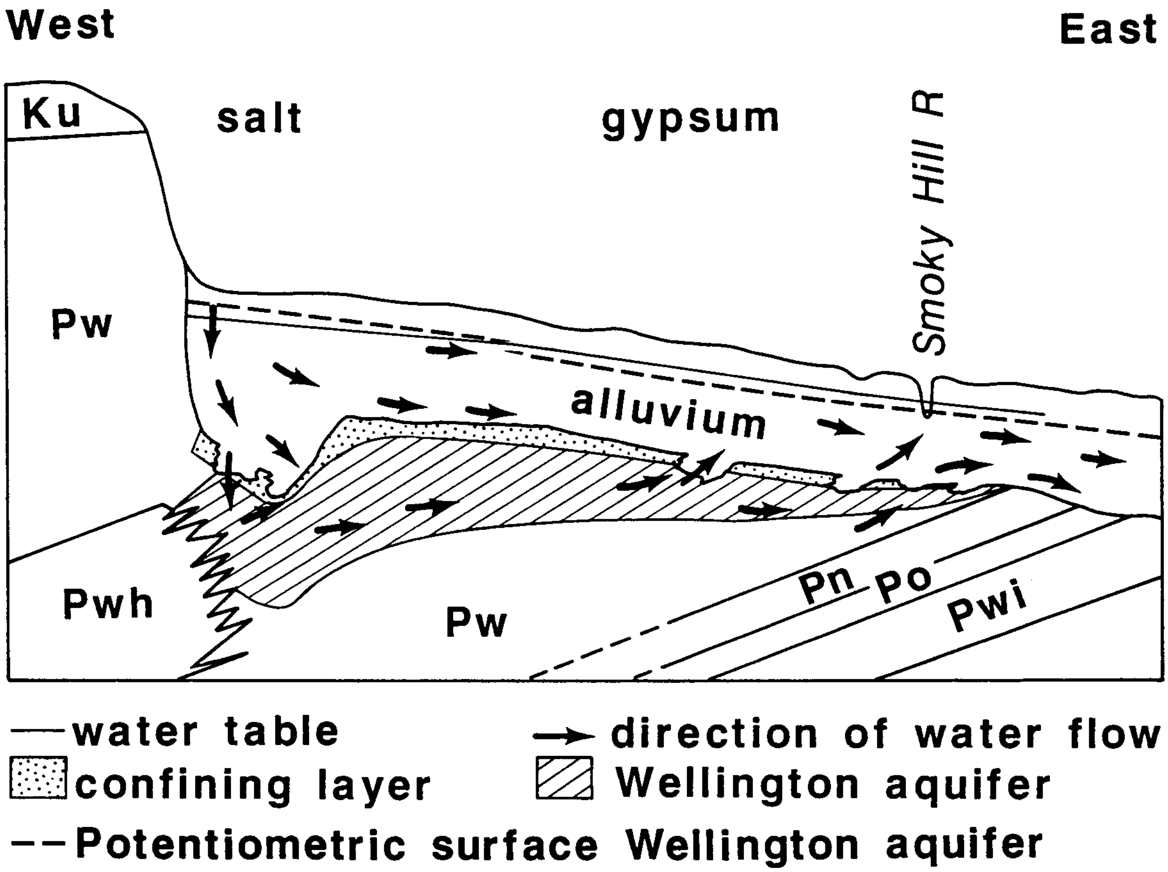

Figure 3.3 Cross-sectional view of the Wellington aquifer in the area between Salina and Solomon showing the groundwater flow pattern; after Gogel (1981).

water-table aquifer comes from precipitation falling on the valley floor and terraces and interactions with the river when the stream is flowing at higher stages. Ground-water movement is generally eastward and toward the river where discharge occurs during low-flow periods. Figure 3.4 shows the configuration of the water table for May 1984. The saturated thickness of the alluvial and terrace deposits ranges from featheredge near the valley extremities to as much as 40 feet near the axial portion of the valley.

The chemical quality of ground water from the alluvial and terrace deposits varies widely and depends on the spatial distribution and relative amounts of recharge to these deposits from precipitation and bedrock sources (Latta, 1949; Gillespie and Hargadine, 1981; and Whittemore et al., 1981). Low total dissolved solids Ca-HCO_3-type waters have originated from precipitation. Those waters that have been affected by halite and evaporite solution contain high concentrations of total dissolved solids, chloride and sulfate. These brines do not seem to have been produced from oil-field operations.

Low total dissolved solids Ca-HCO_3 or mixed-cation-mixed-anion-type ground waters are commonly found in the alluvial aquifer between Enterprise and Abilene, Salina to New Cambria, and in the sand-dune-covered terrace deposits between Solomon and Abilene. Chloride and sulfate concentrations of ground-water samples from these areas range from less than 100 to 1900 mg/L and less than 100 to 500 mg/L, respectively. Ground-water samples containing chloride and sulfate concentrations near the upper end of dissolved solids range have probably resulted from some mixing with ground waters that have been affected by halite and evaporite solution. Ground waters from the terrace deposits are generally low total dissolved solids Ca-HCO_3-type waters. Ground waters in the alluvial aquifer near these terrace deposits in the vicinity of Sand Springs are Ca-HCO_3-type waters, generally low in total dis-

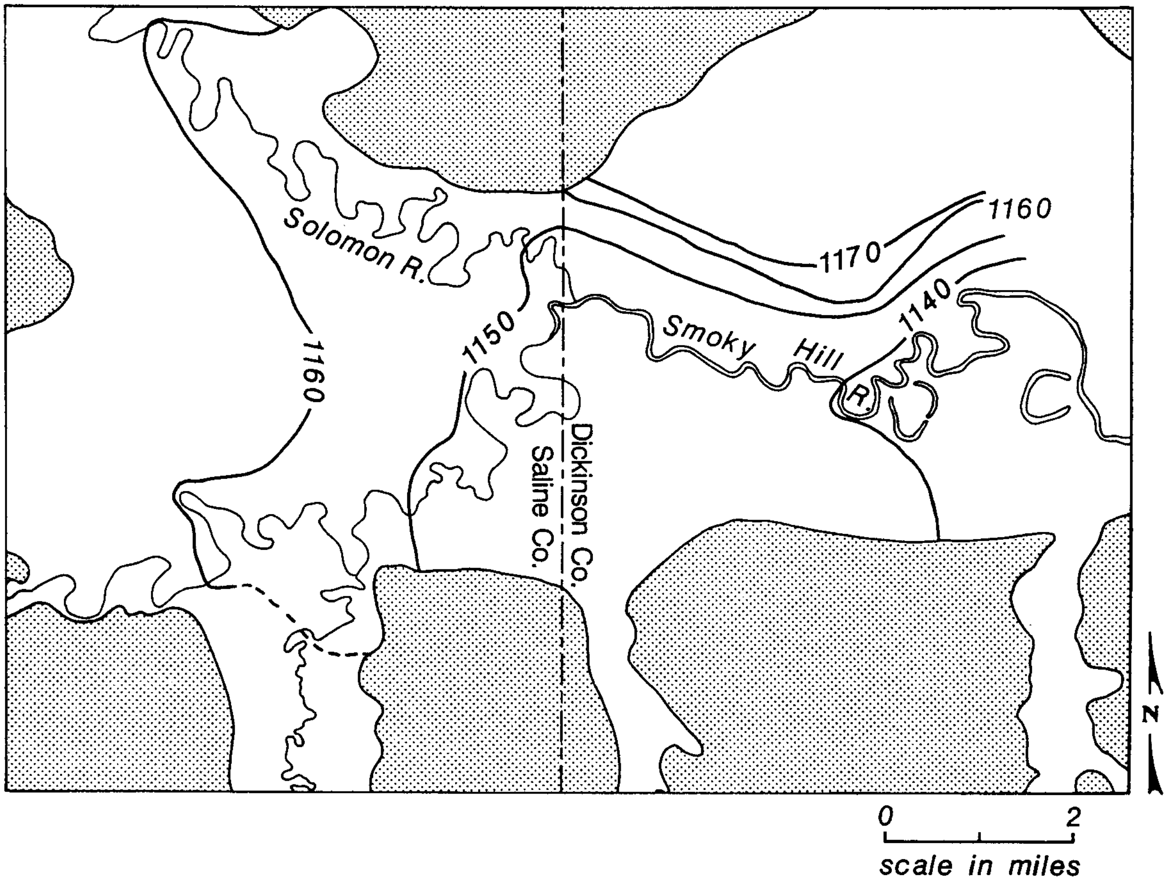

Figure 3.4 Configuration of the water table in alluvial aquifer of the Smoky Hill River Valley in the vicinity of Solomon, Kansas, during May 1984.

solved solids, low in chloride (100-200 mg/L), and low in sulfate (100-200 mg/L). These waters have resulted from the mixing of fresh ground waters from the terrace deposits with more mineralized waters in the alluvial aquifer.

Ground waters in the Smoky Hill River and Solomon River valleys near Solomon are NaCl-type waters. The total dissolved solids of ground waters from this part of the valley are generally above 1000 ppm and contain chloride concentrations that range from 600 to 6800 mg/L, and sulfate concentrations that range from 400 to 6000 mg/L. The more saline waters are generally found near the base of the alluvial aquifer. The area containing these NaCl-type ground waters is located in the vicinity of collapse features that were mapped by Gillespie and Hargadine (1981).

3.4 Analysis of Streamflow Data for the Smoky Hill and Solomon Rivers near the Field Site.

Streamflow records for the Smoky Hill and Solomon rivers were examined to determine streamflow variations and gains or losses in the vicinity of the study area. To accomplish these objectives the monthly and annual records of stream discharge were examined for the New Cambria and Enterprise stream gages on the Smoky Hill River and for the Niles stream gage for the Solomon River (Figure 3.4). The field site is located adjacent to the Smoky Hill River between the New Cambria (13 miles upstream) and Enterprise (24 miles downstream) stream gages. The Solomon River empties into the Smoky Hill River near the town of Solomon.

Figure 3.5 shows the variation in monthly stream discharge for the New Cambria gaging station between the calendar years 1963 and 1983. The monthly streamflow pattern has a pronounced seasonality which is directly related to the precipitation. Figure 3.6 shows the monthly precipitation for the same period from the weather station at Abilene, 10 miles east of the field site.

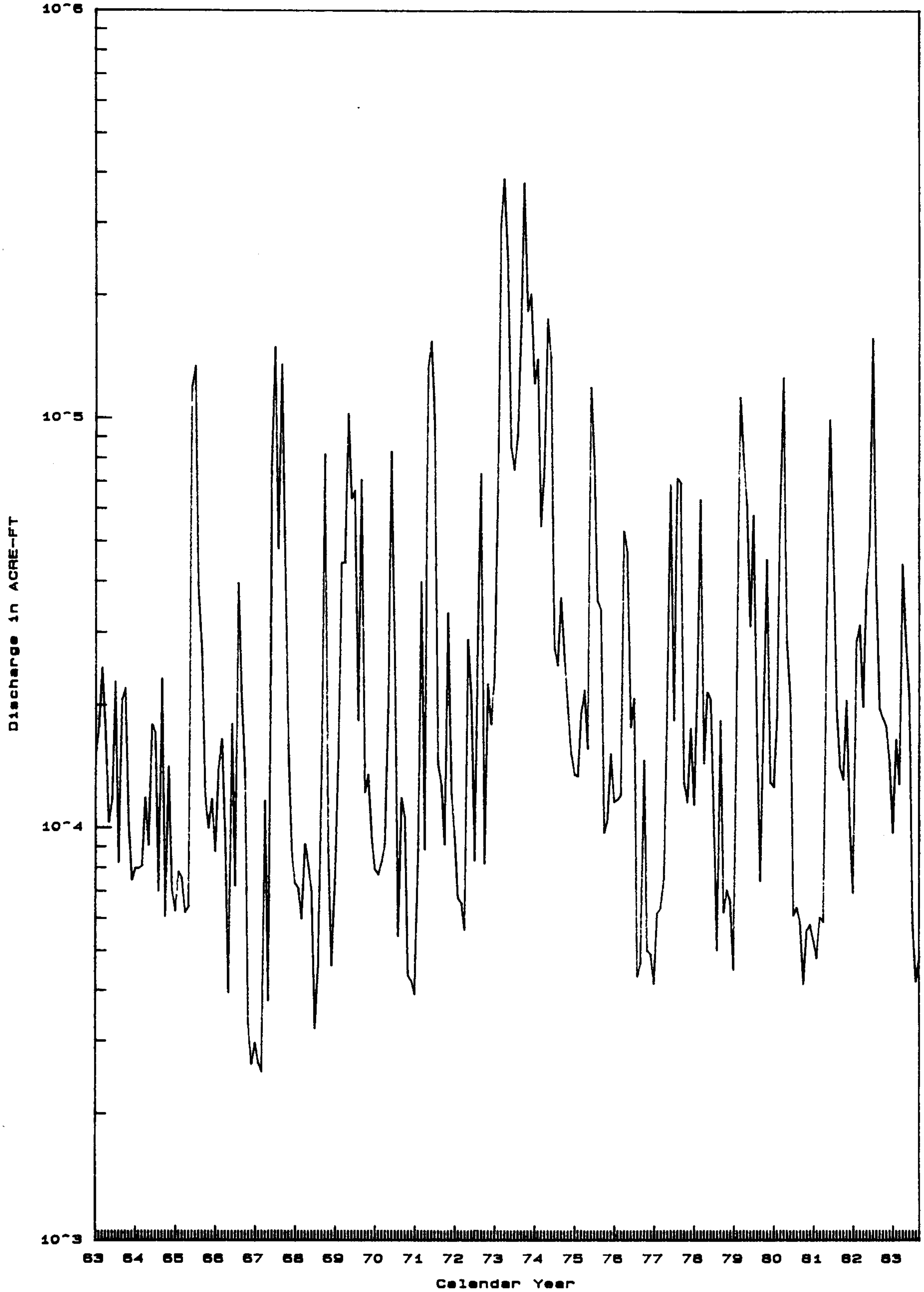

Figure 3.5 Stream discharge at New Cambria gaging station on the Smoky Hill River for the period 1963-1984.

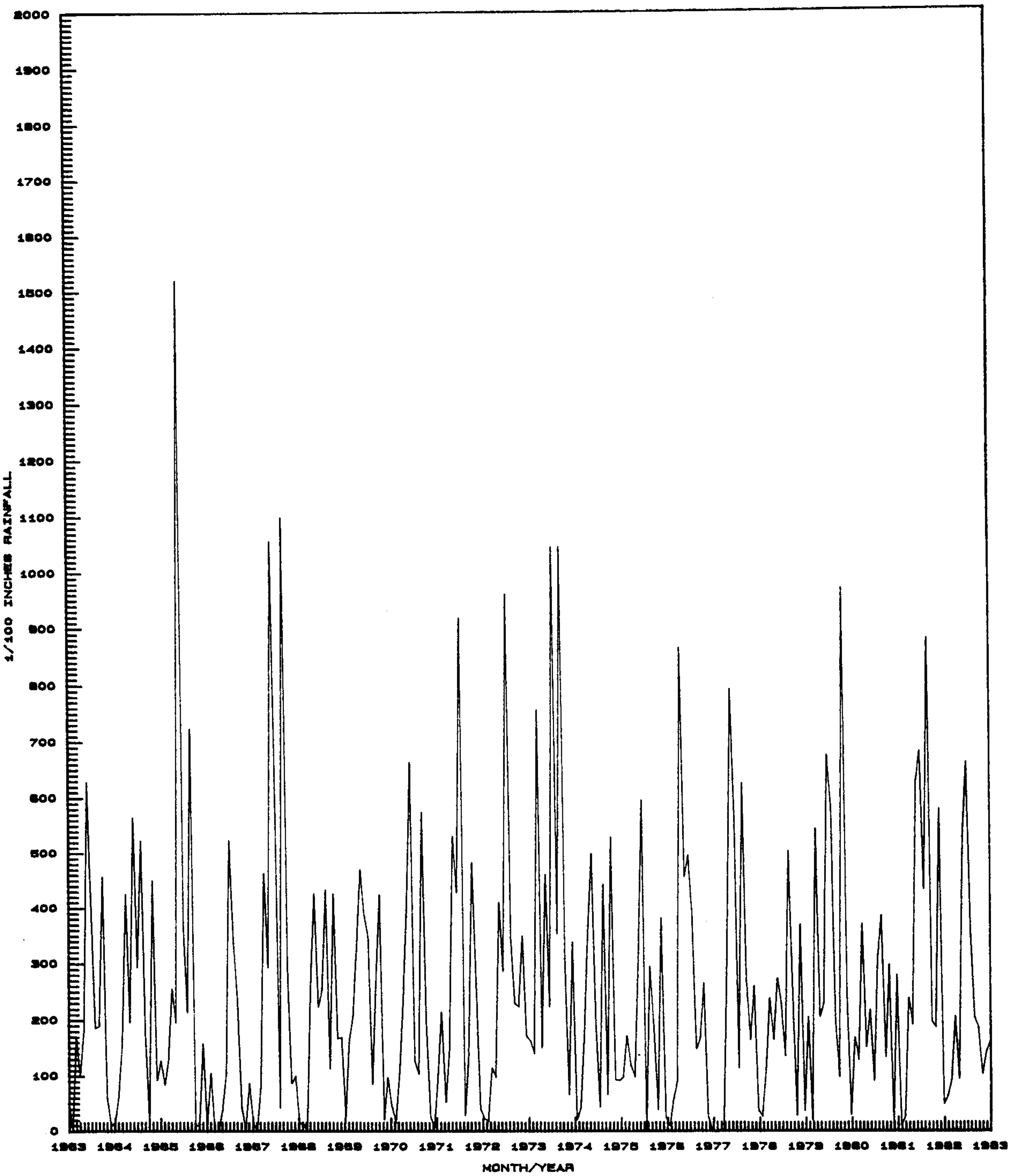

Figure 3.6 Monthly precipitation at Abilene, Kansas, for the period 1963 to 1983.

Stream discharge is generally lower in the late summer, fall and winter, and higher in the spring and early summer. A peak period of discharge occurred in 1973 and 1974 when streamflow and precipitation were considerably higher than normal. A twelve-point moving average of the monthly precipitation at Abilene clearly shows this peak period (Figure 3.7). Gillespie and Hargadine (1981) report that widespread flooding occurred on the Smoky Hill, Saline, and Solomon rivers on April 1, September 29, and October 12, 1973. Similar patterns of stream discharge can be seen in the stream discharge records for Enterprise and Niles (Figures 3.8 and 3.9).

Figure 3.10 shows streamflow gains and losses for the reach of the Smoky Hill River between New Cambria and Enterprise and the Solomon River below the Niles stream gage. This graph was constructed using the monthly streamflow records for the Niles, Enterprise, and New Cambria stream gages. Streamflow gains and losses were calculated by subtracting the total monthly streamflows for the Niles and New Cambria gages from the monthly streamflow at the Enterprise gage. The difference represents an approximate net stream gain or loss for the month depending upon the algebraic sign of the resultant. The average streamflow gain at base flow in these reaches of the Smoky Hill and Solomon rivers is estimated to be 2600 acre-ft or 0.74 cfs/mile of stream channel.

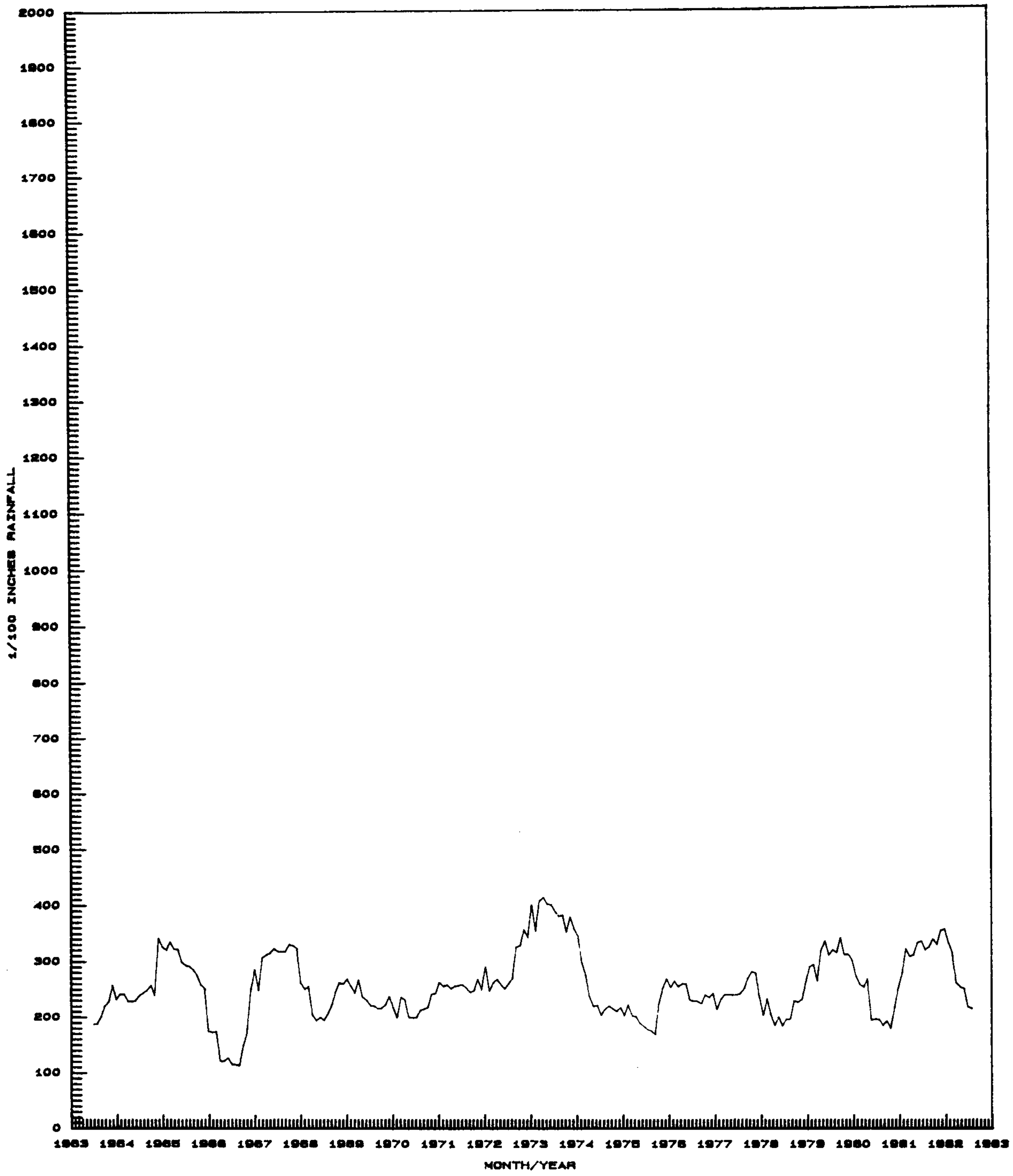

Figure 3.7 Twelve point moving average of monthly precipitation at Abilene, Kansas, from 1963 to 1983.

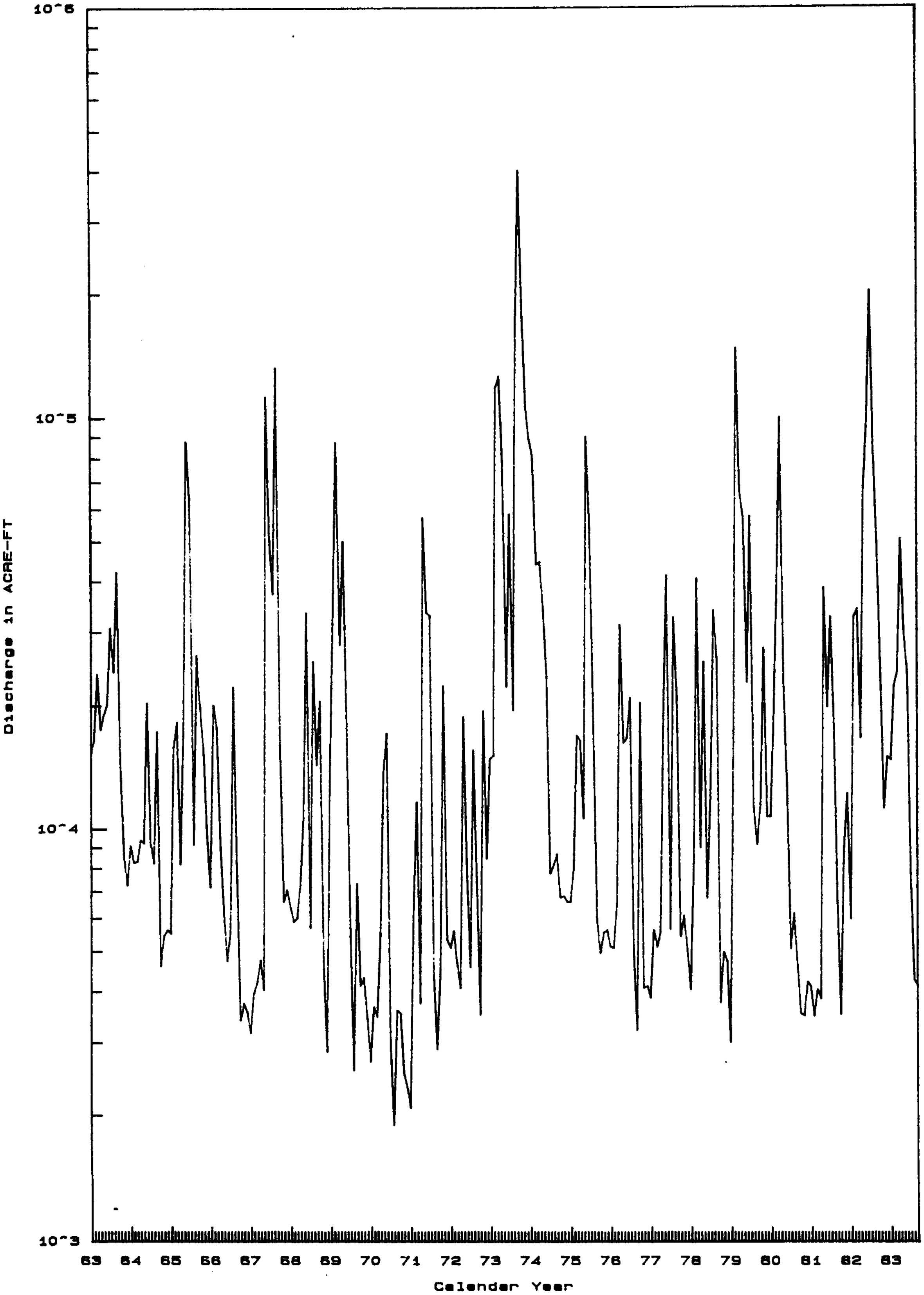

Figure 3.8 Stream discharge at Niles gaging station on the Solomon River for the period 1963 to 1983.

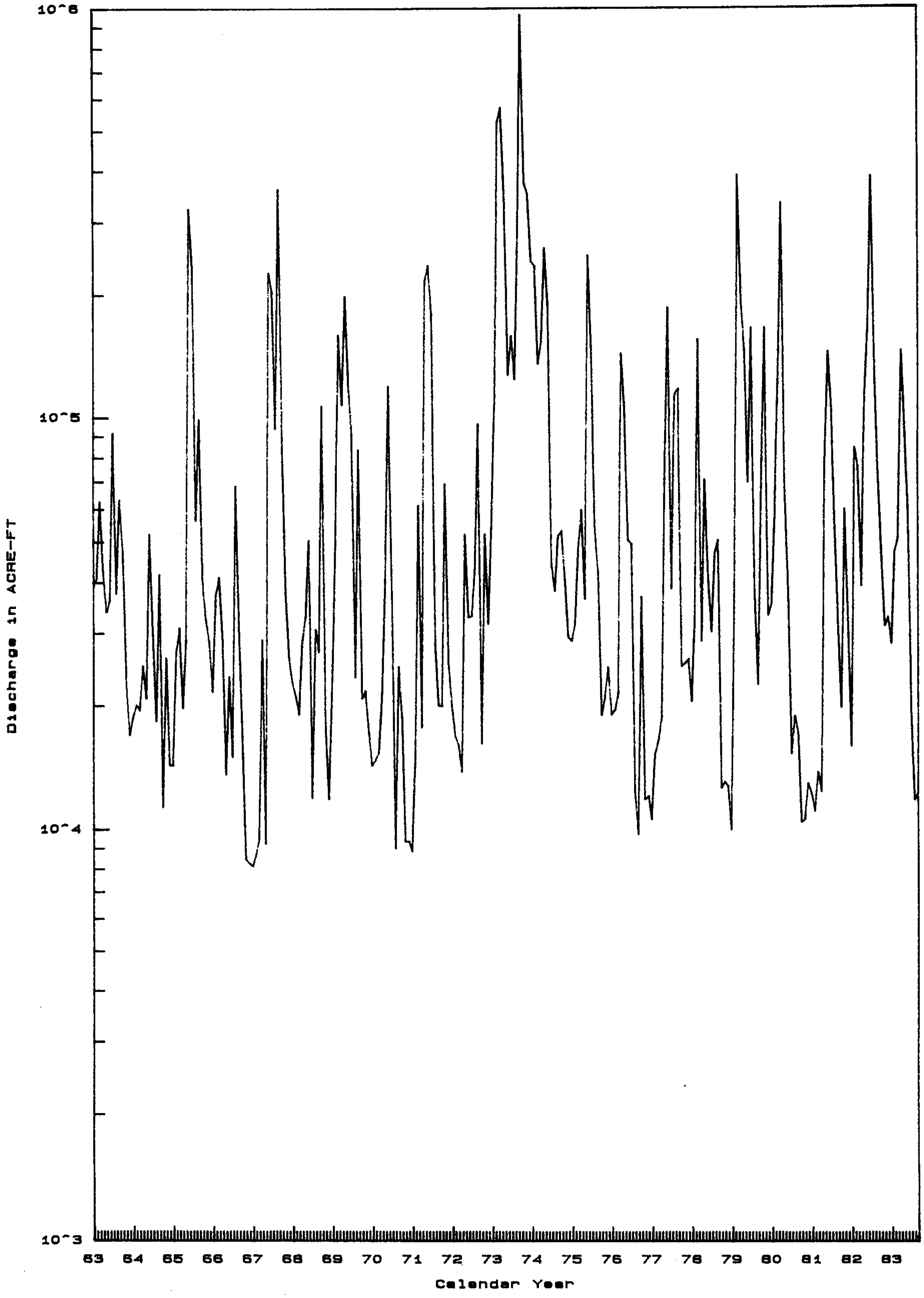

Figure 3.9 Stream discharge for the Enterprise gaging station on the Smoky Hill River for the period 1963 to 1983.

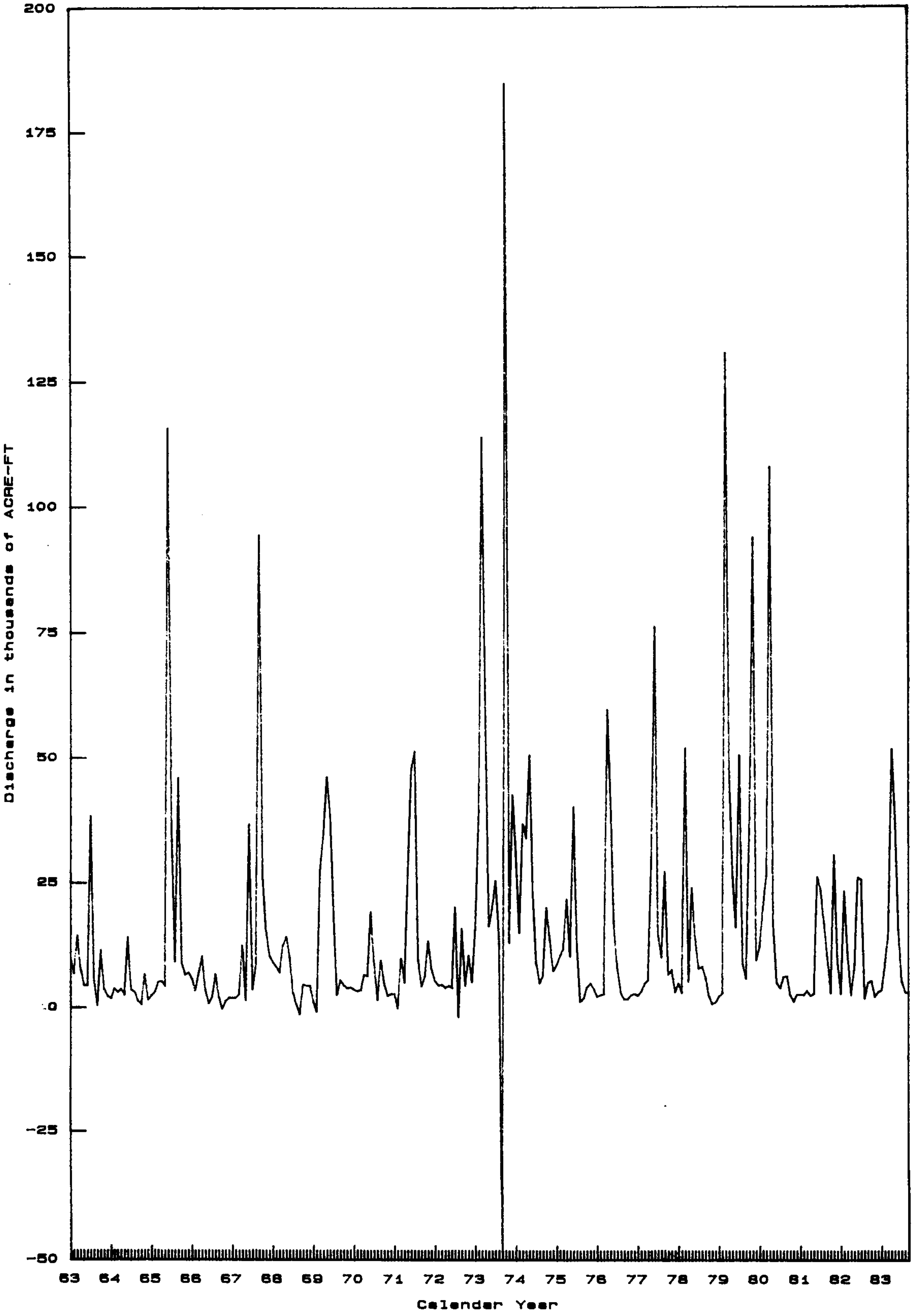

Figure 3.10 Stream gains and losses for the reach of the Smoky Hill River between New Cambria and Enterprise and for the reach of the Solomon River between Niles and the confluence with the Smoky Hill River for the period 1963 to 1983.

4. DESIGN AND INSTALLATION OF THE MONITORING NETWORK

4.1 Observation-well Network

For practical reasons, a particular vertical cross section of the Smoky Hill River valley must be selected for which a detailed description of the saltwater-intrusion zone is to be made. The location of the cross section chosen for our analysis is shown in Figure 4.1. The line of the cross section extends from 3050 feet west of the river to 1550 feet east of the river. This cross section coincides partially with a set of monitoring sites used during the field investigation of Gillespie and Hargadine (1981).

A network of monitoring sites was installed along the line of cross section perpendicular to the Smoky Hill River and at sites remote to the cross section. Figure 4.2 shows a cross sectional view of the monitoring network. A total of 11 monitoring sites comprise the cross sectional network. Table 4.1 gives the position of each monitoring site with respect to the river. As can be seen from Figure 4.2, the density of monitoring sites is highest near the river to observe the saltwater upconing beneath the stream. Temporary monitoring sites were constructed in the stream bottom to conduct seepage experiments during low-flow conditions.

Additional off-line monitoring sites J and L were also constructed to monitor the stream/aquifer system at points upstream of the river. Site J is a new monitoring site located 3300 feet south of monitoring site I and 100 feet west of the river. Site L is located 1400 feet south of site H and 75 feet west of the river and originally contained a deep alluvial piezometer from the field observation network of Gillespie and Hargadine (1981).

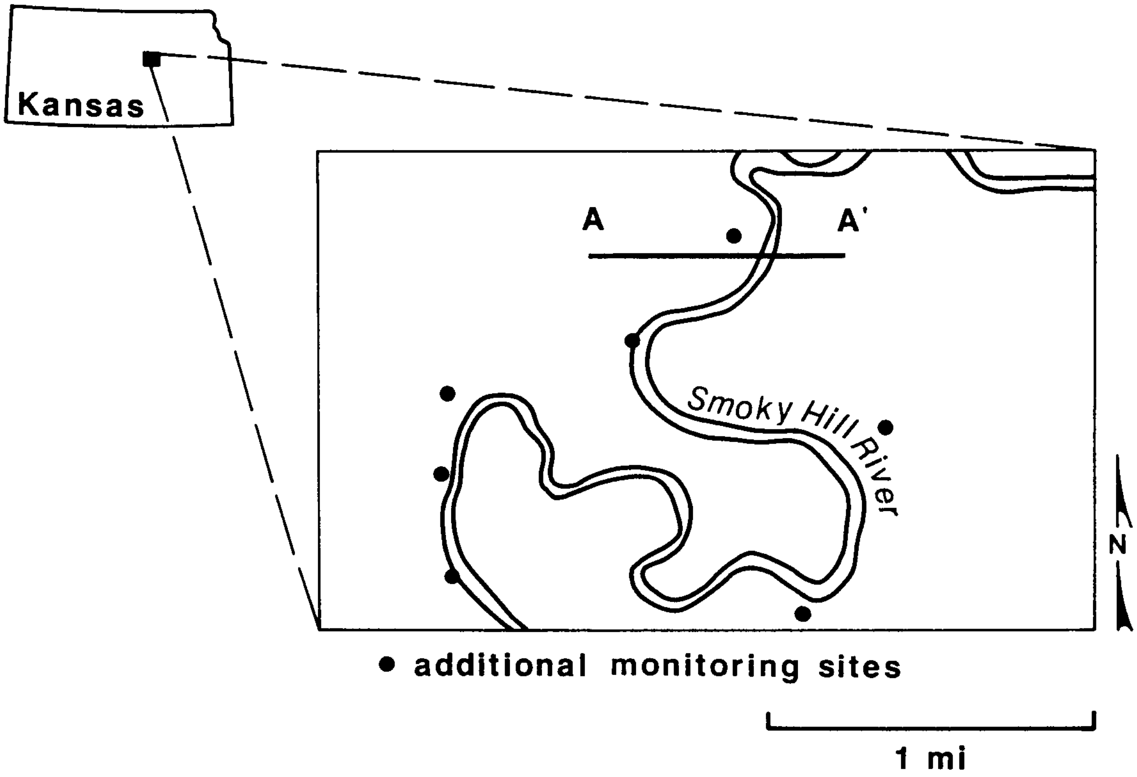

Figure 4.1 Location of the field cross-section.

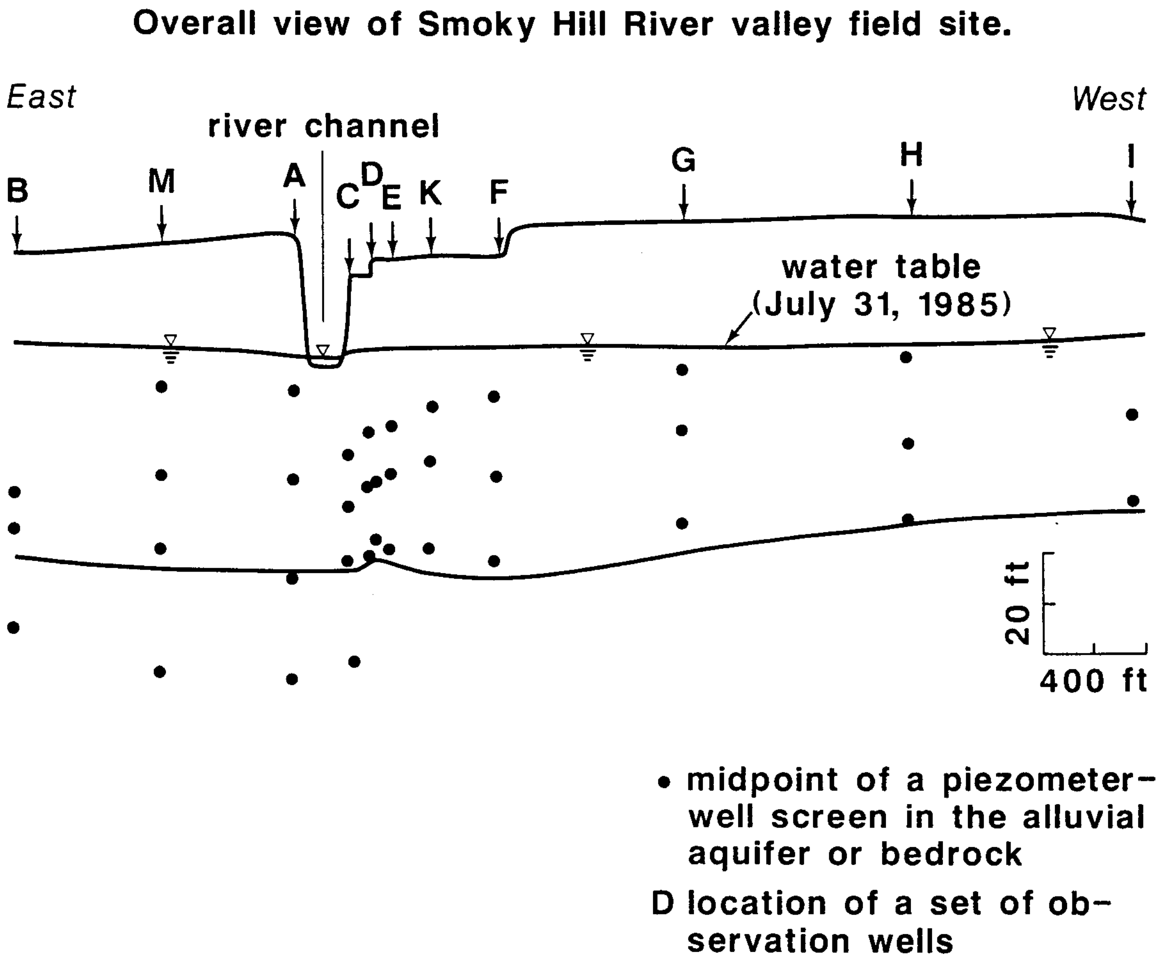

Figure 4.2 Location of the monitoring sites and piezometer well-screen midpoints along the field cross-section in the alluvial and bedrock aquifers.

Monitoring Site	Distance from the river center-line (ft)
East Side	
A	109
M	608
B	1602
West Side	
C	100
D	163*
E	258
K	408
F	652
G	1284
H	2221
I	3104

*Distance is computed from the continuously screened well D-2.

Table 4.1 Location of the monitoring sites along the line of the cross section with respect to the center-line of the Smoky Hill River.

Each monitoring site includes a combination of the following: (1) a well screened continuously through the saturated thickness of the alluvial aquifer; (2) a set of shallow, intermediate and deep piezometers in the alluvial aquifer; and (3) a piezometer screened in the bedrock aquifer beneath the alluvial aquifer. Figure 4.3 is a schematic diagram of a typical monitoring site. Bedrock piezometers were installed near the river and beneath the zone of saltwater upconing. Additional modifications to this basic site design were made as necessary during the field investigation.

4.2 Well Construction and Development

The continuously screened wells were constructed of 2-inch schedule-40 PVC well casing with flush-joint screw fittings in the screened portion of the well. The well screen consisted of machine-slotted pipe sections with five rows of slots of 0.020-inch width arranged along the length of the pipe. Sections of the pipe were assembled and glued at the bottom-end with a 2-inch cap. The annular space around each well was backfilled to within 10 feet of the land surface and cemented from that point to the surface. A cement pad was then placed around the well.

The piezometers were installed in the field using conventional rotary and hollow-stem auger methods. Two-inch schedule-40 PVC pipe was used for the well casing. The well screen consisted of a single 5-foot section of machine-slotted pipe. The slot size used was 0.010 inch in width. The slots were closely spaced and arranged in five rows extending the length of the casing. The well screen and sections of "blank" casing were fitted with 2-inch collars and glued together.

Two different completion techniques were used once the piezometers were installed in the ground. In the case where the piezometers were installed using mud-rotary methods, the well was gravel-packed approximately 2 feet

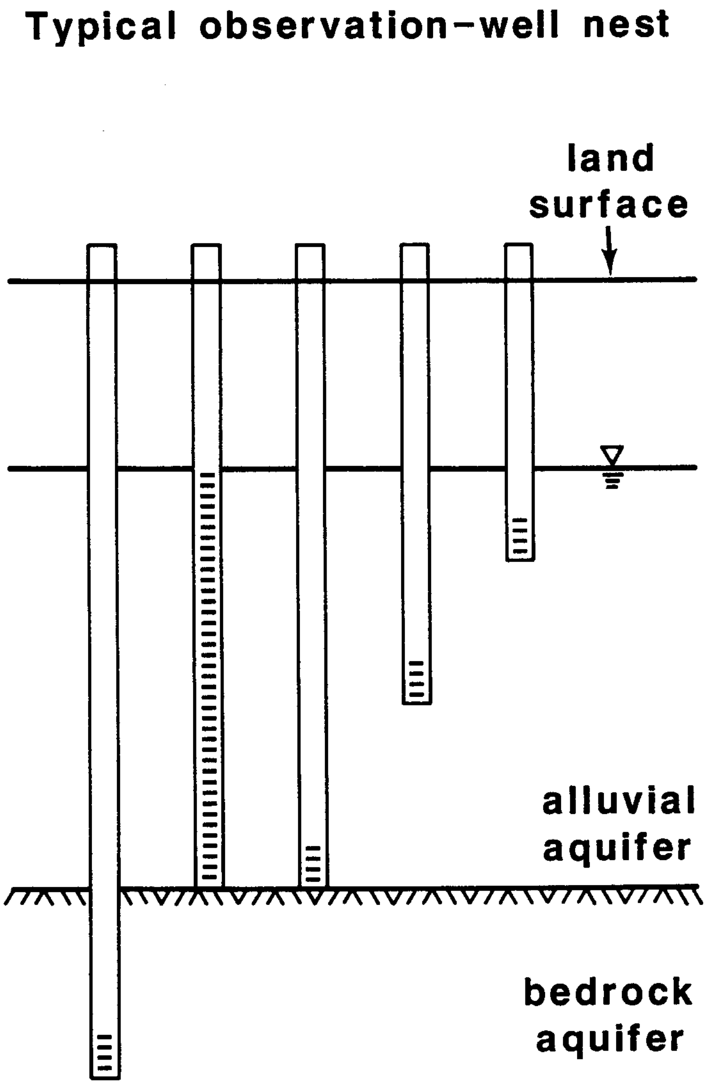

Figure 4.3 Design of a typical monitoring site near the Smoky Hill River.

above the well screen. This was done to help prevent clogging of the well screen with cement. In most cases at least 20 feet of the annular space above the well screen was cemented. The remainder of the annular space was back filled to within 10 feet of the surface. The upper 10 feet of the hole was cemented and a cement pad around the well was constructed. In the case where the hollow-stem auger was used to bore a hole, a natural gravel pack around the well was developed by encouraging sloughing of the borehole wells. The borehole was then back-filled to within 10 feet of the surface and the remainder was cemented. A cement pad was then placed around the piezometer.

The process of development was carried out to remove fines that accumulated in the well casing and gravel pack during the drilling of the borehole. Both bailing and air-pumping methods were used to remove the fines in the piezometers and continuously screened wells. After the initial well development phase, the wells and piezometers were bailed periodically to avoid the accumulation of fine sediments and to ensure collection of representative ground-water samples prior to water-quality sampling.

5. HYDROGEOLOGIC CHARACTERISTICS OF THE FIELD SITE AND THE TECHNIQUES USED FOR THEIR MEASUREMENTS

5.1 Required Field Information

The monitoring network was designed to acquire data on the following: (1) the geologic nature and physical properties of the alluvium and the Permian bedrock; (2) the water-table elevation and fluid-pressure data at various points along the field cross section; (3) the stream stage and seepage rate and chemical quality of water passing through the stream bottom; (4) the nature and extent of the saltwater-intrusion zone and its response to the changes in hydrologic conditions; and (5) the source of the saline ground waters in the aquifer.

Some of the information listed above are measured directly in the field while others are calculated on the basis of observed field data. More than one technique was used for measurement of several properties to compare and evaluate the accuracy of the results. Table 5.1 presents a list of types of measurements and the hydrogeologic or hydrochemical parameters determined from each type of measurement. The measurements have been classified according to their objective use for characterization of the aquifer or monitoring the ground-water conditions. As has been pointed out in Table 5.1, periodic monitoring of the ground-water condition is essential for a concise description of the transient saltwater-upconing condition.

Table 5.2 lists the different types of measurements performed at the monitoring sites according to the type of the well. Measurements taken at piezometers are usually indicators of the local quantities. On the other hand, for continuously screened wells, the measured values are representative

	Periodic Monitoring						Hydrogeologic Framework		
	Ground-water chem. quality	Bottom-hole fluid pressure	Ground-water discharge	Freshwater/ saltwater interface or transition	Stream/aquifer interaction	Specific discharge	Lithology	Hydraulic conductivity	Porosity
Borehole-fluid conductivity	X			X					
Borehole gamma ray							X		X
Pressure transducer		X			X				
Water sampling	X			X					
Seepage measurements			X		X	X			
Fluid-pressure differentials		X		X					
Stream levels					X				
Ground-water levels					X				
Ground-water velocity from thermal pulse						X		X	
Slug tests						X		X	

Table 5.1. Types of field measurements made at the field site and their purposes.

Piezometer	Continuously Screened Well
Bottom-hole fluid pressures	Ground-water levels
Water quality	Velocity measurements using the heat-pulse method
Slug tests	Fluid-pressure differentials
Borehole gamma ray	fluid conductivity
	water quality

Table 5.2. Types of measurements made in the piezometers and continuously screened wells at the field site.

of average quantities over some length of the well or they may represent changes of a physical property such as pressure in the vertical direction.

The subsequent sections include detailed discussions of the techniques used for measurement of various hydrogeologic characteristics of the field cross section and the interpretation of the results. Some of the field investigation results are presented here because of appropriateness but a more complete description of the saltwater-upconing conditon at the field site will be given later.

5.2 Monitoring Ground-water Flow Conditions

Fluid pressures, stream levels and static ground-water levels were measured at the monitoring sites to determine ground-water flow conditions in the alluvial and bedrock aquifers. These measurements were used to calculate the hydraulic-head distribution in the field cross section. Fluid pressures were measured in the piezometers using an SE-1000A Hydrologic Monitor manufactured by In Situ Inc. Pressures are read from the device in feet of freshwater to the nearest 0.01 foot. The accuracy and repeatability of the instrument are within ± 0.2%, of the full range at constant temperature (100 psi). Static ground-water levels were measured in the continuously screened wells using either a steel or electric tape. Stream levels were measured by taking levels. All elevations were referenced to a datum at piezometer F-1 (elevation = 0.00). Ground-water specific-weight profiles were prepared from differential-pressure measurements in the continuously screened wells. Description of the method of differential pressures is given in Section 5.3.2.

The fluid pressures and elevations at the measurement points of a particular site and the vertical variation of fluid density were used to compute the hydraulic head defined by the equation,

$$h_i = z_i + \sum_{i=1}^{n} \frac{p_i - p_{i-1}}{(\gamma_i + \gamma_{i-1})/2} \qquad (5.1)$$

where z_i is the elevation, p_i is the fluid pressure, γ_i is the specific weight of the fluid, h_i is the hydraulic head and i is an index for the measurement points arranged from higher to lower elevation in the aquifer. We should point out that hydraulic head (or fluid potential) of an inhomogeneous fluid as defined by Hubbert (1940, p. 802) has a definite meaning only when the fluid density is a function of pressure. However, ground waters contained in an unconfined aquifer are considered to be incompressible at ordinary pressures. The variations of density recorded in equation (5.1) are due to the changes in salt concentration and are not related to the fluid compressibility. The approximation of hydraulic head from equation (5.1) is derived by adding up the elevation head of a measurement point to the sum of the pressure-head increments of the overlying vertical fluid column.

The hydraulic heads computed from equation (5.1) were plotted on a cross sectional view of the alluvial and bedrock aquifers along the line of monitoring sites and contoured to show the approximate ground-water flow conditions during the time that the measurements were taken. This process assumes that fluid specific-weight variations in the alluvial and bedrock aquifers are insignificant laterally and that the hydraulic heads calculated from one set of measurement points at a monitoring site can be compared to heads at other monitoring sites. This assumption is only partly true because significant lateral changes in fluid specific weight are present beneath the west bank of the Smoky Hill River. However, this deviation from the assumptions is not considered severe and the contoured distribution of head is consistent with the configuration of the water table.

5.3 Monitoring the Saltwater Upconing

Saltwater upconing in the vicinity of the river was monitored using two methods: a borehole geophysical logging technique to measure the fluid resistivity and a differential-pressure method to compute the fluid specific weight. Note that the fluid resistivity is inversely related to TDS (total dissolved solids) whereas the specific weight has a direct relationship with TDS. The existing relationships between fluid resistivity and specific weight, and TDS are the basic concepts used for detection of the saltwater intrusion zone.

To obtain the relationships described above, borehole geophysical logging and pressure measurements were performed in the continuously screened wells at each of the monitoring sites. It is assumed in both methods that conditions in the continuously screened wells accurately reflect conditions in the surrounding aquifer, i.e. the vertical hydraulic gradient is not significant in the well. The results of each method were compared to the chemical analyses of water samples from the piezometers at the field site to check the results of each method.

5.3.1 Borehole Geophysical Logging

A borehole fluid-resistivity logger manufactured by the EG & G Mount Sopries Instrument Company was used to measure borehole fluid resistivity. Figure 5.1 shows four fluid-resistivity logs taken in July 1985 from sites M, A, C, and D near the river. Also shown is the trace of the top of the freshwater/saltwater transition zone interpreted from the chemical analyses of water samples collected at that time and the fluid-resistivity logs. High fluid resistivities are shown above the top of the transition zone. However, there is considerable fluctuation in the trace of the fluid-resistivity

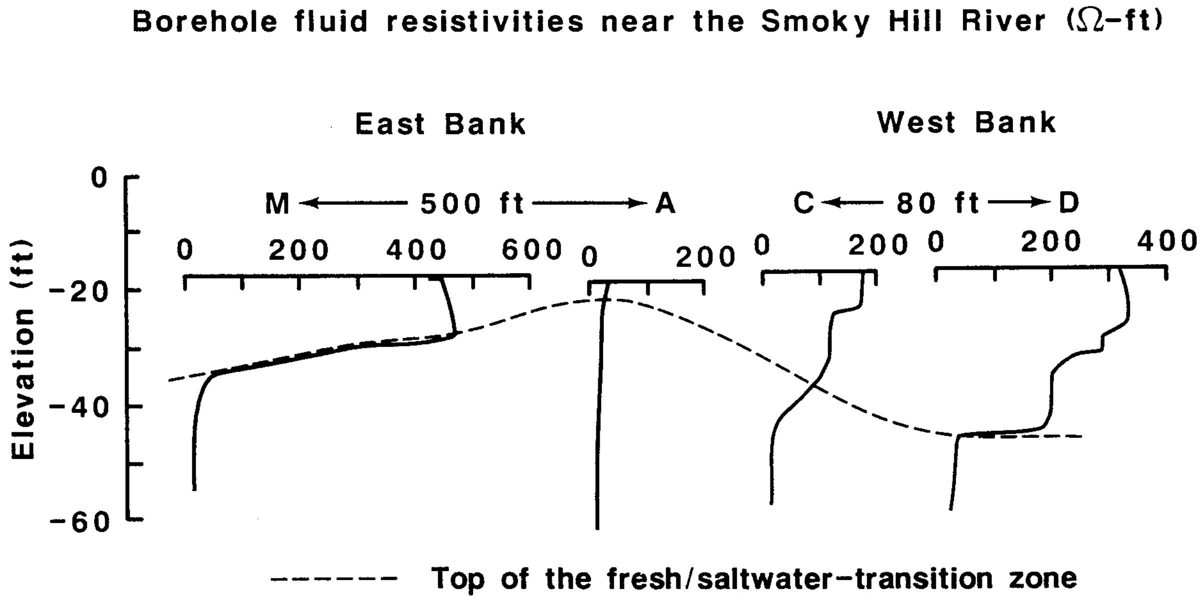

Figure 5.1 Top of the freshwater/saltwater transition zone interpreted from the ground-water chemical quality data and the borehole fluid resistivity profiles.

logs. These fluctuations make it difficult to locate the top of the transition zone.

Figure 5.2 is a plot of specific conductance of water samples vs. borehole fluid resistivities that were picked off the logs at the same elevation in the subsurface as the midpoint of the appropriate interval sampled by each of the piezometers. Ideally the plotted points in Figure 5.2 should fall along a straight line showing an inverse relationship between fluid resistivity and specific conductance. An inverse relationship is indicated by the plotted points. However, there is considerable scatter in the data in the lower range of specific conductance. The high degree of scatter in the lower range shows that the logging tool may not be sensitive enough to detect small changes in fluid resistivity associated with changes of TDS in the borehole of the continuously screened wells. Specific conductance of the water is directly related to TDS. The relationship between TDS and specific conductance at the field site is shown in Figure 5.3 using the data from July 1985, and November 1985.

5.3.2 Differential-pressure Method

Another method that was used to monitor saltwater upconing at the field site is the differential-pressure method (Macfarlane et al., 1986). Figure 5.4 shows a continuously screened well penetrating the entire saturated thickness of an unconfined aquifer. Ground-water density is assumed to be a function of depth, H-z, in the aquifer (Figure 5.5). Two pressure measurements are made below the water level in the continuously screened well separated by depth interval $(z_1 - z_2)$, such that the change in density with depth can be approximated by:

$$\frac{d\gamma}{dz} (z_1 - z_2) = \text{constant} \qquad (5.2)$$

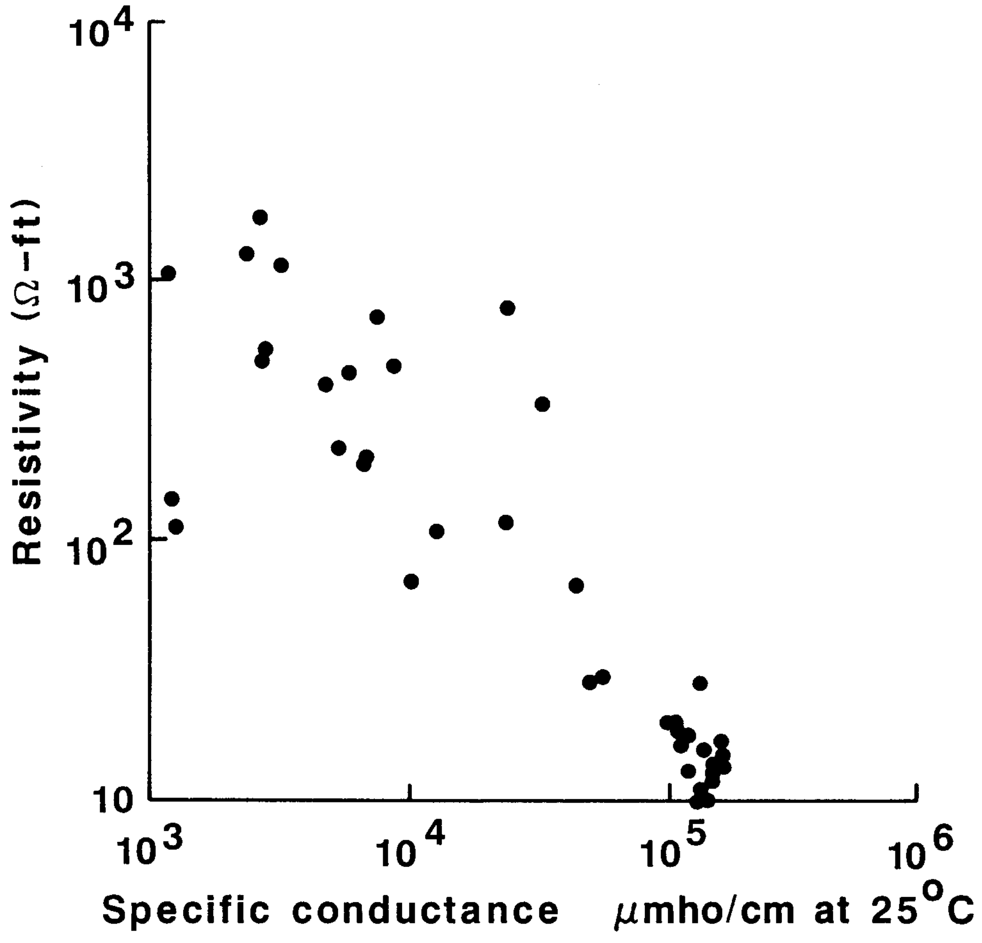

Figure 5.2 Scatter diagram of borehole fluid resistivities vs. specific conductance of the water samples.

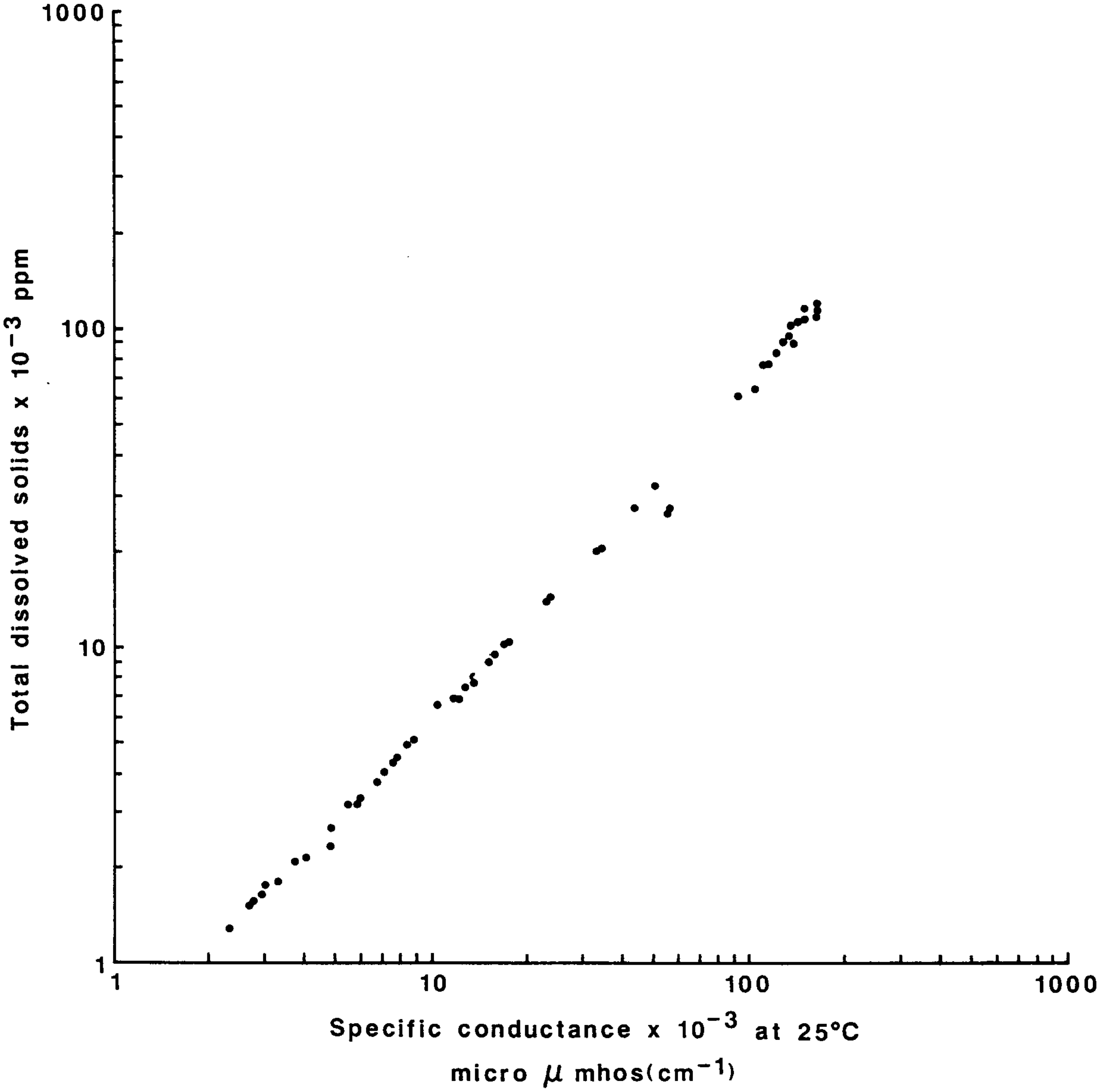

Figure 5.3 Total dissolved solids vs. specific conductance for water samples collected during the field investigation.

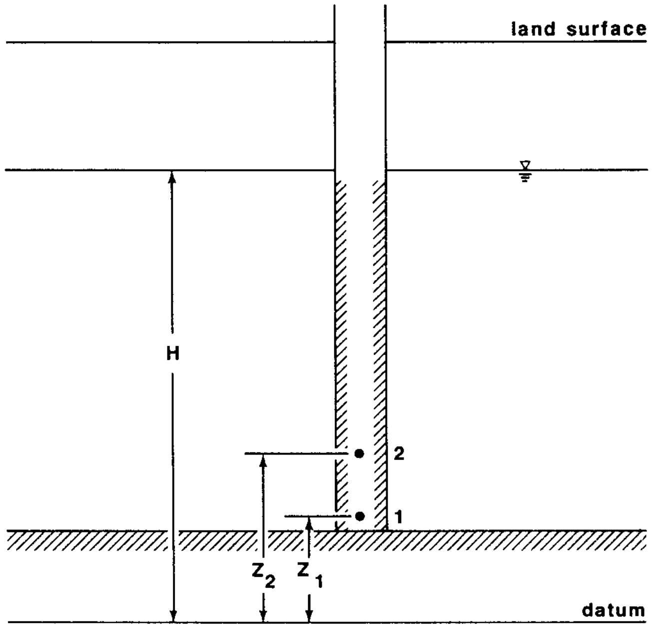

Figure 5.4 Cross-sectional view of a continuously-screened well with the location of sampling points for pressure differential measurements.

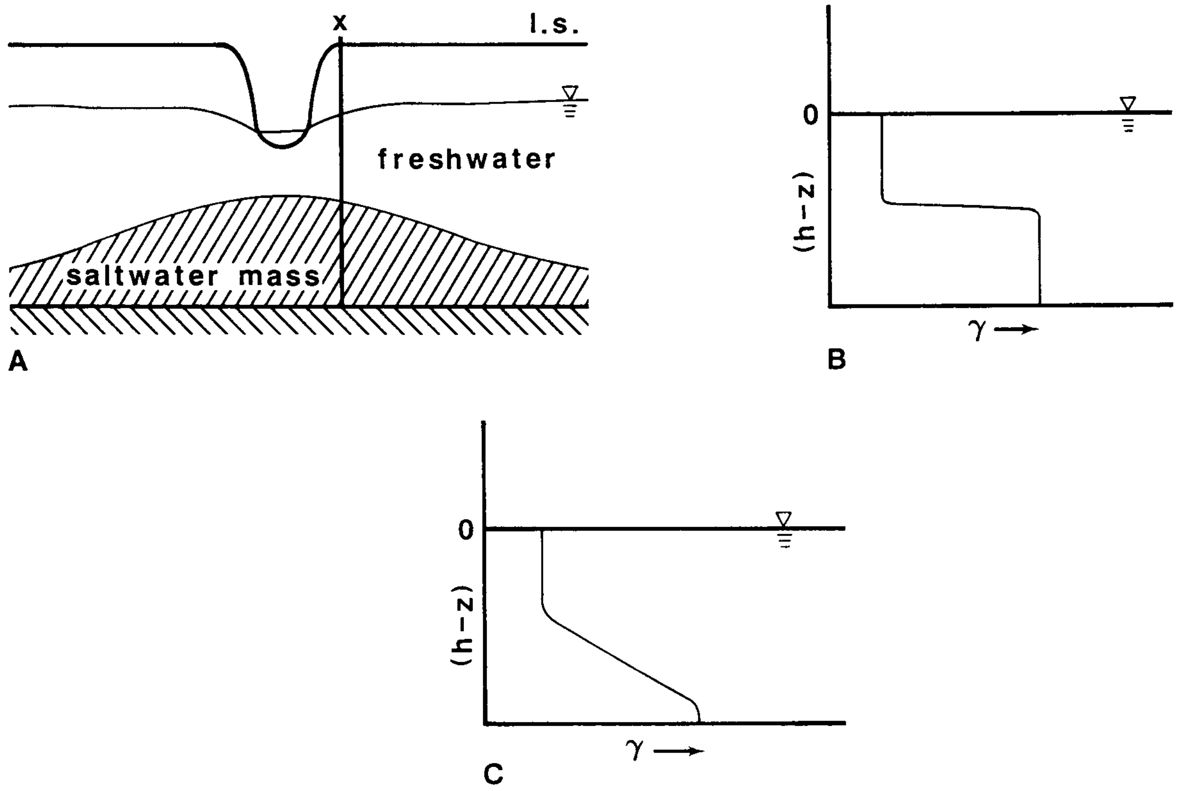

Figure 5.5 Hypothetical relationship between the saltwater body and the stream (A); the variation of ground-water specific weight with depth below the water table where a thin transition (B) or a thick transition (C) separates the freshwater and saltwater in the alluvial aquifer.

Then the ground-water density at the midpoint of the interval is the average density.

$$\gamma_m = \frac{\gamma_1 + \gamma_2}{2} \qquad (5.3)$$

The differential pressure, Δp , measured over the depth interval is related to the average ground-water density by:

$$\Delta p = p_2 - p_1 = \gamma_m(z_1 - z_2) \qquad (5.4)$$

Thus, ground-water density at the midpoint of the interval, z_m, can be calculated from measurements of differential pressure using the relationship:

$$\gamma_m = \frac{\Delta p}{(z_1 - z_2)} \qquad (5.5)$$

A smooth curve can be drawn through a plot of γ_m vs. z_m to show the variation of water density with depth in the continuously screened well.

Differential-pressure measurements were taken at locations three feet apart from the bottom of each continuously screened well to the top of the screened portion using the Hydrologic Monitor. Some experimentation was done to determine the proper depth spacing between differential-pressure measurements. For any particular situation the length of the interval must be sufficiently large to minimize the effect of instrumentation errors yet small enough to measure changes in fluid density. Figure 5.5 shows two typical types of fluid-density profiles: one for a thin freshwater/saltwater transition (or sharp interface) and another for a thick transition zone.

As mentioned before, this method assumes that conditions in the continuously screened well reasonably approximate conditions in the aquifer along the entire length of the screened portion. This assumption was checked by (1) comparing the computed ground-water specific weights to measured water sample specific weights and (2) comparing the pressure distribution below the water level in the continuously screened wells with the distribution of bottom-hole pressures measured in the piezometers at each monitoring site.

Figure 5.6 compares the fluid specific weights calculated from the differential-pressure method with the specific weights of water samples collected from the piezometers. A regression analysis shows that the measured and calculated densities are not significantly different from each other.

The fluid-pressure distributions determined from the continuously screened wells and piezometers were plotted vs. depth in the alluvial aquifer beneath monitoring sites, A, C, D, and K for November 27, 1985 (see Figure 5.7). Fluid pressures in the deepest parts of the alluvial aquifer as they are measured in the piezometers cannot be compared to the pressures in the continuously screened wells because these wells do not extend to measurement depths at sites A, C, and K. However, estimates of fluid pressure at the appropriate depth can be extrapolated from the curve. At each of the sites A, C, and K, the fluid pressure-depth relationships derived from measurements taken in the continuously screened wells are identical or are within the range of instrument error (± 0.1% of range or to within .23 foot of fresh water) in comparison to the piezometers. At site D the bottom-hole pressure in D-5 is 0.72 foot of freshwater higher than the fluid pressure measured at the same level in the continuously screened well, D-2. This fluid-pressure difference (range: 0.07 to 0.72 foot of freshwater, mean = 0.50 foot) has been relatively constant for almost all of the sets of measurements taken during the course of

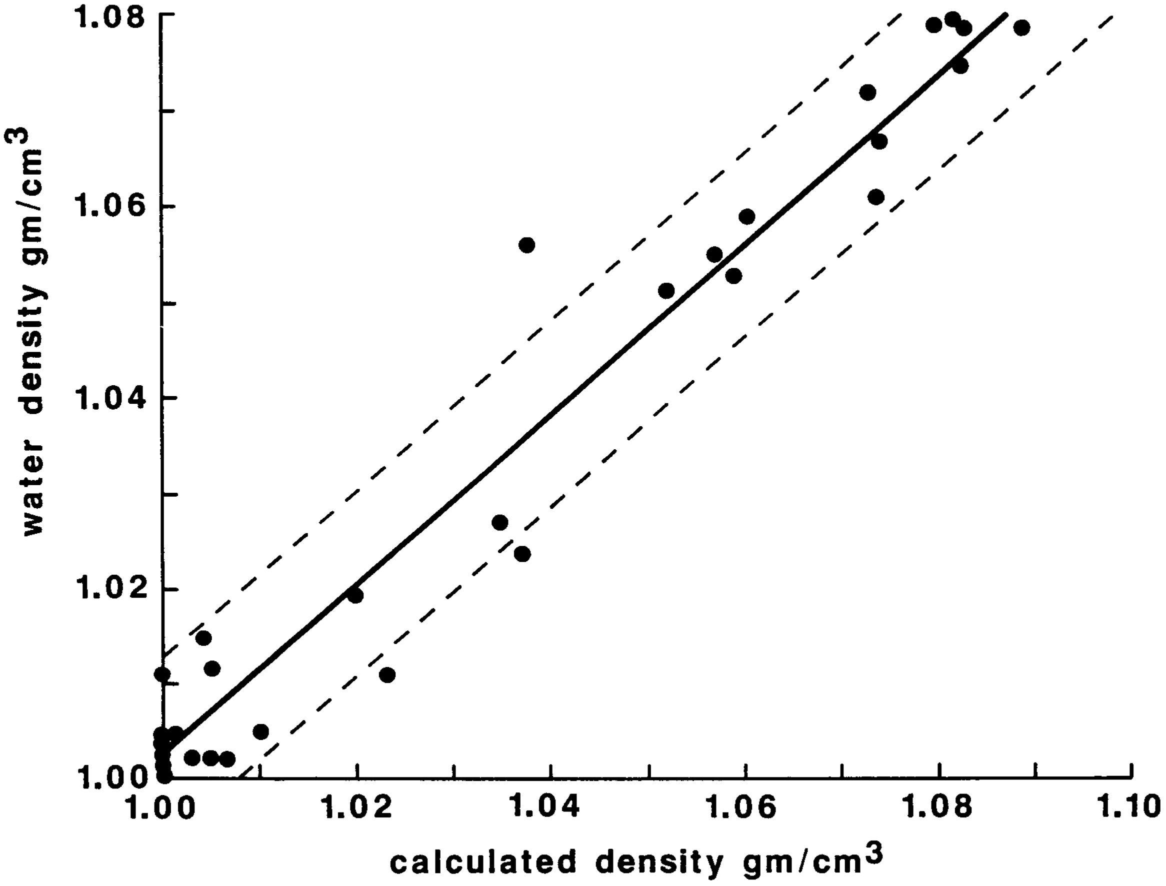

Figure 5.6 Linear regression of groundwater sample densities and ground-water densities calculated from the differential pressure method, showing also the 95% prediction limits.

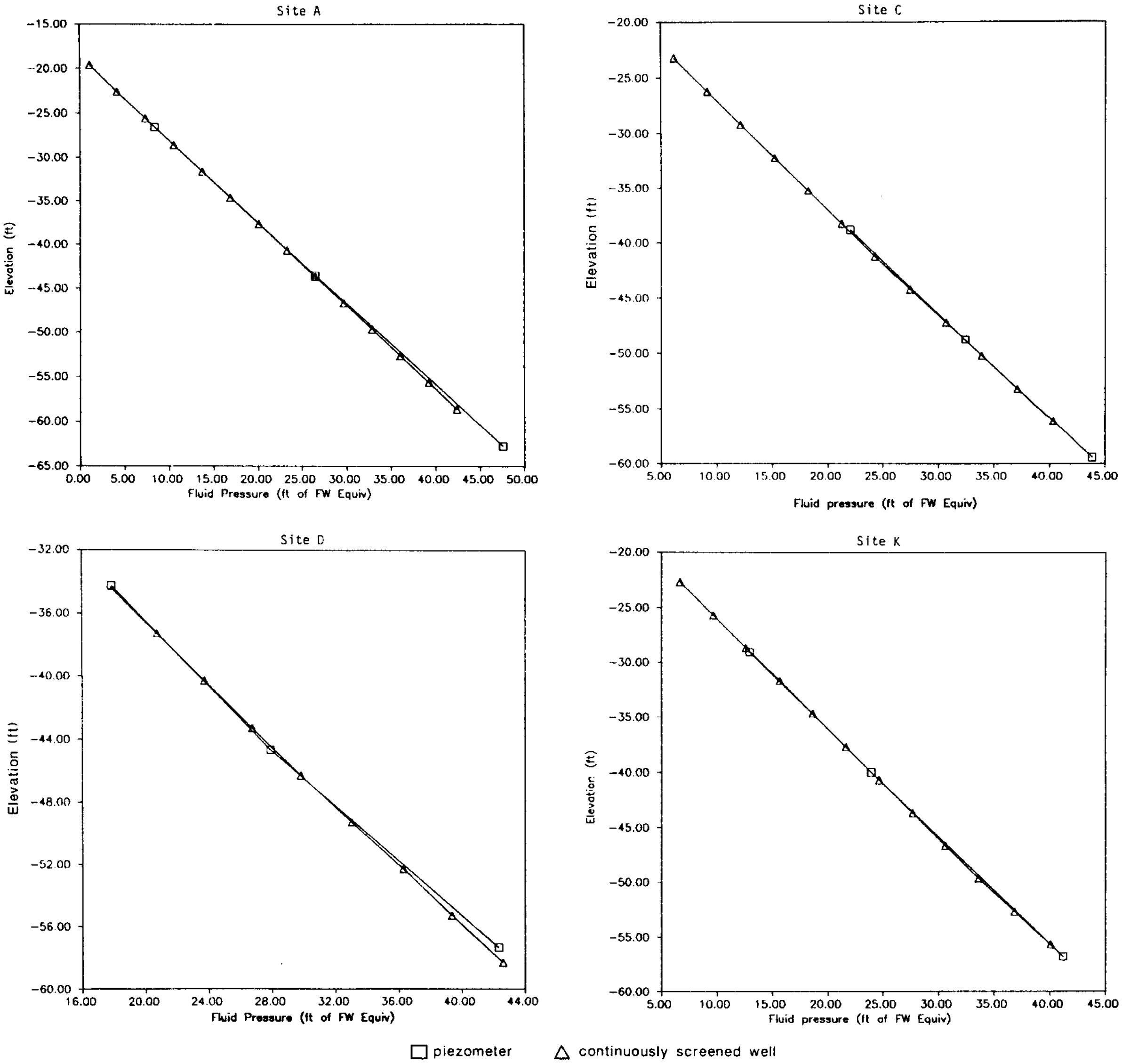

Figure 5.7 Fluid pressure-depth profiles of the piezometers and continuously-screened wells at monitoring sites A, C, D and K from measurements taken on November 27, 1985.

the study and seems to be slightly affected by ground-water flow conditions. These fluid-pressure differences have also been found in the data from some of the other monitoring sites. Although some pressure differences exist between the continuously screened wells and the piezometers, they are not considered to significantly affect the results of the differential-pressure method in these wells.

5.4 Surface Geoelectric Surveys

Several geoelectric surveys were conducted adjacent to the line of monitoring sites to determine the lateral extent of saltwater upconing in the alluvial aquifer. Surface geoelectric techniques are well suited for defining areas of saltwater upconing because the spatial variation of bulk resistivity is directly related to the presence or absence of brines in the alluvial aquifer. Low-resistivity brine-saturated sandy sediments can be easily distinguished from high-resistivity low-TDS water-saturated sandy sediments in the shallow subsurface using the surface-resistivity technique. However, if the sediments beneath the sounding site contain appreciable silt and clay, low resistivities will also be measured at the surface. As a result, to distinguish between the two interpretations the distribution and nature of the lithologies must be known.

Vertical electrical soundings were conducted on the east side of the Smoky Hill River to determine the geoelectric section in the area surveyed and the appropriate electrode spacing for areal surveys using horizontal profiling techniques. Four vertical electrical soundings and 44 apparent-resistivity measurements were taken during the course of the field investigation. All surveys were conducted when the stream was under low-flow conditions. The vertical electrical soundings were taken during the latter part of July 1985, and two horizontal profiling surveys were conducted on the east and west sides of the river during the latter part of March 1986.

The vertical electrical soundings were taken using a Schlumberger electrode array (Figure 5.8). Measurements of apparent resistivity were made with a Model 2390 signal-enhanced Bison surface-resistivity meter and were used to plot the vertical electrical sounding curve. Four soundings were taken along a line beginning at a point 115 ft, N30E of site A (S-1) and extending eastward to a point located 205 ft, N75E of site M (S-4). Each sounding was begun at an AB/2 spacing of five feet and the measurements were terminated when sufficient data points were collected to define the terminal branch of the sounding curve rising at a 45 degree angle. In all cases the maximum AB/2 spacing was less than 1000 feet. Each vertical electrical sounding was interpreted using an automatic iterative interpretation technique (Zohdy, 1973). Figure 5.9 shows a typical vertical electrical sounding curve and the interpreted geoelectric section of the sounding site. The interpreted geoelectric section was then modified based on the known hydrogeology of the site by changing the interpreted layer thicknesses and resistivities of the section. The modifications were considered completed when an earth model geolectrically equivalent to the original interpretation of the sounding site was produced.

The apparent resistivities calculated at each spacing of the electrode array were plotted for each of the sounding sites and contoured to show the variation of apparent resistivity between sites (a cross section of apparent resistivity). Apparent resistivity is an aggregate property of part of the geoelectric section penetrated by an applied electric current and should not be confused with the resistivity of individual layers in the geoelectric section. Figure 5.10 shows the variation of apparent resistivity in the cross section between sounding sites S-1 and S-4. The cross sections show that

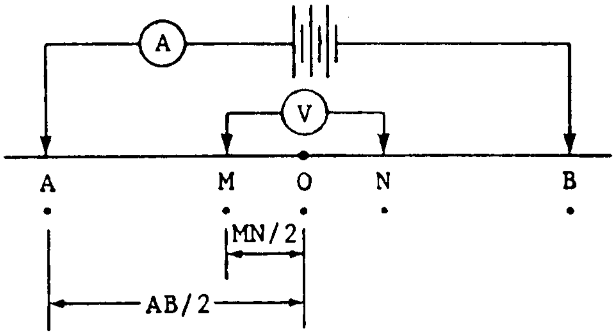

Figure 5.8 Schematic representation of the Schlumberger electrode array for surface resistivity measurements.

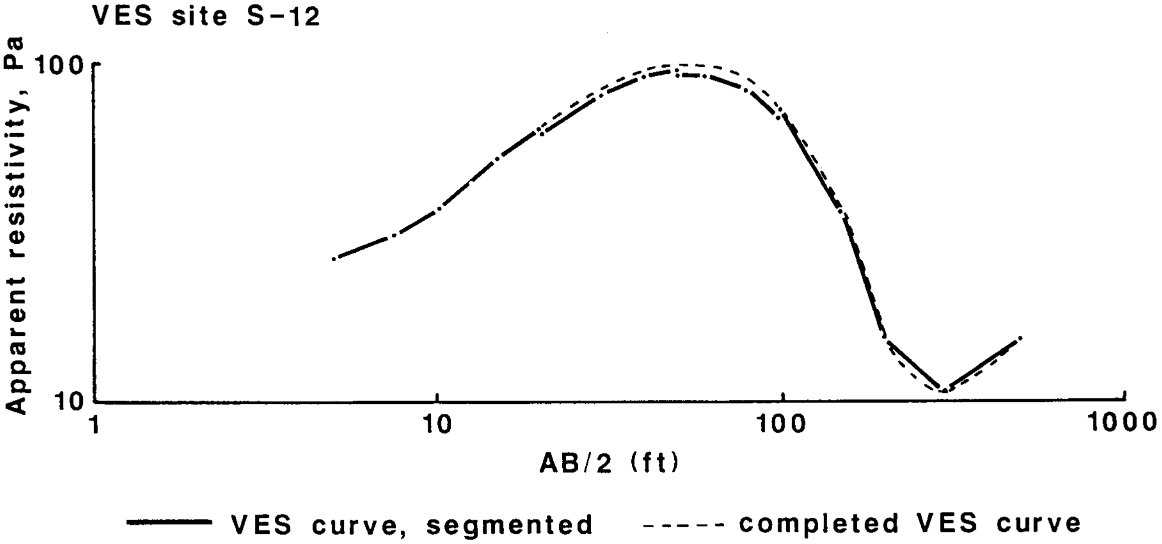

Figure 5.9 Vertical electrical sounding (VES) curve for surface resistivity sounding at Site S-12.

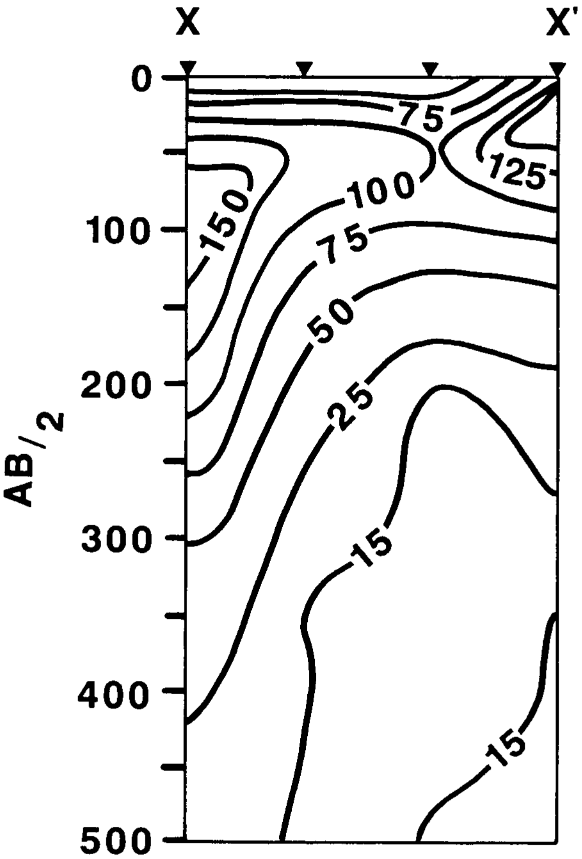

Figure 5.10 An apparent resistivity cross-section between VES sites S-1 and S-4 on the east bank of the Smoky Hill River.

relatively low apparent resistivities were found at shorter electrode spacings at site S-2, 3 and 4. This suggests shallow brines are present beneath these sites at shallow depths and at greater depths beneath sounding site S-1. These results have been verified with the interpreted geoelectric sections for the four sounding sites.

The horizontal profiling surveys of the area on both sides of the river were run using a Schlumberger array with a spacing of 150 ft. The spacing size was determined from the cross section of apparent resistivity between soundings S-1 and S-4 (Figure 5.10). This spacing was chosen to outline areas of high and low apparent resistivity in the areas surveyed.

Figure 5.11 shows the lateral variation of apparent resistivity in the vicinity of the monitoring sites on the east and west sides of the Smoky Hill River. A large north-south-trending area of low apparent resistivity (less than 50 ohm-feet) at the 150-feet spacing occurs east of the river. Another very elongate low resistivity was found south of the line of monitoring sites and north of the river. The low-resistivity area is oriented in an east-west direction and generally follows the course of the river channel. Apparent resistivities are above 100 ohm-feet near the river to the north and south of monitoring sites A, K, and M, and to the south of G, next to the river. To the east of this low-resistivity area, apparent resistivities increase to approximately 100 ohm-feet. The apparent resistivities are generally lower on the west side than on the east side because the alluvial sediments are more fine grained. Additionally, low apparent resistivities (less than 25 ohm-feet) are found near the river and generally increase away from the river toward the line of monitoring sites.

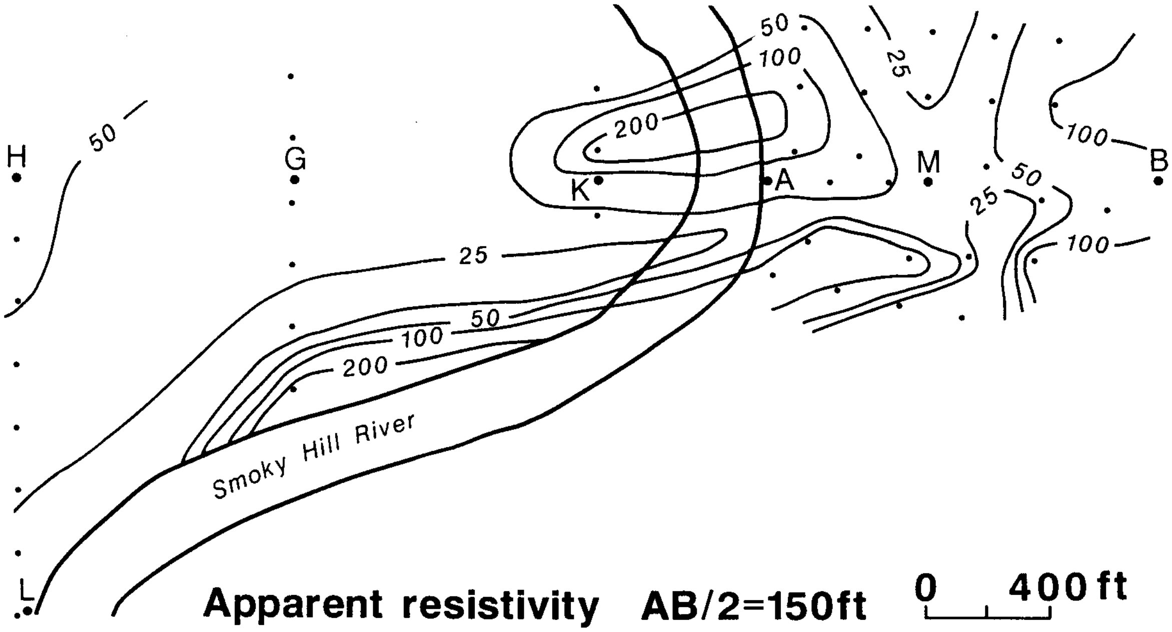

Figure 5.11 Distributions of apparent resistivity from surface resistivity measurements at the field site; a current electrode spacing (AB/2) of 150 ft was used to make the measurements.

5.5 Field Measurements in the Active Stream channel Bottom

A series of measurements of ground-water seepage and hydraulic head were taken in the active channel of the Smoky Hill River stream bottom between monitoring sites A and C. Seepage meter and miniature piezometers (minipiezometers) were used to make these measurements. Figure 5.12 shows the location of these measurements in the active channel. The ground-water seepage and hydraulic-head measurements were used to calculate ground-water flux, vertical hydraulic gradient, and the vertical hydraulic conductivity of the stream-bottom sediments. The minipiezometers were also used to collect ground-water samples from the alluvial aquifer immediately beneath the stream bottom. The general features, method of installation, measurement procedures and analysis of data collected are described in detail by Lee and Cherry (1978). Lee (1977) describes several case histories where the minipiezometers and seepage meters have been used to collect field data.

Hydraulic heads in minipiezometers were measured relative to the free surface in the stream using a meter stick. The vertical hydraulic gradient was calculated from the relative head measurement and the depth of the midpoint of the minipiezometer well screen beneath the stream bottom.

Ground-water seepage is measured using a seepage meter. Seepage meters were constructed by cutting 10-inch end sections from a 55-gallon metal drum. A small 1-inch diameter hole was cut in the circular top of each end section. During seepage measurement the hole is fitted with a rubber stopper containing a short section of glass tubing. The glass tubing serves as a connection between the drum and a plastic bag that is used to collect the seeping water during measurement. The seepage meter is pushed slowly into the sediment and tilted slightly to vent the trapped air through the hole in the top of the drum. A plastic bag is fitted over the glass tubing and secured

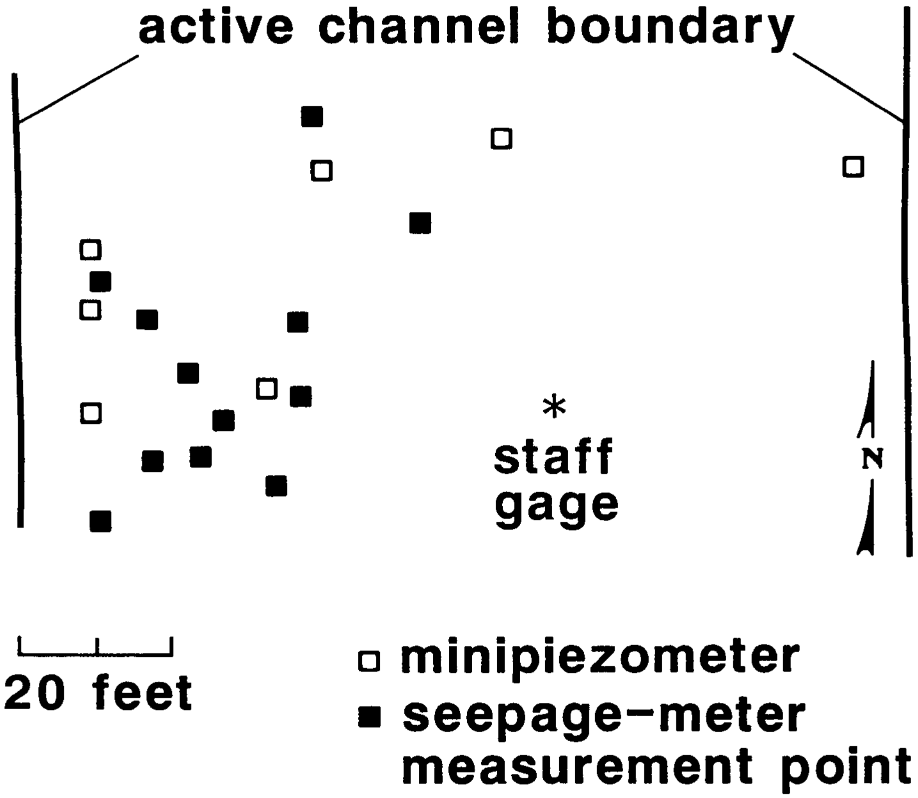

Figure 5.12 Location of seepage meter and minipiezometer measurements made in the stream bottom of the Smoky Hill River at the field site.

with a rubber band. The bag is then allowed to fill with water for a certain period of time. At the end of the measurement period, the bag is removed.

The volume of seeping water collected and the measurement time period are used to calculate the Darcy velocity or the ground-water seepage rate, q, from:

$$q = (0.439) \frac{Q}{At} \tag{5.6}$$

where Q is the total volume of water collected during the measurement period in liters, A is the cross sectional area of the drum in m^2 and t is the measurement time interval in minutes. Using this formulation the seepage has the units of feet/day.

The vertical hydraulic conductivity, K, of the stream bottom can be calculated from the Darcy equation:

$$K = q/i \tag{5.7}$$

where q is the specific discharge calculated from the seepage measurements, and i is the vertical hydraulic gradient calculated from hydraulic-head measurements taken in the minipiezometers. The vertical hydraulic conductivity is calculated in units of feet/day.

5.6 Ground-water Chemical-quality Sampling Techniques

Ground water samples were collected from all wells and minipiezometers to define the location and nature of the freshwater/saltwater transition zone and to locate areas of saltwater upconing. All of the monitoring sites were sampled under low streamflow conditions. Samples were collected carefully to minimize contamination from external sources and to ensure representative sampling.

Prior to sampling, the wells and minipiezometers were developed by evacuating all stagnant water in the casing and in the immediate area of the well screen. This task was accomplished by two different methods. Piezometers and continuously screened wells were initially developed by using an air-compressor pump that discharged water at about 3 gallons per minute. During pumping the air and water discharge lines were moved up and down in the well periodically to resuspend any sediment in the well-bore. Pumping was continued until the discharge water was clear. Air-pumped samples were collected immediately after development of the well and stored in 500-ml air-tight containers. After collection, containers were packed in ice to prevent dissolved gasses from coming out of solution and to maintain chemical equilbrium. This method of obtaining water samples was used for the September 1984, March 1985, and July 1985, collection times.

In addition to pumping, samples were also collected by bailing. Each well was developed by continued bailing with a six-foot PVC bailer until at least one well-casing volume of water (equivalent to the total amount of stagnant water in the casing before bailing) was removed from the well. The water sample was then collected by one final bailing and then stored as discussed above. This method was used for the November 1985, collection period.

Ground-water samples were also collected from the minipiezometers installed in the active channel of the stream bed during the July 1985, sampling period. Sample collection methods similar to those discussed above were used to sample the minipiezometers except that the scale of the apparatus and development time were greatly reduced. Each minipiezometer was developed before sampling by the use of a rubber bulb. These samples were taken only once during the project because the minipiezometer network was destroyed during a flood in October 1985, and could not be re-established.

Ground-water samples were analyzed to determine the concentration of chloride (Cl^-) and sulfate (SO_4^-) in solution and the amount of total dissolved solids. The specific gravity of each sample was determined from filtered samples by calculation using a known volume of sample and weighing the mass of the insoluble residue at 180°C. Specific conductance at 25°C was also measured on the filtered sample. Appendix A contains the complete results of all chemical analyses.

5.7 Measurements of Hydraulic Conductivity

Slug tests were performed in all piezometers to estimate the *in situ* hydraulic conductivity of the aquifer material in the vicinity of the five-foot well screen. The pieozmeter-recovery method of Hvorslev (1951) was selected as a simple and easily interpretable method. In the Hvorslev method, the rate of inflow to the piezometer tip at any time is proportional to the hydraulic conductivity and the unrecovered head difference (Figure 5.13; Cedergren, 1967):

$$q = FKh = FK\,(z-y) \qquad (5.8)$$

where h is active hydraulic head; K is hydraulic conductivity; F is shape factor; (z-y) is unrecovered head difference; and q is rate of flow of water into the piezometer. The shape factor, F, is a term which takes into account the shape and dimensions of the piezometer intake and hydraulic boundaries near the piezometer screen.

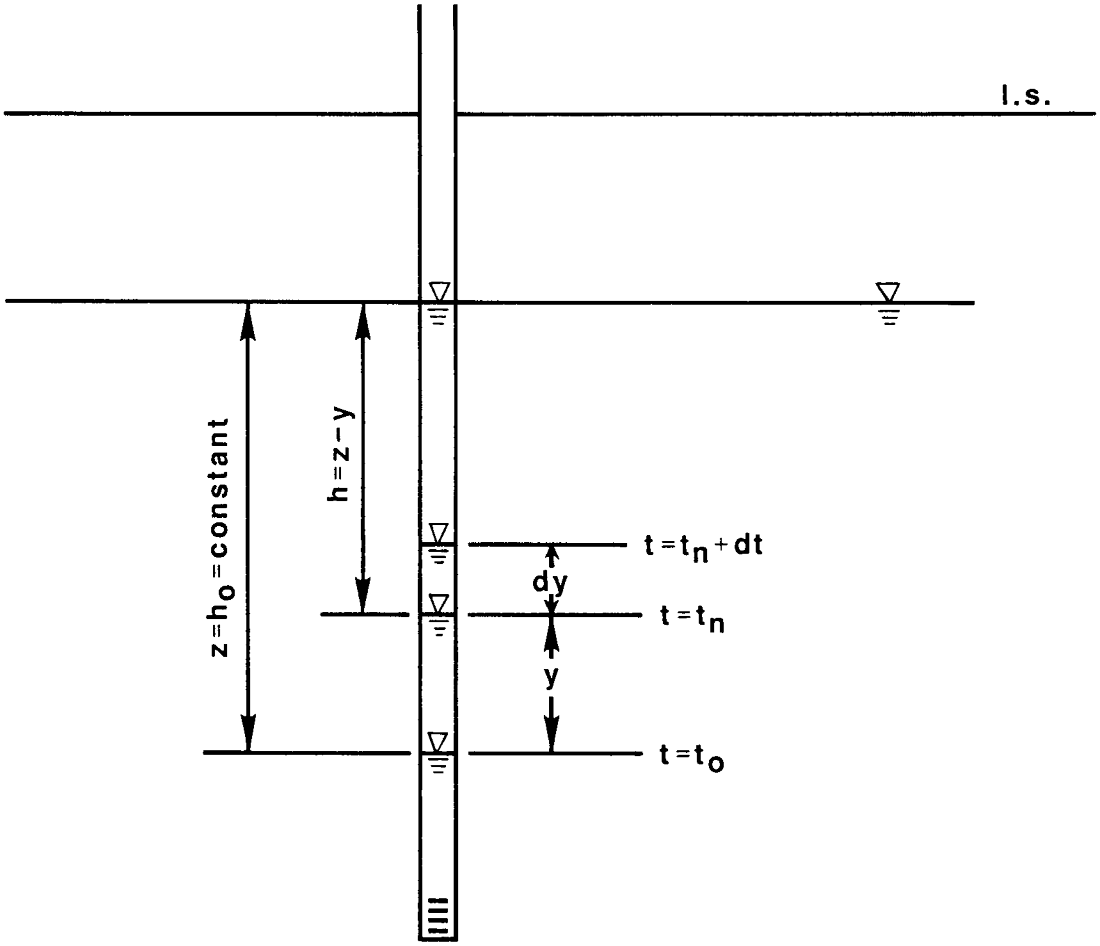

Figure 5.13 Cross-section of a single-well "slug" test in a piezometer.

Considering the volume of flow during a small time increment, dt, and assuming that friction losses in the pipe can be neglected, the following equation can be written:

$$qdt = Ady \qquad (5.9)$$

where A is the cross sectional area of the standpipe and y is the distance from the initial static water level (reference level) in the piezometer to the transient water level.

In addition, Hvorslev defined the time required for the complete equalization of the head difference if the initial rate of inflow were maintained as the basic time lag, T, and equated it as:

$$T = \frac{A}{FK} \qquad (5.10)$$

Equation 5.9 may be rewritten as:

$$\frac{dy}{(z-y)} = \frac{dt}{T} \qquad (5.11)$$

Equation 5.11 is the basic differential equation for the hydrostatic time lag and the solution is a semilogarithmic relation between the head ratio h/h_o and the time-lag ratio t/T:

$$\frac{t}{T} = \ln \frac{h_o}{h} \qquad (5.12)$$

where t is the time after the test began and the other parameters are as they were previously defined in the text or on Figure 5.18. The equalization ratio, E, is:

$$E = 1 - \frac{h}{h_o} = 1 - e^{-\frac{t}{T}} \qquad (5.13)$$

The hydraulic conductivity of the aquifer material in the vicinity of the piezometer well screen is computed graphically by plotting the head ratio, h/h_o, against time, t, on a semilogarithmic paper, fitting a straight line through the data, and reading T when the head ratio is 0.37 (i.e. when $\ln(h/h_o) = -1$). The value of the hydraulic conductivity K can then be computed by rearranging equation (5.10):

$$K = \frac{A}{FT} \qquad (5.14)$$

Values of the shape factor were computed from the geometry of the piezometer (Spangler, 1963):

$$F = \frac{2\pi L}{\ln (L/R)} \qquad (5.15)$$

where R is inside radius of the casing; and L is length of the well screen.

As a check, another form of the Hvorslev formulation was used to determine the hydraulic conductivity, assuming the horizontal component, K_h is equal to the vertical component:

$$K_h = \frac{d^2 \ln(\frac{2L}{D})}{8LT} \qquad (5.16)$$

where d is diameter of the piezometer; D is diameter of the intake; and L is length of the intake.

The Hvorslev method of recovery testing assumes that the formation surrounding a piezometer is homogeneous, isotropic, infinite in extent, and incompressible. Certainly, field conditions at the Smoky Hill study area deviate from these ideal conditions, but it is assumed that any deviations have only a minor effect on the computed hydraulic conductivities. Anisotropic conditions between vertical and horizontal hydraulic conductivities probably represent the largest source of error. Furthermore, for those wells which were drilled using a rotary mud method, a skin effect (Schalla, 1986) resulting in a decrease in hydraulic conductivity has affected the measurements. It should be noted that hydraulic conductivities computed by the recovery method give local estimates of aquifer materials surrounding the piezometer screens. The surrounding materials include both the disturbed zone around the well screen and the undisturbed aquifer matrix. As a result the condition of the disturbed zone may profoundly affect the estimate of hydraulic conductivity calculated from the recovery test and may not reflect the true value of hydraulic conductivity for the porous media (Freeze and Cherry, 1979).

Both displacement (slug) and bail-type recovery tests were performed in the piezometers to generate recovery data. Displacement-type tests were run by rapidly raising the static-water level in the two-inch piezometer by dropping 15 feet of one-inch pipe, sealed at the end, below the water level in the well. Bail-type tests were conducted by rapidly lowering the static-water level by lowering a five-foot PVC bailer into the piezometer, waiting for the water level in the piezometer to re-equilibrate, then rapidly removing the bailer. Both types of tests gave comparable results but the bail type proved to be easier to perform.

Water levels in the piezometers were measured and recorded in both displacement and bail test using a pressure transducer connected to an In Situ Inc. SE-1000 Hydrologic Monitor. This instrument records the height of the water column above the tip of the pressure transducer in feet with an accuracy of ±1% of the range of the transducer (100 psi). A logarithmic-sampling mode was used during each test in which samples were collected continuously using 0.2-second to 30.0-second time intervals. The recovery tests generally lasted under two minutes but recording continued for a full 10 minutes.

The hydraulic conductivities calculated from the slug tests showed a wide range of variation from 4 to 403 feet/day. The reliability of the test results was determined by examining the semi-log plot of head ratio vs. time. If the data showed considerable non-linearity, the test results were not considered valid. The results of the single well tests were also examined to determine the effects of drilling fluids on the aquifer matrix in the vicinity of the piezometer well screen. Figure 5.14 shows the frequencies of occurrence of hydraulic conductivities arranged by classes, aquifer type, and drilling technique. Each hydraulic conductivity class has a range of 50 ft/day. Test-holes for piezometers drilled in the alluvial and bedrock aquifers with mud rotary methods and in the alluvial aquifer with hollow-stem auger techniques are represented in the figure. The hydraulic conductivities of the alluvial aquifer in the vicinity of piezometers drilled using mud rotary methods are almost an order of magnitude lower than those where hollow-stem auger techniques were used. This shows that the drilling mud has substantially affected the aquifer materials surrounding these wells even

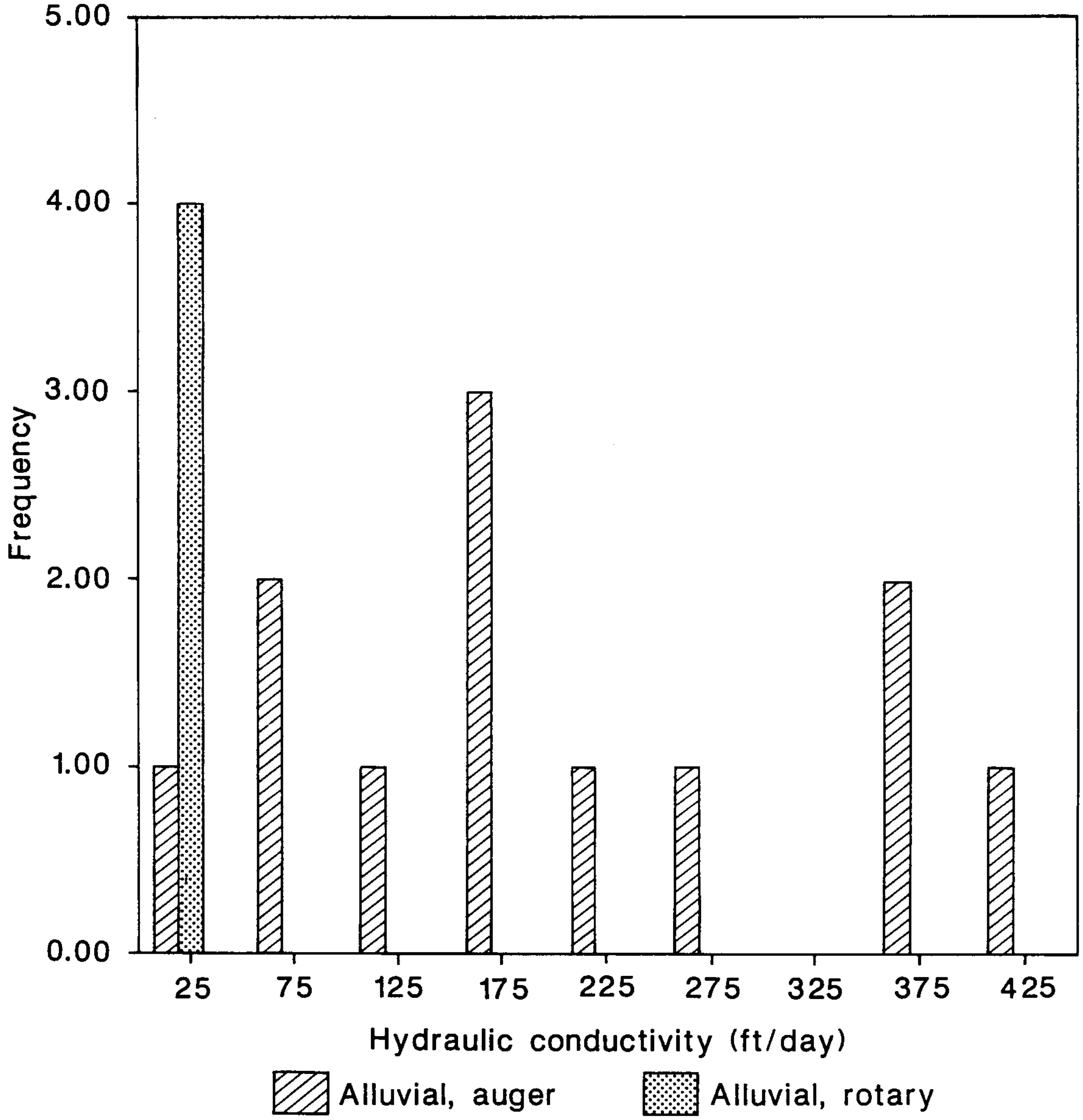

Figure 5.14 Frequency distribution of hydraulic conductivities from slug tests of piezometers arranged by drilling method and aquifer type.

though considerable effort was expended to develop the wells and remove the accumulated fine sediment associated with drilling.

6. RESULTS OF THE FIELD INVESTIGATION

6.1 Definition of the Aquifer and Aquitard Units at the Field Site

The aquifer and aquitard units at the field site were defined on the basis of the site geology, hydrologic properties and observations of hydrologic behavior during the course of the field investigation. Three major units were defined: an alluvial aquifer, an aquitard consisting of the Wellington Formation, and a bedrock aquifer consisting of the Herrington Member of the Nolans Limestone. Other bedrock aquifers exist beneath the Herrington, but they have little impact on the local stream/aquifer system.

The distribution of lithofacies within the different units was shown in Figure 6.1, which was constructed using samples of cuttings from test-holes and gamma-ray logs at all sites and the core material collected at monitoring site C. As can be seen from the cross sectional view of the geology, a complex mosaic of lithofacies exists at the field site within both the unconsolidated aquifer and the aquitard-bedrock units. A detailed description of the various geologic units of the field site is given in Appendix B.

The alluvial aquifer adjacent to the Smoky Hill River consists of a fining-upward sequence of alluvial sediments that range in texture from coarse sands and gravels to silt and clay. Saturated thickness of the alluvial aquifer within the study area is approximately 40 feet and varies little due to the regularity of the bedrock surface beneath the alluvium. Recharge to the alluvial aquifer comes from: (1) precipitation falling on the land surface and percolating through the unsaturated zone to the water table; (2) lateral water movement from the Smoky Hill River when streamflow is above base-flow; and (3) vertical water movement upward as leakage through the Wellington shale from the bedrock aquifer in the Herrington. Discharge from the alluvial

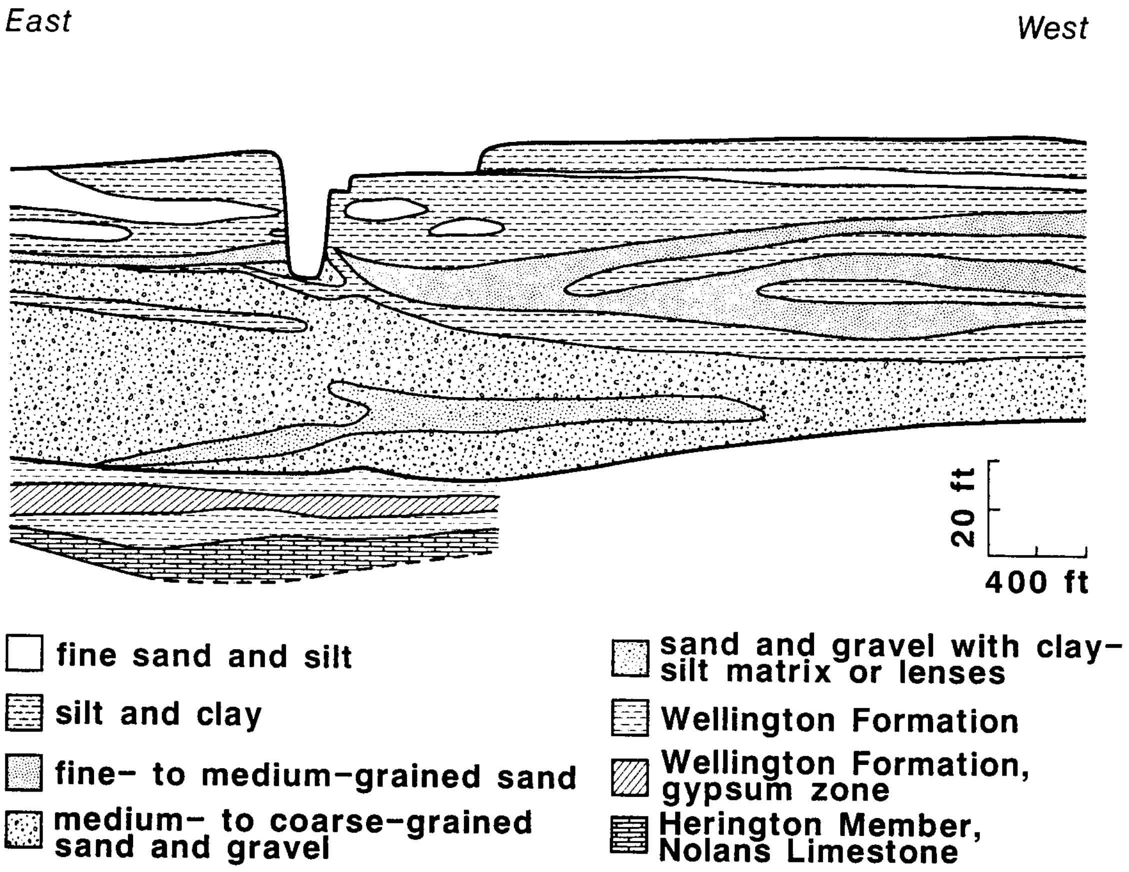

Figure 6.1 Geologic cross-section of the field site between monitoring sites I and B.

aquifer is to the stream under most streamflow conditions and into the bedrock aquifer during recharge events that affect the stream/alluvial aquifer system.

The bedrock aquitard in the Wellington Shale consists of the fractured and weathered Wellington shales. The thickness of the aquitard ranges from 10 to 16 feet. Very little information is available at this time concerning the hydrologic properties of this unit. Ground-water flow through the aquitard is believed to be through conduits created by the fracturing of the shales and solution cavities in the bedded evaporites contained in the formation.

The bedrock aquifer in the Herrington Member of the Nolans Limestone consists of the fractured and solutioned gypsiferous dolomites and dolomitic shales contained in the bedrock.

6.2 Hydraulic-conductivity Measurements

A corrected listing of *in situ* hydraulic conductivities in the alluvial aquifer is given in Table 6.1. The values in Table 6.1 exclude test results believed to have been affected by drilling mud during well construction. Values range from a minimum of 18 ft/day in piezometer I-2 to a maximum of 403 ft/day in piezometer I-1.

A plot of observed hydraulic conductivity on a logarithmic-probability paper closely approximates a straight line (Figure 6.2). This suggests that values of hydraulic conductivity from the Smoky Hill River study area are approximately log normally distributed. Some deviation from log normality is expected because of the simplifying assumptions implied in the analysis of the slug test data. The straight line shows that a unimodal distribution adequately describes the variation of hydraulic conductivity in the alluvial aquifer. The geometric mean of this distribution is 153 feet/day.

The spatial distribution of hydraulic conductivity of the alluvial aquifer at the Smoky Hill River study area is presented in Figure 6.3. The

Piezometer	Hydraulic Conductivity ft/day
A-1*b	11.9
B-2*b	45.5
C-5*b	20.6
D-1*	30.3
F-1*	35.1
H-2	71.2
H-1*	16.6
I-2	17.7
K-2	123.0
A-1*b	6.3
C-2	84.7
I-1	403
G-1*	18.8
G-3	282
M-3	378
M-2	178
M-5*b	4.1
B-3	215
D-3	384
C-4	175
D-5	157

* Installed using mud rotary methods

b Piezometer well screen in bedrock

Table 6.1. Hydraulic conductivities computed from slug test results.

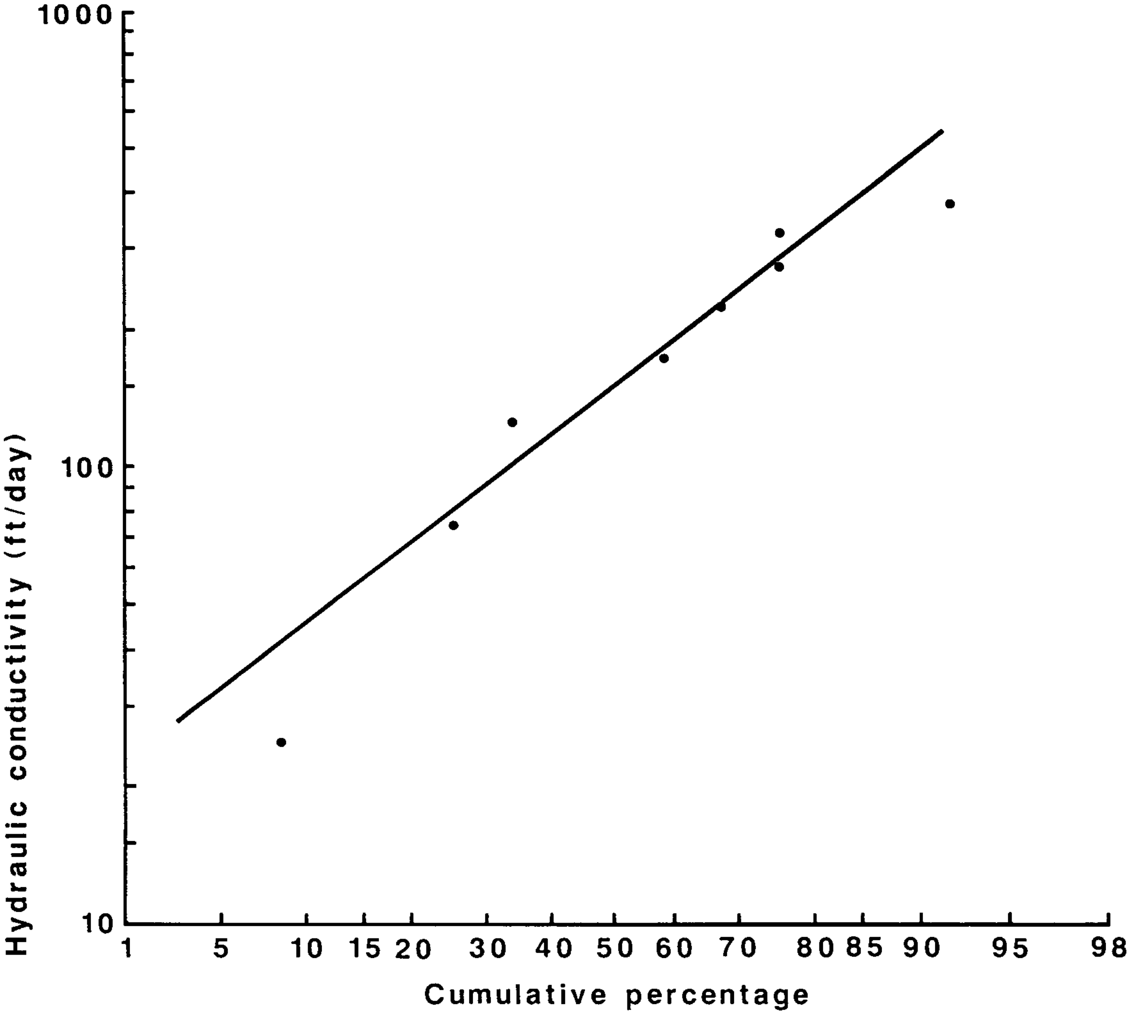

Figure 6.2 Log-probability plot of the estimated hydraulic conductivities.

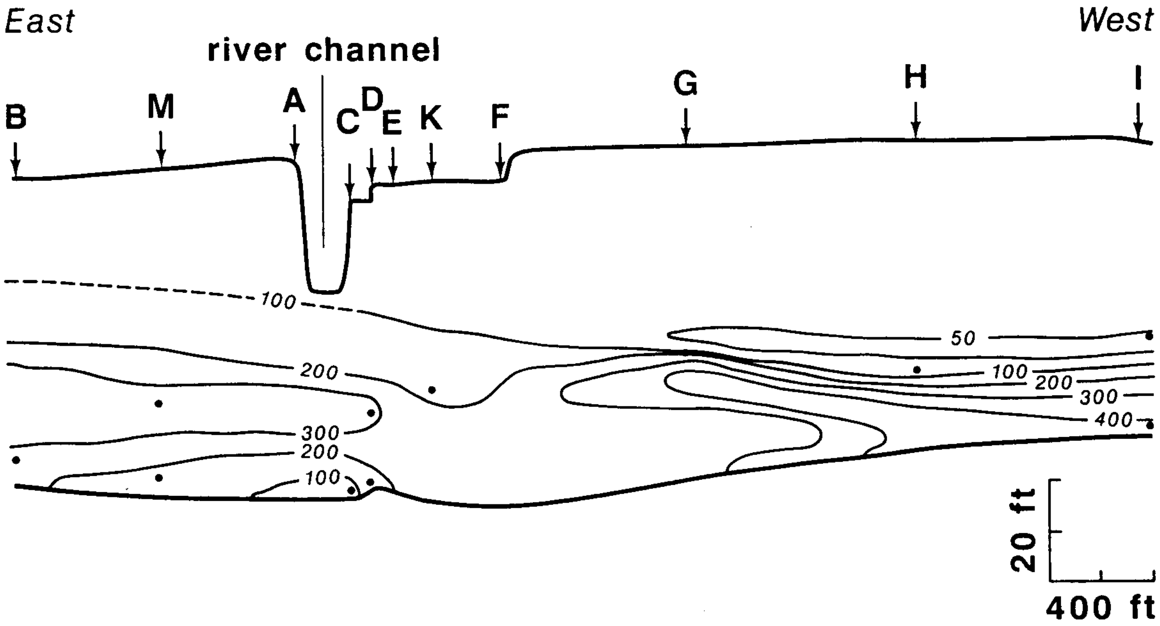

Figure 6.3 Variation of the hydraulic conductivity (ft/day) in the field cross-section.

distribution shows a complex pattern of highs and lows and underscores the overall geologic and hydrologic complexity of the alluvial sediments. However, the overall pattern of the distribution can be interpreted in terms of local geology. Hydraulic conductivities in the range of 200 to 400 ft/day are associated with coarse sands and gravels found in the lower part of the alluival aquifer. Hydraulic conductivities that range from approximately 100 to 300 ft/day are probably associatd with fine to medium grained sands. Values less than 100 ft/day are probably associated with the more fine grained sand and silt-size sediments.

The aquitard and bedrock at the field site are much less conductive of water than the overlying alluvial sediments. The average hydraulic conductivities (geometric mean) are 15 feet/day and 6 feet/day for the vuggy fractured dolomites of the Herrington Member of the Nolans Limestone and the weathered Wellington shale beneath monitoring site A, respectively. However, the data that were used to determine these mean values are difficult to evaluate since the bentonite mud used to drill the test-holes has probably affected the rock matrix in the vicinity of the piezometers by plugging off some of the secondary permeability of the rock.

The results of the seepage rate and hydraulic-head measurements and the calculated hydraulic conductivities at the stream bottom are summarized in Table 6.2. Values of vertical hydraulic conductivity range from 0.34 to 1.93 feet/day. The geometric mean of these measurements is 0.74 feet/day. The vertical hydraulic conductivity of the stream bed increases progressively to the center of the stream. This observation is supported by the fact that the texture of the bottom sediments coarsens towards the center of the stream. Towards the west bank, the bottom consists of fine- to medium-grained sand, whereas the middle of the stream bottom consists of medium to coarse sand and

Location	Volume of Fluid Collected (ℓ)	Time (Hrs.)	Vertical Hydraulic Gradient	Hydraulic Conductivity (ft/day)
SM1	0.54	1.20	0.22	0.62
SM2	0.28	0.80	0.22	0.45
SM3a	0.85	1.14	0.22	1.02
SM4	0.23	0.95	0.22	0.34
SM5	0.22	0.49	0.22	0.57
SM6	0.53	0.89	0.22	0.82
SM7	0.30	0.90	0.22	0.45
SM8	0.42	0.93	0.22	0.62
SM9	0.82	0.98	0.22	1.16
SM10	0.52	1.04	0.22	0.68
SM11	NO DATA			
SM12	0.61	0.95	0.10	1.93
SM13	0.09	0.98	0.14	1.42
SM14	NO DATA			

Table 6.2. Field data and estimated hydraulic conductivities from the seepage-meter tests performed in the stream bottom of the Smoky Hill River, July 1985.

gravel. The vertical hydraulic gradient in the shallow part of the alluvial aquifer also varies. Near the west bank the vertical gradients are on the order of 0.22 foot/foot, but near the center of the stream the gradient is 0.12 foot/foot. Near the east bank of the river the hydraulic gradient increases to approximately 0.05 foot/foot. The average vertical hydraulic gradient is estimated to be 0.12 for the whole width of the stream-channel cross section.

6.3 Changes in Ground-water Flow Conditions

Monitoring of ground-water conditions was carried out at the observation wells during the period of field investigation. The pressure density and elevation measurements were used to construct the hydraulic-head (defined in Section 5.3) distributions along the field cross section. General directions of ground-water flow may be inferred from changes in the hydraulic head.

Ground-water flow conditions and their response to the stream stage are illustrated in Figure 6.4 for July 31, 1985 (low-flow conditions), and in Figures 6.5 through 6.9 for the period between September 26 and November 27, 1985 (transient conditions). Ground-water flow in all of the cross sections presented except the one for October 16, 1985, is toward the stream according to the distribution of hydraulic head in the alluvial aquifer and the configuration of the water table. The seepage measurements made in the active channel of the river during the latter part of July 1985, are toward the stream according to the distribution of hydraulic head in the alluvial aquifer and the configuration of the water table. The seepage measurements made in the active channel of the river during the latter part of July 1985, indicated that the streamflow gain from seepage was approximately 0.52 cfs/mile. The observed seepage rate corresponds closely to an average low-flow gain from

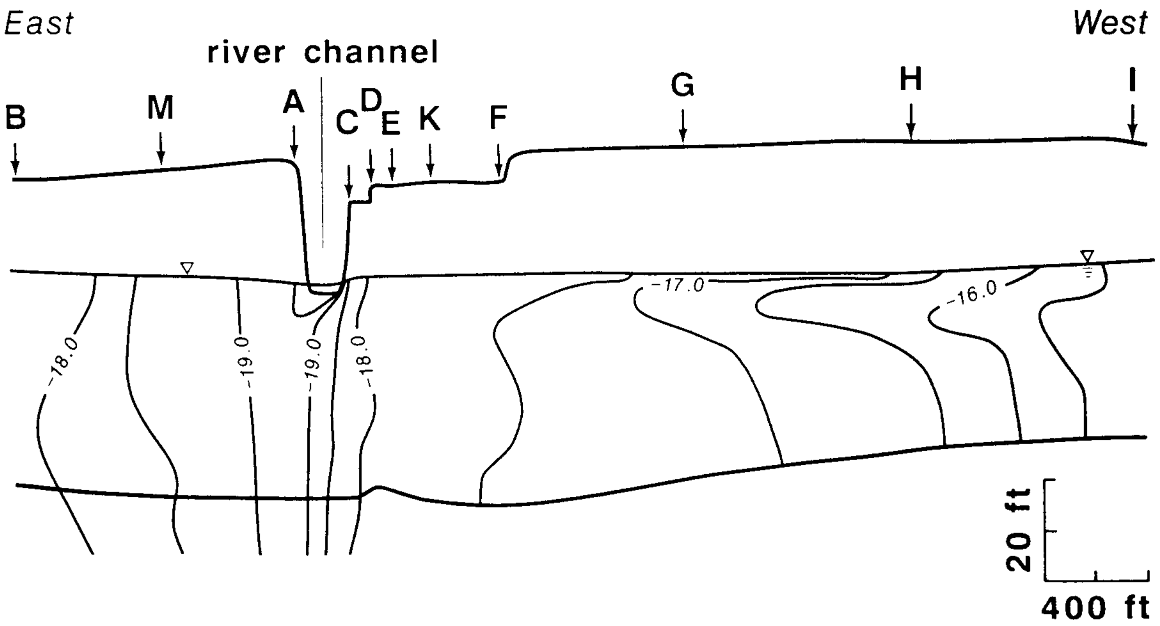

Figure 6.4 Hydraulic head distribution along the field cross-section on July 31, 1985.

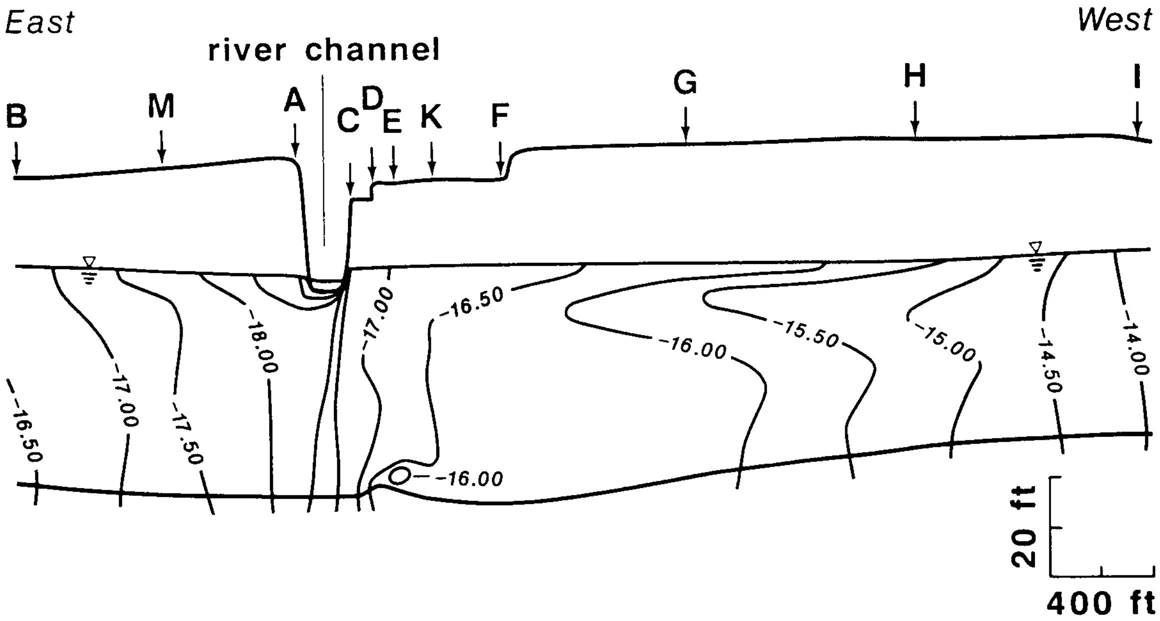

Figure 6.5 Hydraulic head distribution along the field cross-section on September 26, 1985.

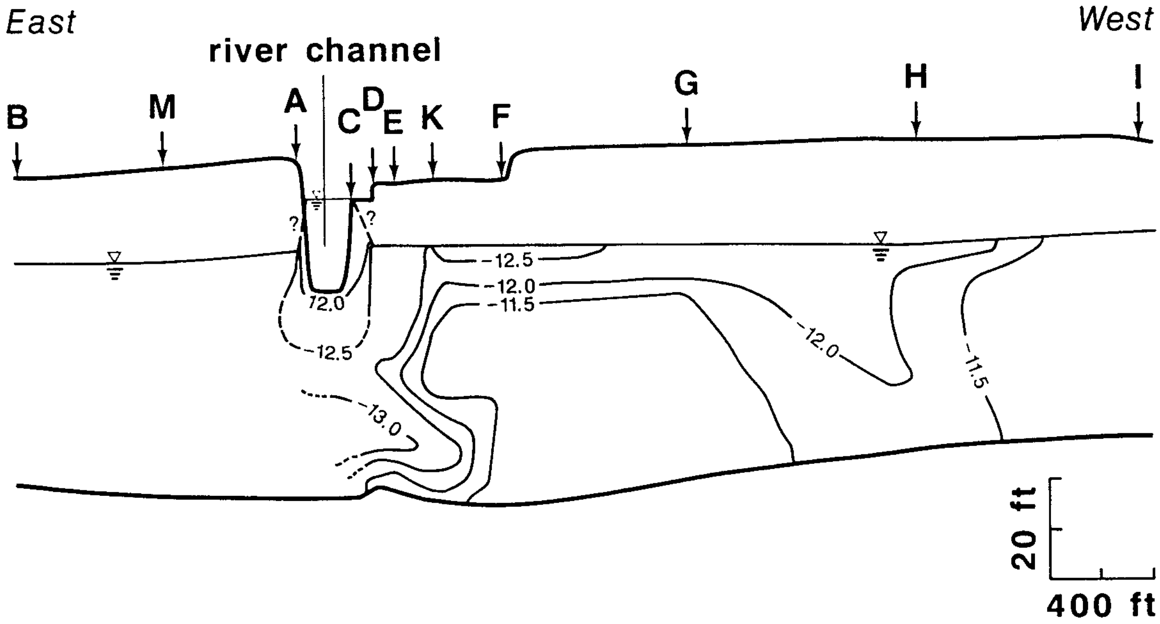

Figure 6.6 Partial distribution of hydraulic head along the field cross-section on October 11, 1985.

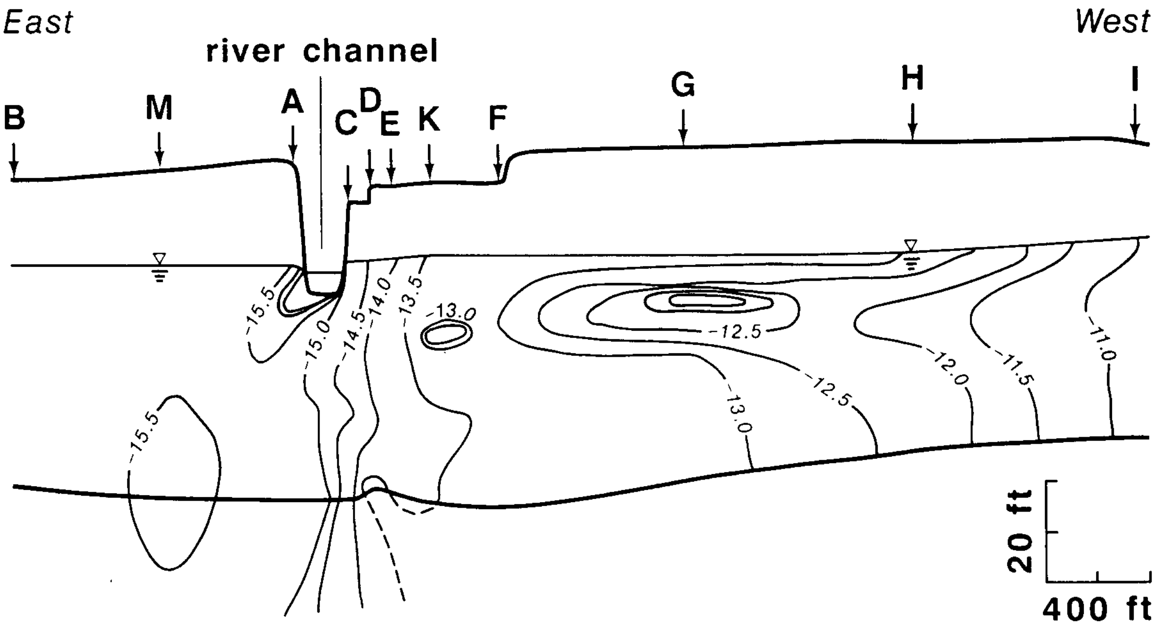

Figure 6.7 Hydraulic head distribution along the field cross-section on October 16, 1985.

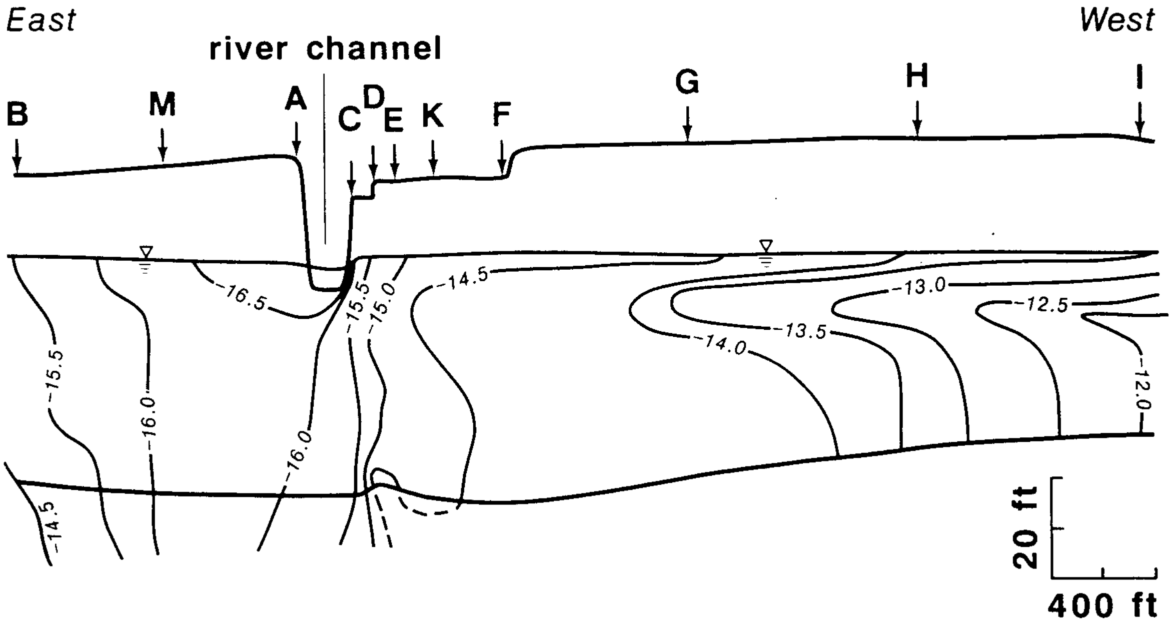

Figure 6.8 Hydraulic head distribution along the field cross-section on October 30, 1985.

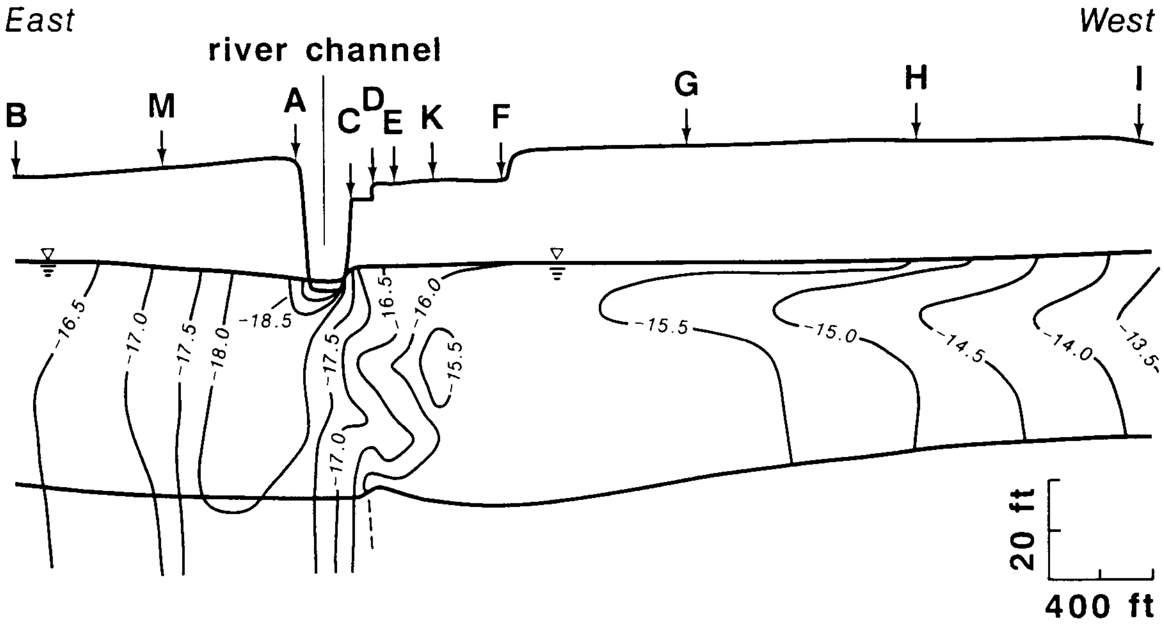

Figure 6.9 Hydraulic head distribution along the field cross-section on November 27, 1985.

seepage of 0.74 cfs/mile calculated from the streamflow records of the New Cambria, Enterprise, and Niles stream-gaging stations (see Section 3.4).

The slope of the water table away from the stream was generally much steeper on the west bank than on the east bank. The hydraulic-head low was located almost always to the east of the vertical centerline of the stream. This asymmetry may be due to the hydrogeologic complexity of the field cross section near the stream or may be caused by the regional ground-water flow directions being oriented perpendicular to the active channel of the Smoky Hill River at this site. Hydraulic-head gradients in the alluvial aquifer show the greatest change in the vicinity of the stream. Vertical hydraulic-head gradients ranging from 0.22 foot/foot on the west bank to 0.05 foot/foot on the east bank were measured in the field at low flow. West of the river, a layer of interbedded medium- to fine-grained sands and clay silts in the shallow part of the alluvial aquifer creates a sharp curvature in the hydraulic-head contours beneath monitoring sites G, H, and I.

Many changes take place in the stream/aquifer system during periods of recharge. As recharge is added to the system, the stream level rises in response to increased runoff and there is a general rise and flattening of the water table. Influent or effluent conditions will exist between the stream and the aquifer depending on the amount of direct recharge to the water table and rate of rise of the stream level. The partial set of measurements shown in Figure 6.6 was taken during a period of widespread flooding following a period of intense rainfall. During this flood event the stream level rose approximately 16 feet above the pre-flood level (Figure 6.10). The direction of ground-water flow in this case is from the stream to the aquifer.

During the time of flooding, ground-water levels also rose dramatically. Figure 6.11 shows the hydrographs of the continuously screened wells in

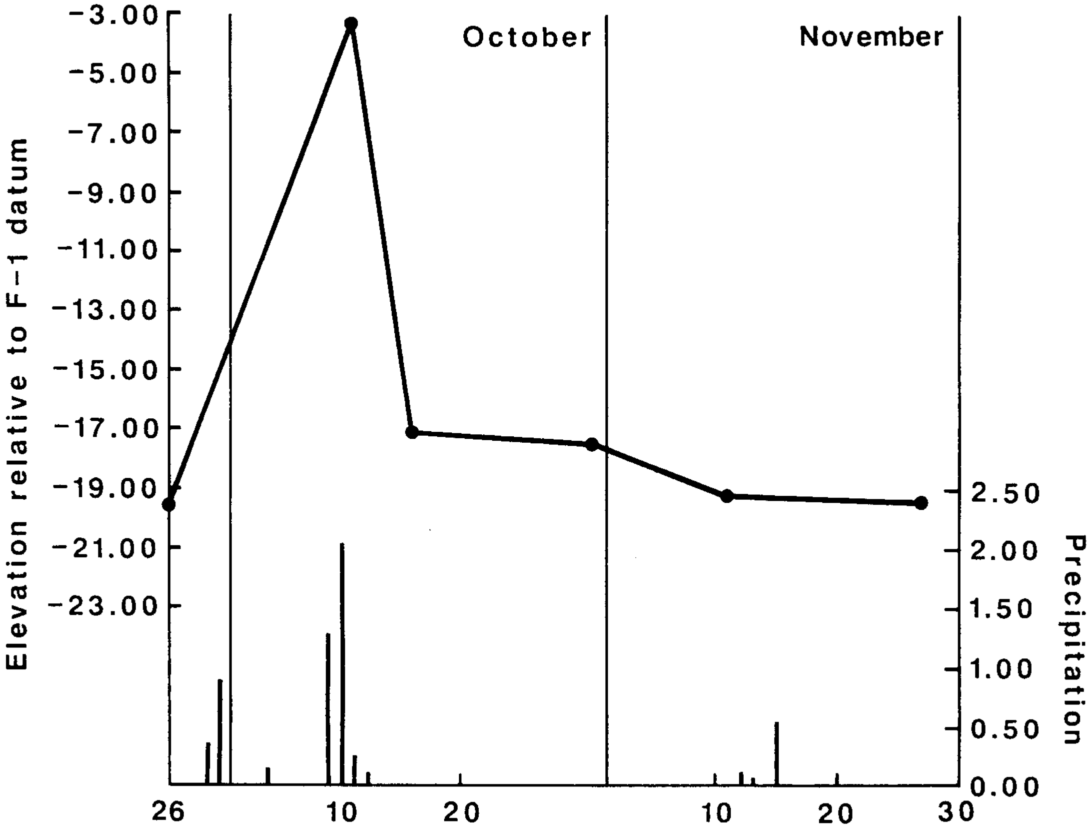

Figure 6.10 Stream stage measurements and precipitation records for the period between September 26 to November 30, 1985.

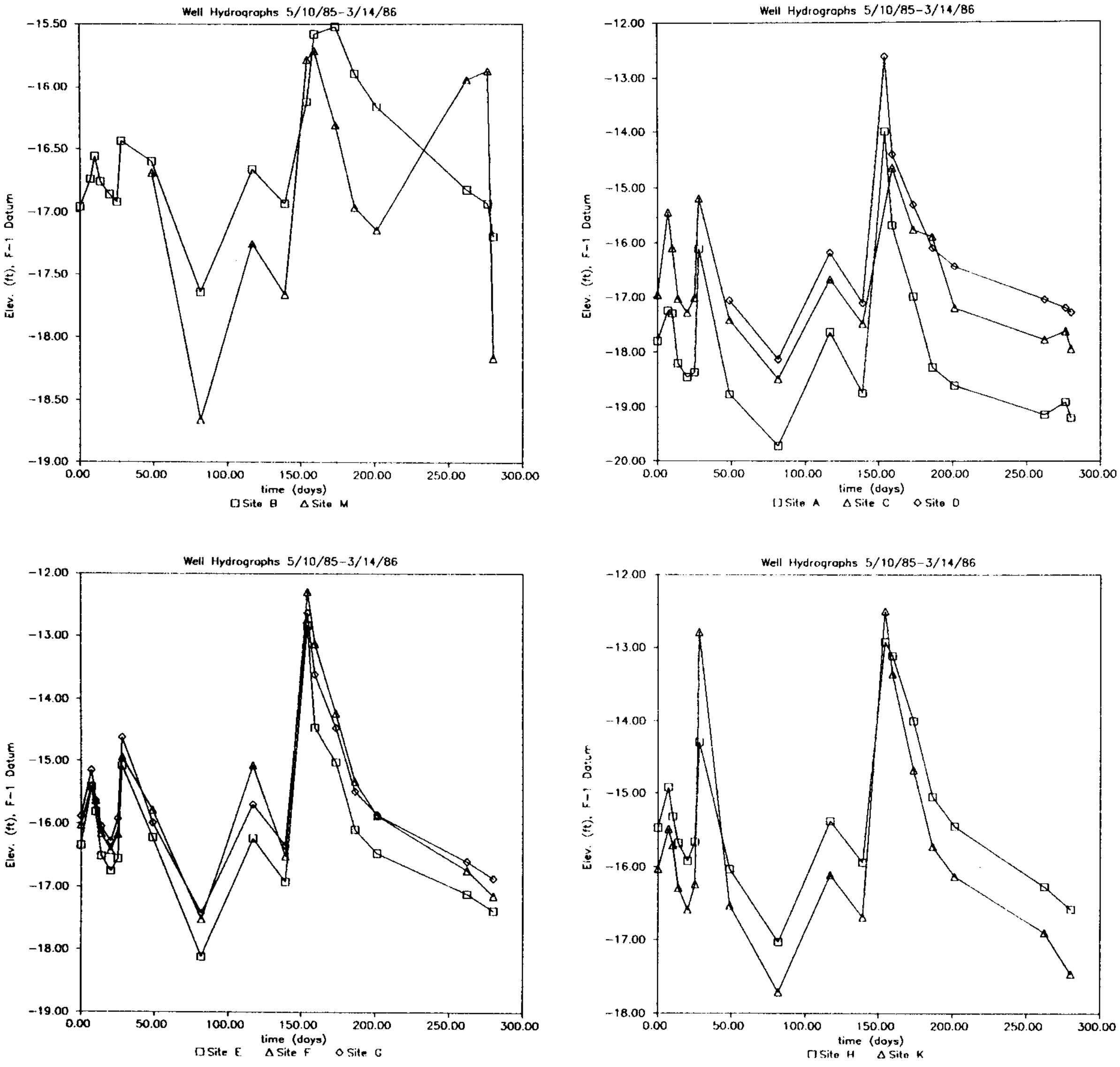

Figure 6.11 Ground-water level hydrographs for different sites for the period between May 10, 1985 and March 14, 1986.

the monitoring network showing fluctuations of ground-water levels over time. Figure 6.12 is a stream-stage hydrograph for this time. These records show a rather sharp 2.5 to 5 foot rise in ground-water level recorded at all of the monitoring sites in response to the flood event. The rising of ground-water levels during the flooding did not lag behind the rise in stream level even at sites H and B which are approximately 3100 and 1200 feet away from the river, respectively. Note that the quick rise of water levels in the alluvial aquifer is caused mainly by the recharge from infiltration of precipitation and not by seepage from the river bed.

The recovery of ground-water levels to the pre-flood conditions was slower than the recovery of stream levels. The lengths of the recovery period were about the same for all of the monitoring sites regardless of distance from the river. Figure 6.10 shows that ground-water discharge to the stream resumed shortly after the passage of the flood (October 16, 1985). Figure 6.11 indicates that the general ground-water flow and water-table configuration was established at the field site by October 30, 1985. These observations suggest that the alluvial aquifer responds quickly to the changes in the hydrologic conditions at the field site.

Ground-water flow in the bedrock aquifer is principally in a lateral direction toward the hydraulic head low between monitoring sites A and M. The flow pattern in the bedrock aquifer is only slightly affected during periods of recharge or high streamflow. However, some upward leakage of ground water from the bedrock aquifer in the Herrington Member of the Nolans Limestone through the Wellington shale is indicated when the stream is at low flow.

6.4 Extent of the Saltwater Upconing

The lateral and vertical extent of the saltwater/freshwater contact zone was mapped at low-flow conditions in the river using surface resistivity

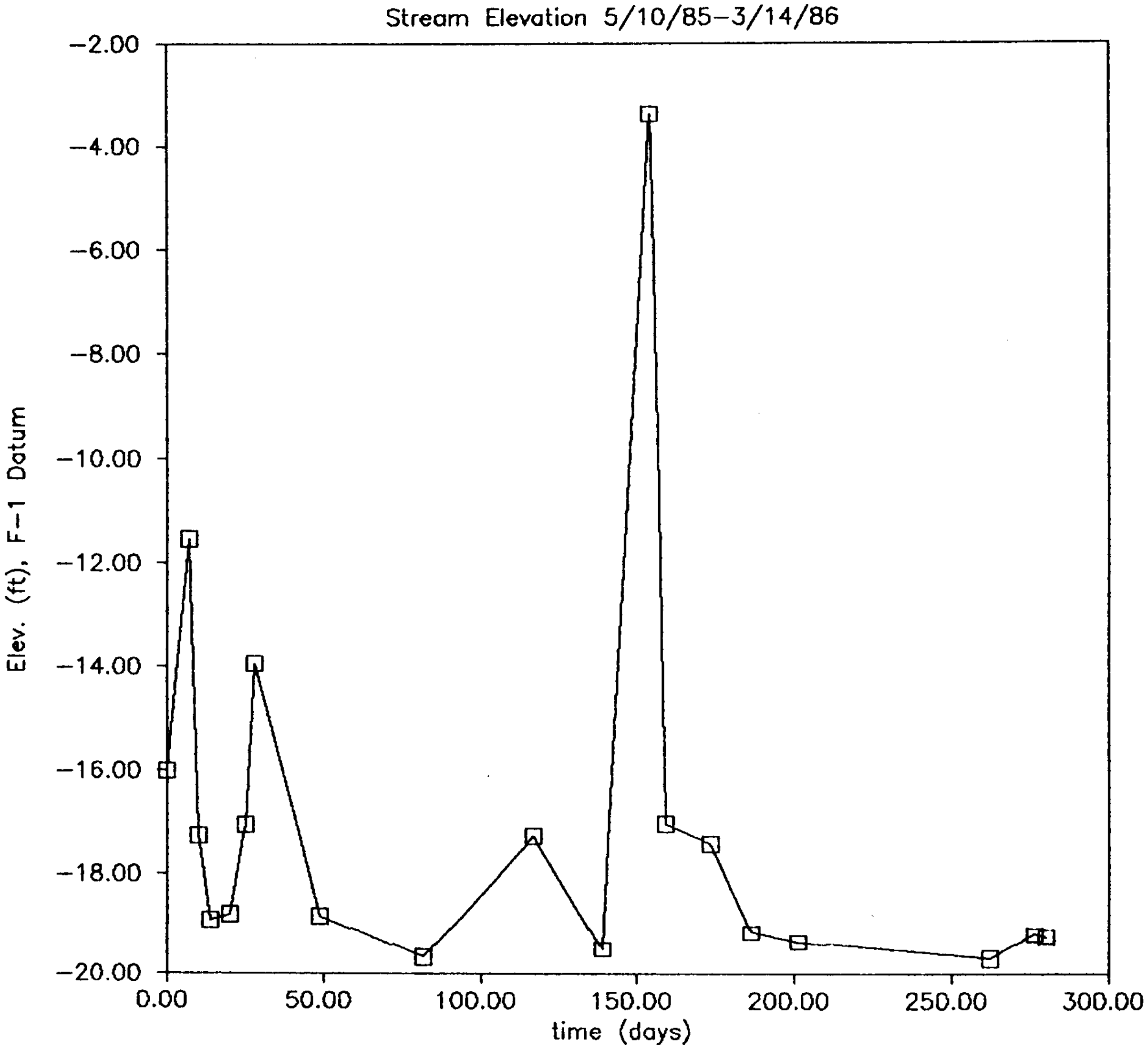

Figure 6.12 Stream-stage hydrograph for the Smoky Hill River at the field site for the period between May 10, 1985 and March 14, 1986.

techniques and the differential-pressure measurements (see section 5.4 for a description of these methods).

Figure 6.13 shows the distribution of apparent resistivities in the vicinity of the Smoky Hill River field site and the interpreted location of zones in the alluvial aquifer where saline ground waters are believed to be present at shallow depths (zones of saltwater upconing). The apparent resistivities are generally lower on the west side of the river than those on the east side because the alluvial sediments are generally more fine grained on the west side. Areas of high apparent resistivity are located north and south of the line of monitoring sites. Two "sources" of saltwater are outlined by the surveys. One body of saline water generally parallels the course of the river and crosses beneath the river near the line of monitoring sites. This plume moves with the easterly direction of ground-water movement in the alluvial aquifer. Another body of saline ground water is outlined by a north-south-trending area of low apparent resistivity east of the river. Outside of these areas the higher apparent resistivities indicate that the alluvial sediments are saturated with generally lower salinity waters.

The results of the apparent resistivity surveys are confirmed by the pressure-differential surveys in the continuously screened wells of the monitoring network. Figure 6.14 shows the variation in ground-water chemical quality computed from the reuslts of the July 31, 1985, pressure-differential survey when the stream was flowing under low-flow conditions. The overall shape of the saltwater-intrusion area shown in Figure 6.14 is asymmetrical with respect to the vertical center line of the river and is coincident with the hydraulic head low in the cross section. West of monitoring site D the upper part of the alluvial aquifer contains low-salinity ground waters. Closer to the river beneath site C, saltwater upconing occurs at shallow

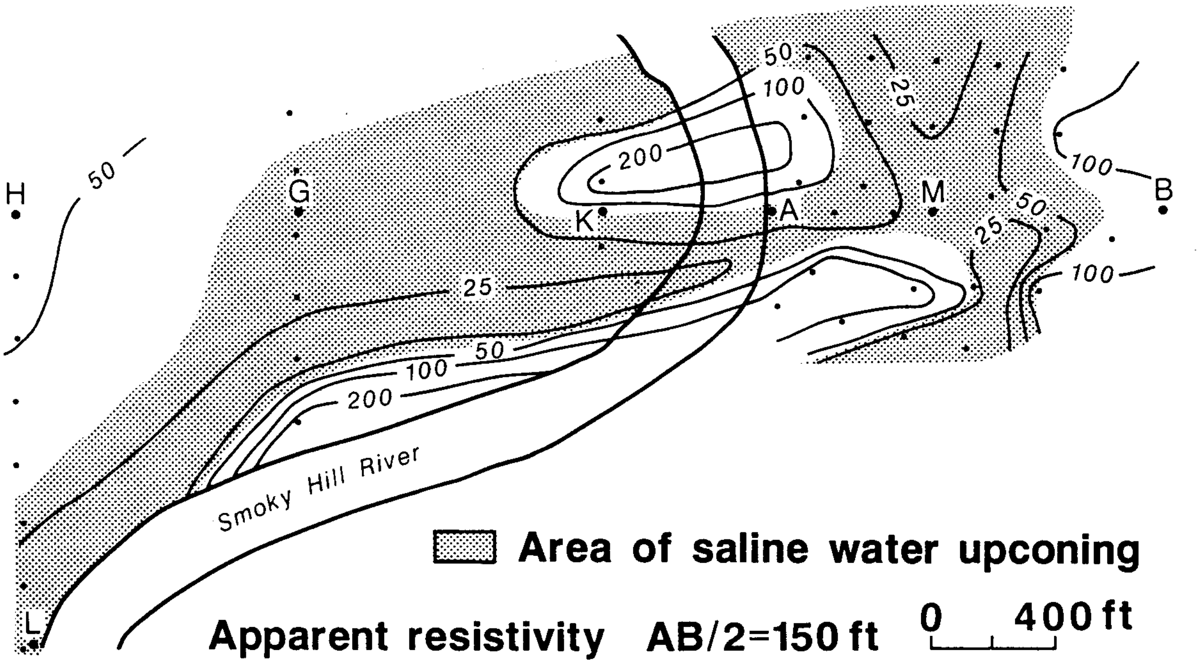

Figure 6.13 Areas containing saltwater at shallow depths in the alluvial aquifer.

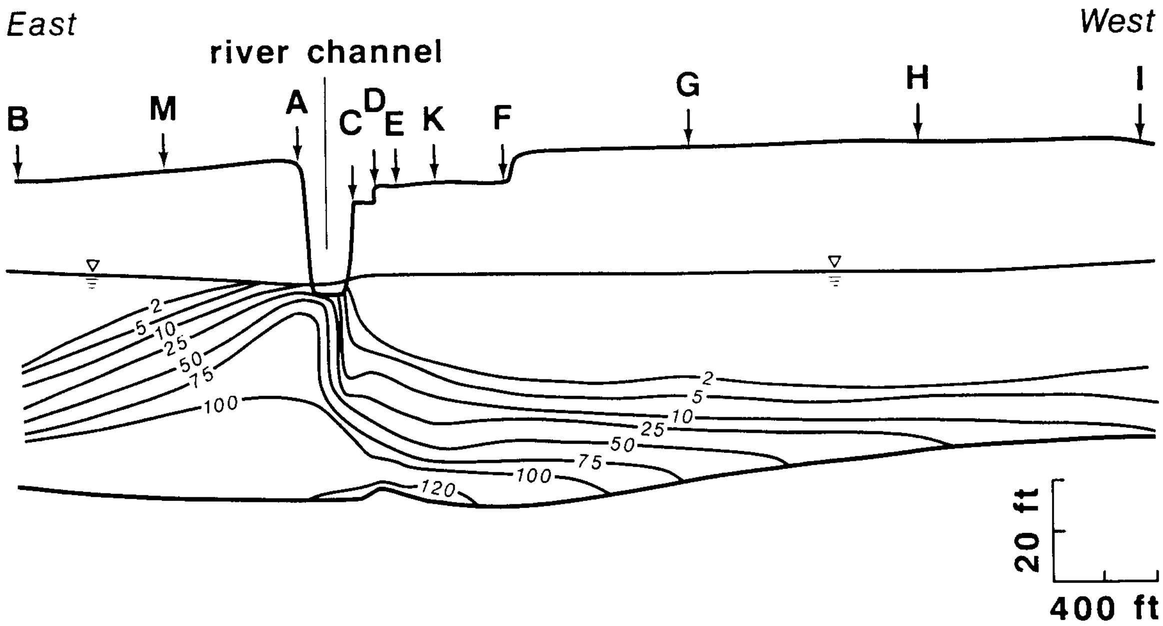

Figure 6.14 Distribution of total dissolved solids of ground-water at the field cross-section on July 31, 1985.

depths. At this point the slope of the west side of the saltwater-intrusion zone is almost vertical. East of monitoring site A the downward slope of the top of the saltwater-intrusion zone is much smaller than the slope at C. Farther to the east beneath site B the brines occupy the lower part of the alluvial aquifer. The denser brines (greater than 100,000 ppm total dissolved solids) are also contained in the lower areas of the bedrock formations. The thickness of the salt-dispersive zone assumed to be the area between the 2000 and 100,000 ppm TDS lines is 15 feet to 20 feet in the cross section. The concentration gradients change rather uniformly over much of the cross section except at site A where the ground-water dissolved solids increase rapidly beneath the stream. At this point saline waters with high chloride content are entering the stream.

The shape and configuration of the salt-dispersive zone is very much influenced by changes in the stream/aquifer conditions. These changes may result from variations in stream discharge or may be caused by water table rise due to increased natural ground-water recharge.

To observe the saltwater-upconing conditions during a changing hydrologic environment, we analyzed the data collected from September 26 to November 27, 1985. As indicated in the previous section, during this period heavy rainfall resulted in minor flooding of the river valleys. The stream level at the cross section rose from the September 26 level of -19.52 feet elevation (relative to the datum at monitoring site F) to -3.36 feet elevation. The preflood stream-level elevation indicates that the streamflow was near low-flow conditions.

Figures 6.15 through 6.19 show the temporal variation of total dissolved solids of ground water calculated from the differential-pressure measurements for the five sets of measurements made during the period between September 26

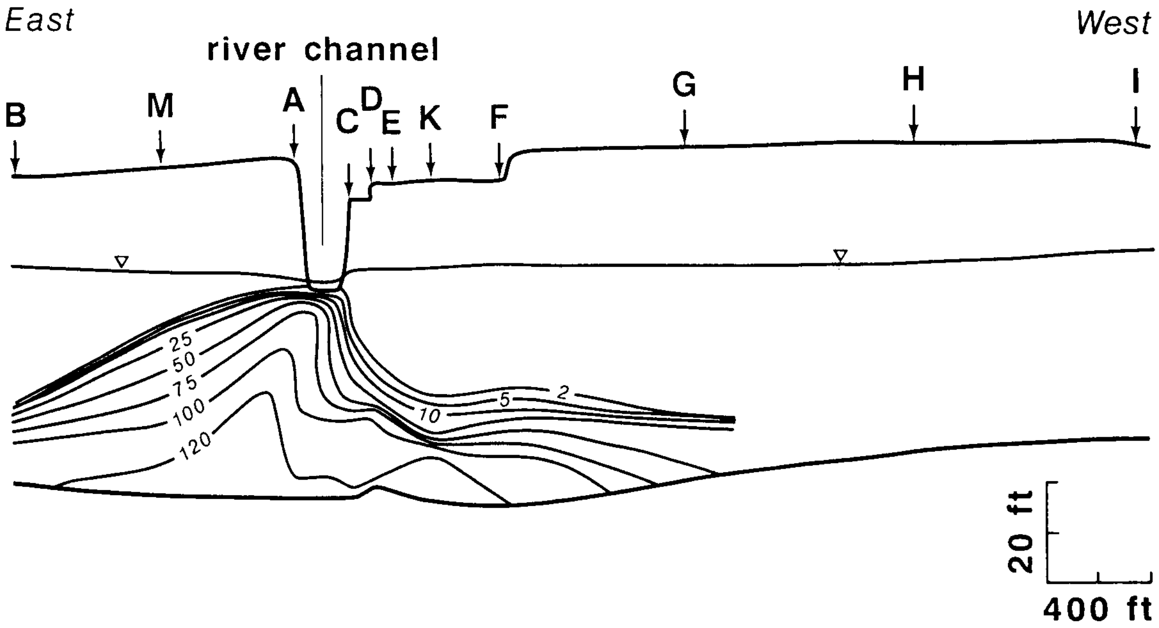

Figure 6.15 Distribution of total dissolved solids of ground-water at the field cross-section on September 26, 1985.

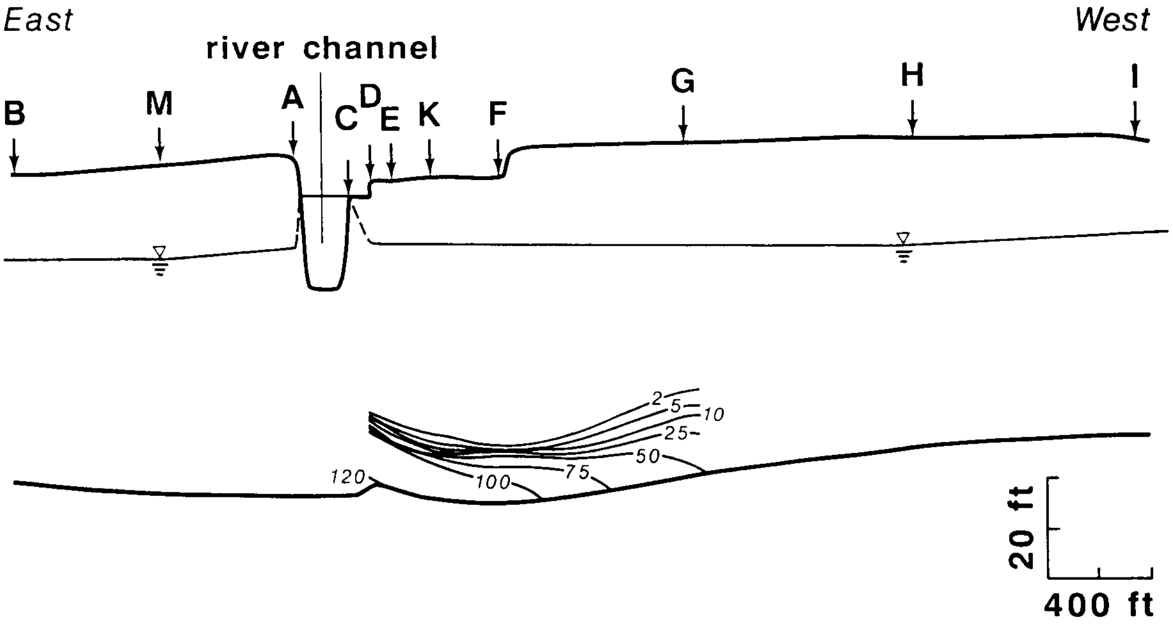

Figure 6.16 Partial distribution of total dissolved solids of ground-water at the field cross-section on October 11, 1985.

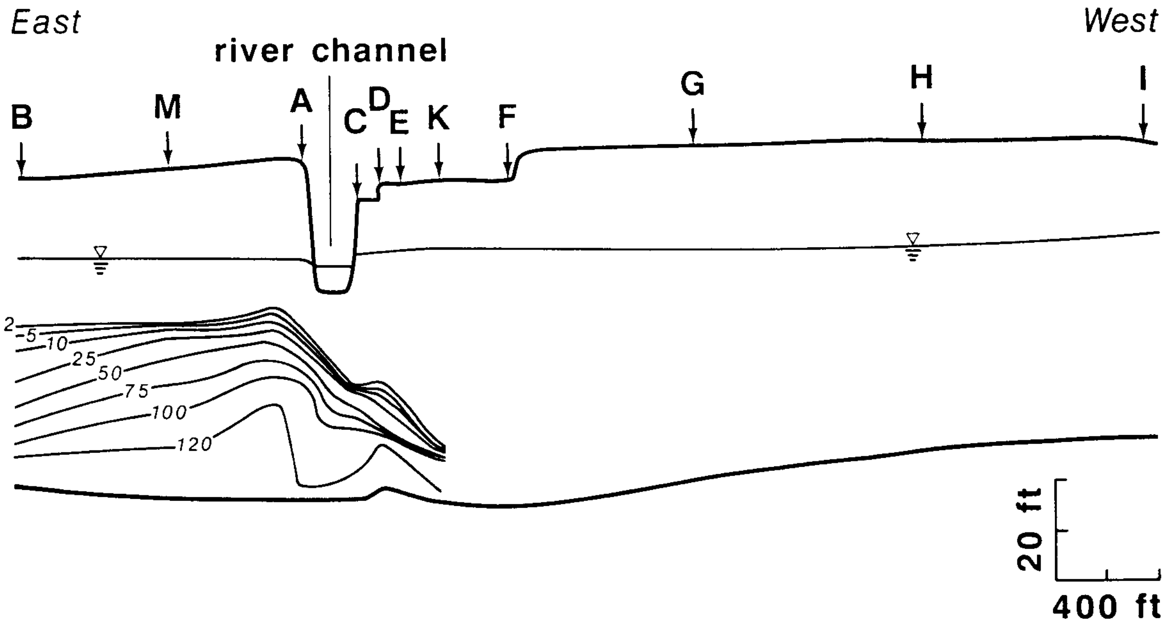

Figure 6.17 Distribution of total dissolved solids of ground-water at the field cross-section on October 16, 1985.

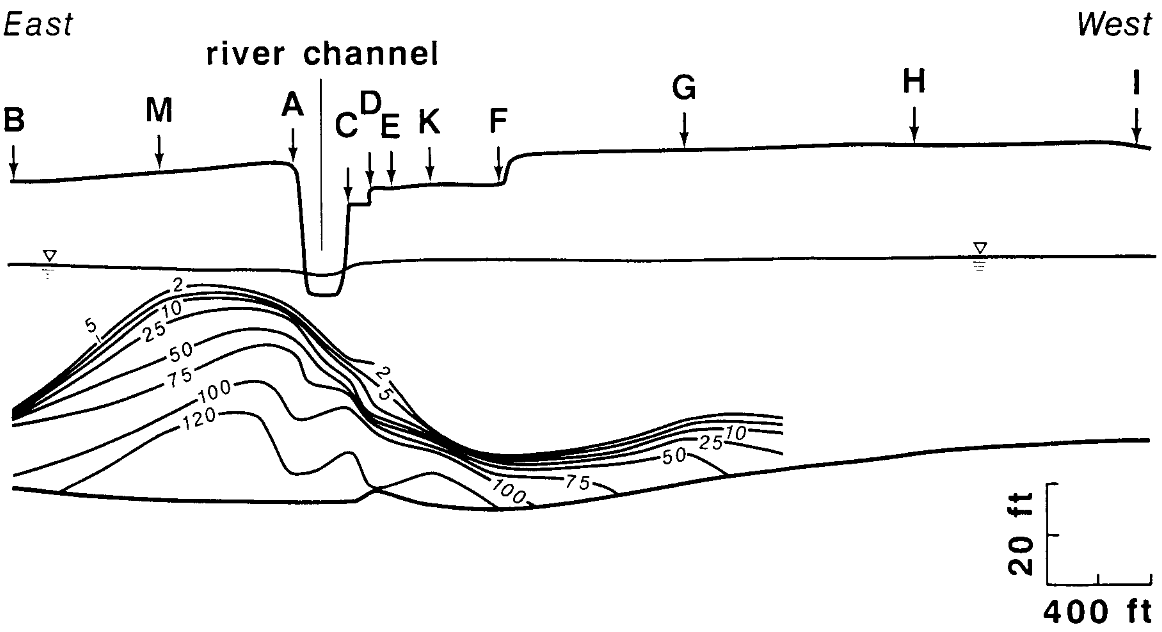

Figure 6.18 Distribution of total dissolved solids of ground-water at the field cross-section on October 30, 1985.

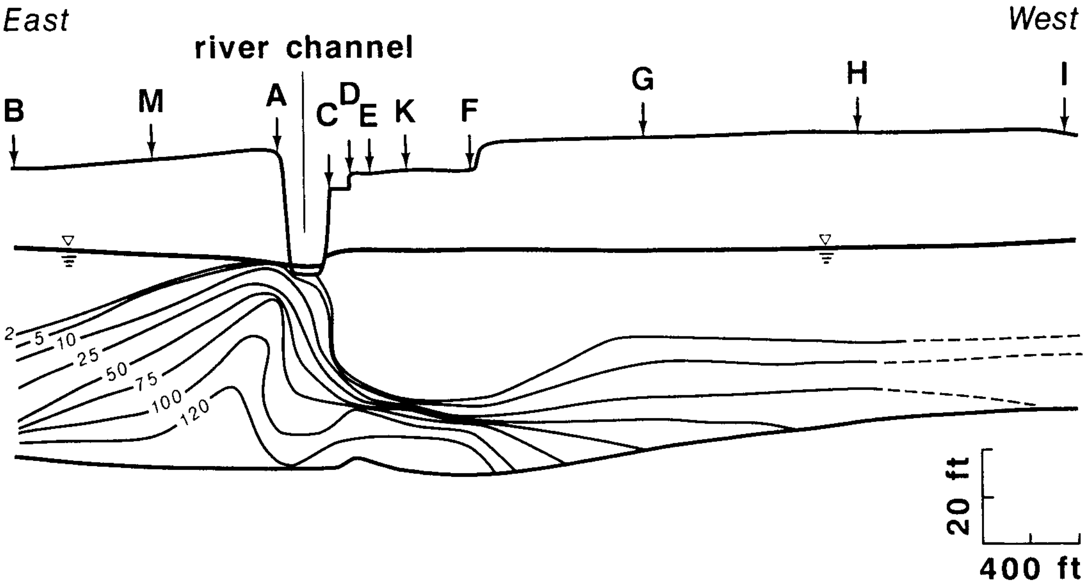

Figure 6.19 Distribution of total dissolved solids of ground-water at the field cross-section on November 27, 1985.

and November 27, 1985. Due to inaccessibility of some wells and malfunctions of the pressure transducer, only partial sets of measurements are available for October 11 and 16. Figure 6.15 illustrates the pre-flood configuration of the saltwater-intrusion zone which is associated with low streamflow conditions. The saltwater intrusion zone is in contact with the stream bottom indicating that saline ground waters are being discharged to the stream. Under similar conditions in the latter part of July 1985, water samples collected 10 feet from the west bank of the river at a depth of approximately 3.5 ft below the stream bottom contained 8340 ppm total dissolved solids.

Figure 6.16 shows a part of the saltwater intrusion area mapped from a partial set of measurements taken during the flooding at the field site on October 11, 1985. As mentioned before, a full set of measurements was not taken due to the instrument problems. The contoured map of total dissolved solids shows that the position of the intrusion area beneath monitoring sites D through F is lower than that from the previous set of measurements. The thickness of the transition zone ranges from 3 to 7 feet which is considerably less than the pre-flood thickness. Obviously, increased seepage from the stream is acting to "compress" the transition zone in the vicinity of the sites D and E. The ground-water flow direction beneath monitoring sites G, H, and I is upward and toward the west end of the cross section. The result of this upward movement of ground water in the vicinity of site G is a slight upconing of the saltwater body.

Figure 6.17 shows the shape and location of the saltwater-intrusion zone in the cross section five days after the flood occurrence. At this time, stream level and ground-water table are beginning to return to pre-flood elevations (see Figure 6.10). Also, the saltwater-intrusion area is beginning to rebound to its pre-flood configuration. Substantially more of the lower part of the alluvial aquifer is saturated with brines containing more than 100,000 ppm total dissolved solids. The thickness of the transition zone has increased beneath site D to 10 feet and the top of the transition has risen 10 feet in the alluvial aquifer since the day of the flood. East of the river the top of the transition zone is almost flat, except for a gentle rise beneath monitoring site A. The thickness of the transition zone beneath site B was approximately 23 feet during this set of measurements which is much greater than the 10-foot thickness measured prior to the flood.

Figure 6.18 shows the results of measurements made in the cross section nineteen days after the flood on October 10, 1985. By this time, the general pre-flood pattern of ground-water flow has been re-established in the cross section. The saltwater body is continuing to rebound after the flood and a definite upconing pattern is evident in the alluvial aquifer. The top of the transition zone has not yet intersected the stream bottom. The major change that has taken place in the cross section since the previous set of measurements is the redevelopment of a wide transition zone between the fresh and saline waters in the vicinity of the stream bottom. A relatively thin transition zone is present beneath monitoring sites K and F.

Figure 6.19 shows the results of the last set of measurements in the cross section made in November 27, 1985 (47 days after the flood). By this time the stream/aquifer system had returned to pre-flood conditions for the most part. The saltwater-intrusion zone has also returned to its pre-flood configuration except at site B where a relatively wide transition zone exists. A relatively thin transition zone approximately 5 feet thick is present beneath monitoring sites D through F. The top of the transition has intersected the stream bottom indicating that saline water discharge to the stream is reoccuring.

This sequence of measurements shows that the extent of the saltwater-intrusion zone is directly related to the stream stage and the elevation of the water table in the alluvial aquifer. During and after the intense period of recharge in early October, the saltwater-intrusion zone was depressed considerably below the bottom of the stream for a short period of time. However, the stream/aquifer system seems to recover quickly from these recharge events and allows the quick redevelopment of the saltwater upconing beneath the stream bottom.

These observations confirm the results obtained by Gillespie and Hargadine (1981) who showed that an increase in stream discharge caused an initial decrease in the chloride concentration of surface waters in the Smoky Hill River. However, during the streamflow recession, the chloride discharge was increased, peaked at a high level after the passage of the flood wave in the stream and then decreased with time. Similar results were demonstrated by McElwee (1985) who simulated the saltwater upconing in the cross section using a sharp-interface approximation of the transition zone between fresh and saline ground waters. McElwee (1985) used streamflow and surface-water quality data for a period of flooding that occurred in 1973-74 to analyze the transient behavior of the saltwater-intrusion system. It is interesting to note that both studies show dramatic changes taking place in the stream/aquifer system over a small period of time. McElwee (1985) assumes a 5-foot rise in stream level during the flood event. His results indicate that the time when the maximum suppression of the interface occurs was just prior to the peak discharge. Pre-flood chloride discharge levels are surpassed approximately 75 days after the onset of flooding. The maximum chloride discharge occured approximately 100 days after the onset of flooding.

McElwee's results agree quite well with the results of this investigation. In the present field investigation a return to pre-flood conditions in the stream/aquifer system was shown to occur between 21 and 49 days after flooding when stream levels rose more than 16 feet. Stream stage returned to pre-flood elevation approximately 33 days after the onset of flooding. Unfortunately, the surface waters were not sampled during the time these measurements were being made in the alluvial aquifer to observe the chloride discharge to the stream.

6.5 Major Findings from the Field Investigation

Based on our field investigation of saltwater intrusion at the Smoky Hill River site we have drawn the following conclusions:

1. Hydrogeologic framework. The sediments beneath the field site consist of a fining upward sequence of Pleistocene and Holocene alluvium ranging from coarse sand and gravel to silt and clay. The proportion of coarse sand and gravel increases eastward across the field cross section. The alluvial sediments on the west side of the river are generally more fine grained than those on the east side. The thickness of the alluvium ranges from 55 to 65 feet in the study area. The bedrock beneath the alluvium is Wellington Formation and consists of variegated gypsiferous shales and mudstones and intercalated lenses of dolomite. The total thickness of the Wellington Formation at the field site ranges from 10 to 14 feet. Beneath the Wellington Formation is the Herrington Member of the Nolans Limestone. The Herrington consists of vuggy and fractured gray gypsiferous dolomites and dolomitic shales. The total thickness of this unit was not penetrated during any of the test hole drilling at the field site. Many of the fractures and solution cavities within the Herrington are filled with gypsum.

The shallow unconfined aquifer consists of the water-saturated sediments of the alluvial valley. The total saturated thickness in the cross section ranges from 35 to 45 feet. The hydraulic conductivity of the alluvial aquifer calculated from the slug tests ranges from 18 to 403 feet/day. The values calculated from the slug tests are probably more representative of the horizontal component of hydraulic-conductivity tensor than the vertical. The geometric mean of the hydraulic-conductivity values obtained from the slug tests is 153 feet/day. The spatial distribution of the hydraulic conductivities reflects the overall geologic complexity of the alluvial sediments, especially on the west side of the river beneath sites G, H and I. The higher hydraulic conductivities are associated with coarser sediments and the lower values with the more fine-grained sediments. Experiments in the stream bottom show that the hydraulic conductivity of the sediments in the vicinity of the stream bottom is approximately 0.74 foot/day.

Beneath the alluvial aquifer is the Wellington Formation which is considered to be an aquitard. An observed range of hydraulic conductivities associated with this hydrogeologic unit is not available, but it seems that a value ranging from 1 foot/day to 10 foot/day is reasonable. Below this aquitard unit is the bedrock aquifer in the Herrington Member of the Nolans Limestone.

2. Ground-water flow and stream/aquifer interactions. Ground-water flow in the cross section is from areas of higher hydraulic head (recharge areas) to areas of lower hydraulic head (discharge areas). Recharge to the alluvial aquifer comes from infiltration through the unsaturated zone, laterally from the Smoky Hill River when the river stage reverses the hydraulic gradient in the alluvial aquifer, and vertically upward as leakage from the bedrock aquifer. Ground water is discharged to the stream in the cross section and

perpendicularly to the cross section toward the stream except for those times when stream stage is sufficiently high to reverse the hydraulic gradient in the vicinity of the stream. The slope of the water table away from the stream is generally much steeper near the west bank than the east bank. This asymmetry results because the stream at the cross section is perpendicular to the regional flow direction in the valley. West of the river, the ground-water flow pattern is distinctly affected by the heterogeneity of the sediments. Field measurements taken during the course of the field investigation show that the stream/aquifer system responds quickly to recharge events and that stream-stage fluctuations primarily affect the alluvial aquifer in the vicinity of the stream bottom. Recovery to pre-recharge event conditions occurs rather quickly but is slower in the aquifer than in the stream.

3. Morphology of the saltwater-intrusion zone in the vicinity of the field site. Ground-water total dissolved solids range from less than 1000 ppm to more than 100,000 ppm in the alluvial aquifer and generally increase with depth below the water table. The saltwater-intrusion area is asymmetrically distributed with respect to the centerline of the river channel. The saline waters located near the bottom of the alluvial aquifer are separated from the fresh-waters of the alluvial aquifer by a wide transition zone within the cross section. The transition zone is defined as the area between the 2000 ppm and 100,000 ppm dissolved solids concentration contour lines. The width of the transition zone varies spatially within the cross section and temporally in response to recharge events. Laterally, the saltwater-intrusion area intersects the cross section of monitoring sites at an acute angle. The lateral extent of the upconing seems to be controlled by the configuration of the bedrock surface and the nature of the overlying alluvial sediments above the bedrock surface. Saltwater occurs at shallow depths in the alluvial

aquifer in an area that generally follows the course of the river between monitoring sites L and B according to resistivity surveys of the study area. These results suggest that the primary source(s) of saltwater observed in the cross section comes from upgradient areas and not from within the cross section.

4. Response of the saltwater-intrusion zone to the changes in the stream/aquifer conditions. Monitoring of the saltwater-intrusion zone shows that the morphology and position of the saltwater body in the alluvial aquifer is strongly affected by changes in the stream/aquifer system. During a flood event that occurred in October 1985, the stream stage rose more than 16 feet. At this time the top of the fresh/saltwater-transition zone in the alluvial aquifer was considerably depressed below the bottom of the stream and the thickness of the zone was compressed compared to pre-flood conditions. This occurred due to higher water levels in the alluvial aquifer and higher stream stage. Then, as the stream/aquifer system returned to pre-flood conditions, the transition zone became reestablished near the bottom of the stream between 21 and 40 days after the onset of flooding. No measurements were taken during this period to determine if the top of the transition zone continued to rise to higher levels in the alluvial aquifer after the passage of the flood. These results confirm observations made by other investigators working in the area.

5. Suitability of the borehole techniques for characterizing and monitoring saltwater intrusion in a stream/aquifer system. During the course of the field investigation the fluid electrical conductivity and differential-pressure techniques were evaluated to determine their suitability for measuring variations in ground-water chemical quality in the saltwater-intrusion area. Two sets of field measurements taken using both techniques

were compared with the chemical analyses of water samples collected each time. The results from using the differential-pressure technique were more consistent with the hydrochemical data than those using the fluid electrical-conductivity logger.

7. PREVIOUS THEORETICAL DEVELOPMENTS

The contact of freshwater and saltwater is generally associated with the formation of complicated physiochemical processes, the complete description of which may not be mathematically tractable. To overcome the complexity of the problem, most investigators have regarded freshwater and saltwater as immiscible fluids separated by a sharp interface. In reality, the two fluids are miscible and can become mixed and distributed in a dispersive (transition) zone of variable salinity. A mathematical formulation based on miscibility of the fluids is more complete but is also more difficult to solve than a formulation which considers the fluids to be immiscible. The choice of which formulation to use for particular field application depends largely on the conditions along the cross section of the dispersive zone.

7.1 Immiscible-flow (Sharp-interface) Approach

In analyzing the saltwater encroachment problems, hydrologists have approximated the contact zone between freshwater and saltwater by a sharp interface for several decades. At the turn of the twentieth century, Badon-Ghyben (1888) and Herzberg (1901) independently formulated the relationship between the sea water-freshwater interface position and the ground-water regime components, assuming the steady-state condition and the Dupuit approximation. Muskat (1937) presents an analytical solution for steady and stable saltwater upconing. He assumes that the location and shape of the interface do not affect the potential distribution in the freshwater zone, which may be acceptable only when the upconed-interface location is not much different from the hydrostatic (horizontal) one. A similar solution was presented by McWhorter (1972). Bear and Dagan (1964) investigated the sea-water intrusion problem by performing a series of laboratory experiments and developed some analytical solutions for the interface motion, based on the Dupuit approximation and other simplifying assumptions with regard to the shape of the interface. Dagan and Bear (1968) presented solutions for transient-interface upconing, using the method of small perturbations. These solutions may be used to estimate the interface-motion rate only for small interface rises and cannot be used to analyze unstable upconing.

Recently Van Dam and Sikkema (1982) presented an analytical solution for the shape of the interface in a semi-confined aquifer. The solution was derived for the steady-state (flowing freshwater, stagnant saltwater) and utilizes the Dupuit approximation.

Numerical solutions of the saltwater-intrusion problem have been developed since 1971, and have used two mathematical models: 1) sharp interface - horizontal flow and 2) hydrodynamic dispersion - variable density cross sectional model. Shamir and Dagan (1971) first presented a finite-difference solution of the saltwater - freshwater flow model, which utilized the Dupuit approximation. This model has been also used by Pinder and Page (1976), who applied the Galerkin finite-element technique as a numerical approximation. Mercer et al. (1980) presented another version of the finite-difference technique used for the same model. A steady-state solution by the finite-element method was presented by Kovar (1980). Recently, Bear and Kapuler (1981) used the finite-difference technique to solve the movement of the interface in a layered coastal aquifer. Their solution also assumes the Dupuit approximation. McElwee et al. (1981) used the finite-difference technique to analyze the saltwater-upconing problem in the Smoky Hill River area near Solomon, Kansas.

7.2 Miscible-flow Approach

Cooper (1959) was among the first to explain the mixing (or the dispersion zone) and the associated perpetual circulation of sea water in coastal aquifers. According to his hypothesis, the wedge front of the saltwater flowing inland is continuously being eroded by a seaward flow of mixed water in the zone of dispersion. This flow tends to reduce the extent to which saltwater may occupy the aquifer. Field investigation of Kohout (see Cooper et al., 1964) verified Cooper's concept and confirmed the existence of the circulation phenomena along the Biscayne aquifer in the coastal region of Florida. The extent of the dispersive zone is attributed essentially to the rise and fall of the water table, ocean tides and other factors such as changes in pumping patterns.

In corroboration of Cooper's hypothesis, Henry (see Cooper et al., 1964) developed the first analytical solution of the effects of dispersion and density-dependent flow on saltwater encroachment in aquifers. Although by that time it had been discovered the magnitude of dispersion perpendicular to the velocity was much smaller than that in the direction of velocity, Henry (1964) assumed a constant-dispersion mechanism. Despite this and several other simplifying assumptions, the results of Henry's work clarified certain significant consequences of dispersion which until then had been inferred only on a qualitative basis. Henry's quantitative description of dispersion phenomena set the stage for future investigations along this line.

With the advancement in computers, a series of more rigorous solutions of sea-water intrusion problems were obtained using a variety of numerical techniques. Among these studies, we mention the work of Pinder and Cooper (1970) who used the method of characteristics in conjunction with an iterative ADI (Alternating Direction Implicit) procedure. Their approach was of practical importance in that it was applicable to heterogeneous, anisotropic aquifers with irregular geometry and different types of boundary conditions. Pinder and Cooper (1970) obtained a transient solution to the same example analyzed by Henry (see Cooper et al., 1964). Their solution was shown to approach Henry's steady-state solution after passage of a long simulation time. Reformulating the problem in terms of stream functions, Lee and Cheng (1974) derived a steady-state solution for Henry's example using finite elements. Their solution, however, encountered convergence difficulty when advective transport was predominant. This latter formulation was shown by Huyakorn and Taylor (1976) to be inferior to a formulation based on pressure (or head) and salt concentration.

All studies described above were based on the assumption of constant dispersion. In reality, as pointed out before, the dispersion mechanism is dependent upon the fluid velocity and the characteristics of the porous materials. For sea-water intrusion in a coastal aquifer where sea water and freshwater flow in opposite directions, a zone of low fluid velocity develops at the contact of the two fields near the bottom of aquifer. Because the only dispersion process in the absence of fluid motion is molecular diffusion, the use of velocity-dependent dispersion parameters appear to be essential in such situations.

Segol et al. (1975) and Segol and Pinder (1976) were the first to develop a transient solution of the saltwater-encroachment problem on the basis of velocity-dependent dispersion coefficients. Using the mixed finite-element formulation of ground-water flow and Darcy velocity equations, they obtained accurate estimates of velocity components while preserving continuity of the velocity across elemental boundaries. In advection-dominated transport problems, such a formulation is essential to achieving realistic solutions. A disadvantage associated with this approach is the need of solving a very large system of equations which increases the computational cost. For large aquifers requiring a long-term transient response, this disadvantage can limit the practical applicability of the mixed formulation.

With emphasis on optimum efficiency, Frind (1982a) has developed a finite-element model for simulation of saltwater intrusion that was found to be much less costly than comparable existing models. Two distinctive features of Frind's model are the elimination of static pressures in the fluid-flow equation, achieved by introduction of equivalent freshwater head, and the elimination of numerical integrations over elements, achieved by the deliberate choice of linear rectangular elements. This approach does not retain the continuity of the velocity field at the element boundaries. The solution obtained by this model was shown to approach that obtained with a continuous velocity as the grid size was refined. Frind (1982b) demonstrated that his model was capable of handling large simulation periods in aquifer systems of practical importance.

Over the past years, relatively little attention has been given to the analysis of layered aquifers in which the aquifer is divided into several strata by interlying semipervious or impervious layers. For such aquifers, the permeability contrast between different layers usually results in the development of multiple saltwater wedges. The modeling of a complex multiaquifer system may be achieved simply by approximating the entire aquifer by a suitable saltwater-intrusion model (Kawatani, 1980). Solution procedures may, however, encounter difficulty if substantial permeability contrast exists between the system components. Frind (1982b) has reported several numerical advantages if flow in a semipervious layer or aquitard is assumed to be essentially vertical. This assumption is justified on the basis of two-order-of-magnitude permeability contrasts between the layers (Neuman and Witherspoon, 1969). Frind's simulations show that hydrologic characteristics of the aquitard in continuous coastal aquifer-aquitard systems have a great controlling influence on flow dynamics of the entire system.

7.3 Summary

As indicated above, a variety of mathematical models are available for description of saltwater/freshwater systems. The specific conditions of the problem being analyzed determine the selection of an appropriate model. If the flow domain and boundary conditions are relatively simple and the aquifer has homogeneous characteristics, an analytical solution such as the one developed by Henry (see Cooper et al., 1964) may well be sufficient. However, because of the hydrogeologic complexity involved, the majority of aquifer problems of practical interest necessitate the use of a sophisticated numerical model. Two computer models that are currently available for this use are those by INTERA (1976) and U.S. Geological Survey (Voss, 1984). Both of these models are based on the solution of the advection-dispersion equation for variable-density flow conditions. The solution procedures used in these models may encounter numerical oscillation and numerical dispersion if the advective transport is predominant. These difficulties are indirectly related to the poorly defined transport theory in a complex hydrogeologic environment.

In summary, considerable progress has been achieved in the last two decades in understanding the advection and dispersion of salt at the contact of saltwater and freshwater. Although most of the literature in this regard has been concerned with coastal aquifers in contact with sea-water, the basic principles and theory developed apply to inland aquifers as well. Along with increased understanding of physical processes, mathematical models have been developed to test the theory against field observations. The results of such analysis have brought to light many of the relationships and factors that control the mechanisms of saltwater intrusion. As yet, more is left to be discovered before our understanding of the processes involved is complete.

8. AN IMPLICIT BOUNDARY-ELEMENT SOLUTION TO SALTWATER UPCONING

A new implicit approximation of the interface-motion equation is combined with the boundary-element method (BEM) in order to solve the interface-upconing problem. The performance of the implicit scheme is tested by means of numerical simulation. In order to verify the solution, the numerical results for the problem of saltwater upconing under a drain are compared with experimental data (Dagan and Bear, 1968).

8.1 Mathematical Statement of the Problem

We are considering flow of two fluids in a confined homogeneous aquifer, assuming that a sharp interface separates them, such that each fluid occupies a separate zone (Fig. 8.1). The shapes of these zones may vary with time because of the interface motion. Assuming that the fluids and porous medium are incompressible, we can write for each zone a continuity equation as follows (Bear, 1979):

$$\nabla^2\phi^F = 0 \tag{8.1}$$

$$\nabla^2\phi^S = 0 \tag{8.2}$$

where $\phi^F = z + p/\gamma_F$ is freshwater potential, and $\phi^S = z + p/\gamma_S$ is saltwater potential.

In order to be able to solve the system of partial-differential equations (eqs. 8.1 and 8.2), boundary and initial conditions for each zone have to be specified. Boundary conditions on the boundaries excluding the interface are of the same kind as for the flow of a single fluid, i.e. either of the

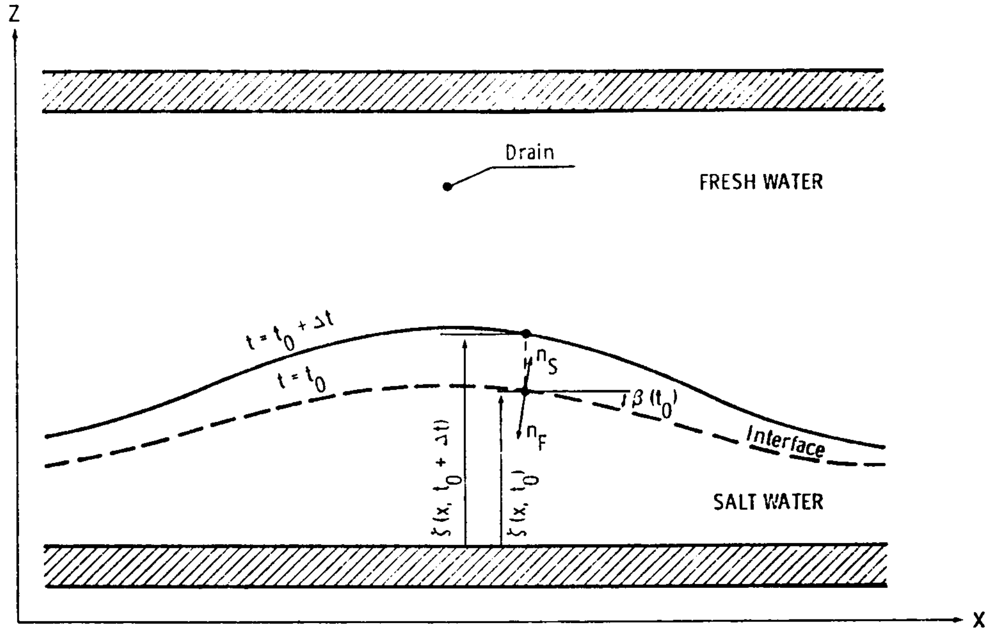

Figure 8.1 Saltwater/freshwater interface-motion scheme.

Dirichlet (given potential ϕ) or Neumann (given normal derivative $\partial\phi/\partial n$) type.

The interface-boundary conditions require the continuity of the pressure and the continuity of the fluxes normal to the interface and may be written as (Bear, 1979)

$$\phi^S = \frac{\gamma_F}{\gamma_S}\phi^F + \frac{\gamma_S - \gamma_F}{\gamma_S}\zeta \qquad (8.3)$$

$$\frac{\partial\phi^S}{\partial n_S} = -\frac{K_F}{K_S}\frac{\partial\phi^F}{\partial n_F} \qquad (8.4)$$

The initial conditions are given by the initial location of the interface $\zeta(x,t_o)$.

The solution of equations 8.1 and 8.2, subject to the boundary conditions and interface relationships, gives, in the transient case, nonzero normal fluxes along the interface. These fluxes cause interface movement. The interface-motion equation may be written as (Bear, 1979)

$$F(x,z,t) = 0 \qquad (8.5)$$

The interface is a material surface (i.e. the fluid particles which, once on the interface, will remain on it unless they leave the system). Therefore, the material derivative of the interface equation is equal to zero (Bear, 1979):

$$\frac{DF}{Dt} = \frac{\partial F}{\partial t} + v \quad \nabla F = 0 \qquad (8.6)$$

where v is particle velocity on the interface. Since in this study we are interested in the vertical motion of the interface, we express the interface equation as

$$F = \zeta(x,t) - z = 0 \qquad (8.7)$$

The dot-product in equation 8.6 may be expressed by

$$v \quad \nabla F = \nabla F \ \ (\text{projection of } v \text{ on } \nabla F) = \nabla F \ \ (v_{n_F}) \qquad (8.8)$$

where v_{n_F} is particle velocity normal to interface,

$$v_{n_F} = - \frac{K_F}{S_o} \frac{\partial \phi^F}{\partial n_F} \qquad (8.9)$$

where S_o is specific porosity. Substituting equations 8.7, 8.8 and 8.9 into equation 8.6, we obtain

$$\frac{\partial \zeta}{\partial t} - \left(1 + \left(\frac{\partial \zeta}{\partial x}\right)^2\right)^{1/2} \frac{K_F}{S_o} \frac{\partial \phi^F}{\partial n_F} = 0 \qquad (8.10)$$

Substituting $\tan\beta$ for $\frac{\partial \zeta}{\partial x}$ (see Fig. 8.1), we finally obtain the kinematic equation of the interface motion

$$\frac{\partial \zeta}{\partial t} = \frac{K_F}{S_o} \left(1 + (\tan\beta)^2\right)^{1/2} \frac{\partial \phi^F}{\partial n_F} = \frac{K_F}{S_o \cos\beta} \frac{\partial \phi^F}{\partial n_F} \qquad (8.11)$$

8.2 Numerical Formulation

The numerical procedure presented herein simulates the interface motion as a sequence of quasi-steady states (Bear, 1979). In each quasi-steady state the equations of flow (equations 8.1 and 8.2), subject to the boundary and initial conditions, are solved. In order to solve the flow equations, the BEM was used. A detailed description of the method, as applied to ground-water flow, may be found in Liggett and Liu (1983).

Application of the BEM to the flow equations leads to a system of N equations given by

$$\sum_{j=1}^{M} \left[\left(\int_{\Gamma_F} \frac{1}{r_i}\frac{\partial r_i}{\partial n_F} N_j \, dS\right) \phi_j^F\right] = \sum_{j=1}^{M} \left[\left(\int_{\Gamma_F} \ln r_i N_j dS\right) \frac{\partial \phi_j^F}{\partial n_F}\right] \qquad (8.12)$$

$$i = 1,2,\ldots.,M$$

$$\sum_{j=M+1}^{N} \left[\left(\int_{\Gamma_S} \frac{1}{r_i}\frac{\partial r_i}{\partial n_S} N_j \, dS\right) \phi_j^S\right] = \sum_{j=M+1}^{N} \left[\left(\int_{\Gamma_S} \ln r_j N_j dS\right) \frac{\partial \phi_j^S}{\partial n_S}\right] \qquad (8.13)$$

$$i = M+1,\ M+2,\ldots.,N$$

where

$N_j(x,z)$ = basis function of node j: this solution utilizes linear basis function; see Liggett and Liu (1983)

ϕ_j = value of potential ϕ at node j

$(\frac{\partial \phi}{\partial n})_j$ = value of normal derivative of potential ϕ at node j

r_i = distance from node i on the boundary to another point on boundary

Γ_F = boundary of freshwater zone

Γ_S = boundary of saltwater zone

M = number of nodes in freshwater zone

N = total number of nodes.

Note that the number of nodes at the saltwater zone is equal to N-M and that the nodes on the interface are numbered twice, once in the freshwater zone and once in the saltwater zone (Figure 8.2).

The system of N equations given by equations 8.12 and 8.13 has 2N unknowns (namely ϕ and $\partial\phi/\partial n$ at each node). However, with the exception of the interface, a value of either ϕ or $\partial\phi/\partial n$ is known at each node from the boundary conditions, thus providing additional N-2I equations, where I is the number of the interface nodes at each zone. The remaining 2I equations are provided by the interface relationships for each couple of nodes on the interface (Figure 8.2),

$$(\phi^F)^k = \frac{\gamma_S}{\gamma_F}(\phi^S)^k - \frac{\gamma_S - \gamma_F}{\gamma_F}\zeta^k \tag{8.14}$$

$$\left(\frac{\partial\phi^F}{\partial n_F}\right) = -\frac{K_S}{K_F}\left(\frac{\partial\phi^S}{\partial n_S}\right)^k \tag{8.15}$$

After the BEM equations for freshwater and saltwater zones are solved, resulting in the distribution of the potential ϕ and its normal derivative $\partial\phi/\partial n$ along the boundaries, a new location of the interface nodes may be calculated using equation 8.11. Approximating equation 8.11 with the explicit finite-difference scheme gives

$$\zeta^{k+1} = \zeta^k + \frac{K_F\,\Delta t}{S_o\cos(\beta^k)}\left(\frac{\partial\phi^F}{\partial n_F}\right)^k \tag{8.16}$$

However, the explicit scheme may cause instability of the numerical solution. Thus, being able to predict the normal fluxes along the interface for the next time step k+1 and to approximate the interface-motion equation using an implicit scheme similar to the one used by Liggett (1977) for the free-

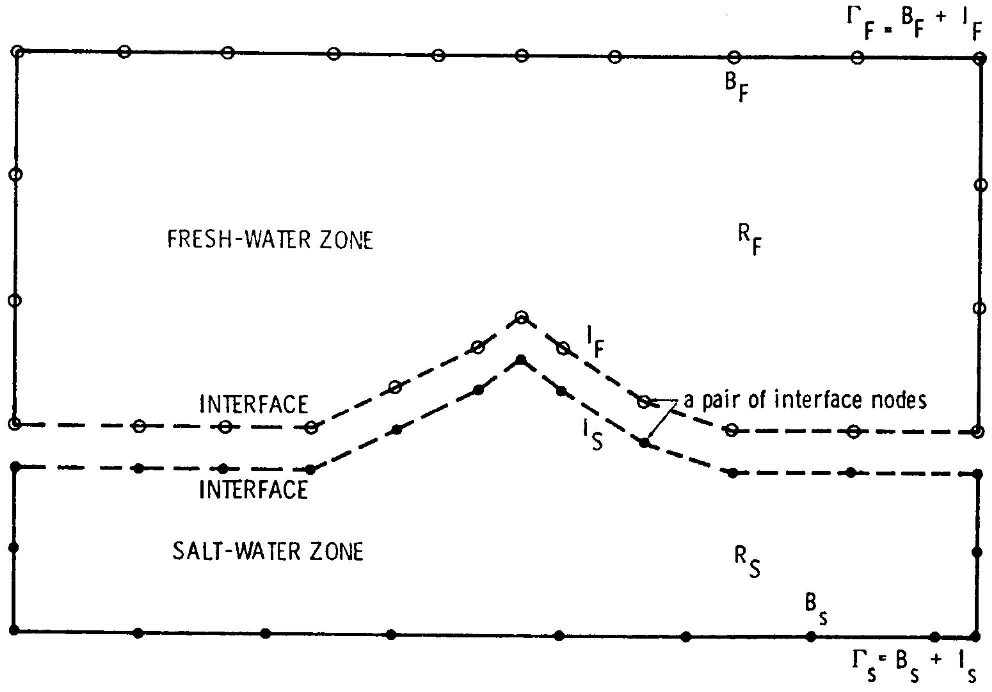

Figure 8.2 Discretized region for the numerical solution.

surface motion would be desirable. The derivation of the implicit interface relationships is presented below. Approximating equation 8.11 with the implicit finite-difference scheme gives (Liggett, 1977)

$$\zeta^{k+1} = \zeta^{k} + \frac{K_F \, \Delta t}{S_o \cos(\beta_i^k)} \{\omega (\frac{\partial \phi^F}{\partial n_F})^{k+1} + (1-\omega) \; (\frac{\partial \phi^F}{\partial n_F})^{k} \} \qquad (8.17)$$

After writing equation 8.3 for times k and k+1 and subtracting the former from the latter, we obtain

$$(\phi^F)^{k+1} - (\phi^F)^{k} = \frac{\gamma_S}{\gamma_F} \{ (\phi^S)^{k+1} - (\phi^S)^{k} \} - \frac{\gamma_S - \gamma_F}{\gamma_F} (\zeta^{k+1} - \zeta^{k}) \qquad (8.18)$$

Substituting equation 8.17 into equation 8.18 we obtain

$$(\phi^F)^{k+1} - (\phi^F)^{k} - \frac{\gamma_S}{\gamma_F} (\phi^S)^{k} - \frac{\gamma_S - \gamma_F}{\gamma_F} \, \frac{K_F \, \Delta t}{S_o \cos(\beta^k)} (1-\omega) \; (\frac{\partial \phi^F}{\partial n_F})^{k}$$

$$+ \frac{\gamma_S}{\gamma_F} (\phi^S)^{k+1} - \frac{\gamma_S - \gamma_F}{\gamma_F} \, \frac{K_F \, \Delta t}{S_o \cos(\beta^k)} \, \omega (\frac{\partial \phi^F}{\partial n_F})^{k+1} \qquad (8.19)$$

Equation 8.19 and the continuity of flow equation given by

$$(\frac{\partial \phi^F}{\partial n_F})^{k+1} = - \frac{K_S}{K_F} (\frac{\partial \phi^S}{\partial n_S})^{k+1} \qquad (8.20)$$

provide the set of implicit equations for the interface motion.

Using the implicit scheme the numerical procedure for each time step (k) consists of

1) Solving equations 8.1 and 8.2 (approximated by equations 8.12 and 8.13) subject to boundary and initial conditions and interface relationships

(equations 8.14 and 8.15). As a result we obtain the values of the potentials $(\phi^F)^k$ and $(\phi^S)^k$ and their normal derivatives $(\partial\phi^F/\partial n_F)^k$ and $(\partial\phi^S/\partial n_S)^k$.

2) Solving equations 8.1 and 8.2 subject to the boundary and initial conditions and the interface relationships given by equations 8.19 and 8.20. As a result we obtain the predicted values of $(\phi^F)^{k+1}$ and $(\phi^S)^{k+1}$ and their normal derivatives.

3) Calculating a new location of the interface using equation 8.17.

Note that in the numerical program, the boundary conditions and interface relationships are incorporated into the system of BEM equations during its formation; therefore, the actual number of unknowns is equal to N.

8.3 Numerical Results

In order to test the performance of the implicit solution and to verify the numerical model, numerical simulations were run for the conditions used in the laboratory experiment of Dagan and Bear (1968). In this experiment the initial interface was in a steady-hydrostatic state (Figure 8.3). At t=0 the drain, located in the freshwater zone, started withdrawing water with a constant rate Q. The boundary conditions, geometry, and numerical discretization, for which some 80 nodes were used, are given in Figure 8.3. The hydraulic parameters for the numerical simulation are given in Table 1.

In order to avoid numerical modeling of the drain singularity, we used the superposition method (Liggett and Liu, 1983). The general solution in the freshwater zone was expressed as a sum of the numerical solution ϕ_1^F and the singular solution for a drain ϕ_2^F

$$\phi^F = \phi_1^F + \phi_2^F \tag{8.21}$$

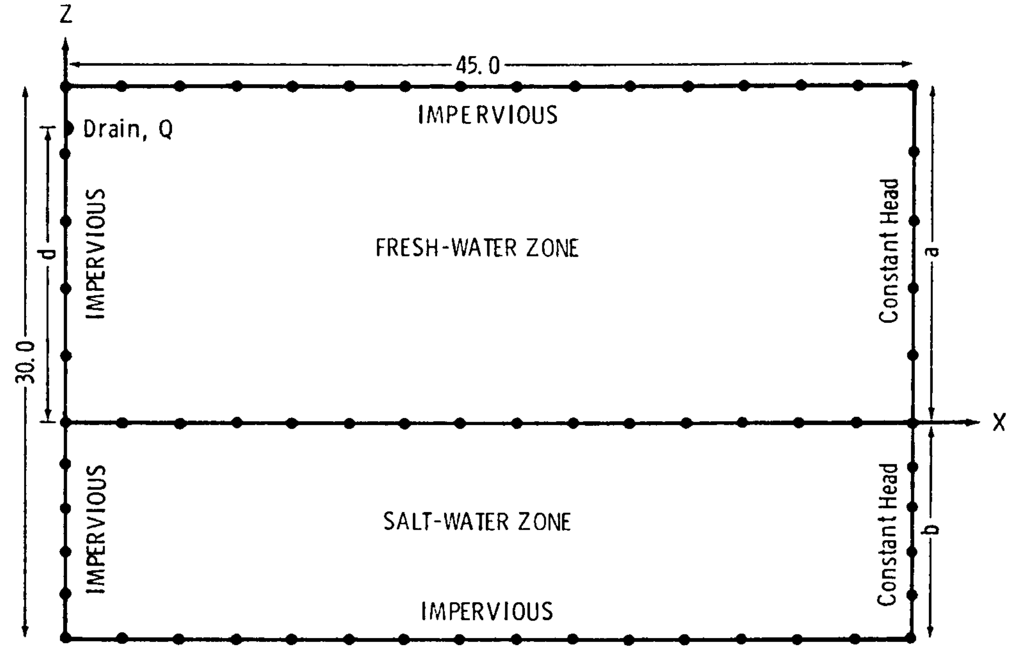

Figure 8.3 Numerical discretization for the salt-water-upconing experiment by Dagan and Bear (1968; dimensions in cm).

where,

$$\phi_2^F = \frac{Q}{2\pi K_F} \ell n r_o \tag{8.22}$$

The boundary conditions for the numerical solution in the freshwater zone were calculated using equations

$$\phi_1^F = \phi^F - \frac{Q}{2\pi K_F} \ln r_o \tag{8.23}$$

$$\frac{\partial \phi_1^F}{\partial n_F} = \frac{\partial \phi^F}{\partial n_F} - \frac{Q}{2\pi K_F r_o} \frac{\partial r_o}{\partial n_F} \tag{8.24}$$

Equations 8.23 and 8.24 also were used to rearrange the interface relationships (equations 8.14, 8.15, 8.19 and 8.20).

The comparison of the boundary-element results with the experimental results obtained by Bear and Dagan (1964) for two pumpage rates (experiments A5 and A7, $Q_{A5} = 1.23$ cm^3/sec/cm and $Q_{A7} = 0.66$ cm^3/sec/cm) is presented in Figures 8.4 and 8.5. The numerical results are in close agreement with the experimental ones, thus verifying the numerical model.

In order to test the accuracy and stability of the numerical solution, numerical experiments for various pumping rates Q, time steps Δt, weighting factors ω, and node spacing were simulated. The results of these simulations are presented in Figures 8.6, 8.7, and 8.8. These results were obtained for $Q = .02\,\pi K_F$, $.04\pi K_F$, and $.06\pi K_F$, respectively, and show stable saltwater upconing, i.e. the saltwater/freshwater interface reaches the steady-state location below the drain. In Figure 8.6B the results obtained by the explicit scheme are presented for comparison.

Analysis of these results shows that the implicit scheme for the interface motion presented herein gives good results, even for relatively long time

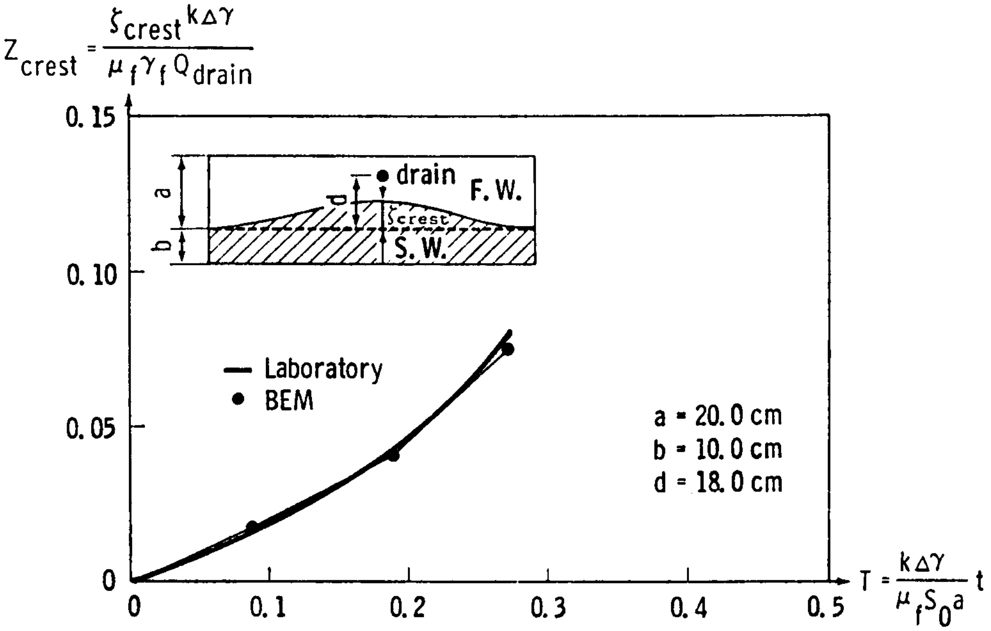

Figure 8.4 The rise of the interface as a function of time, Q = 1.23 cm^3/sec/cm.

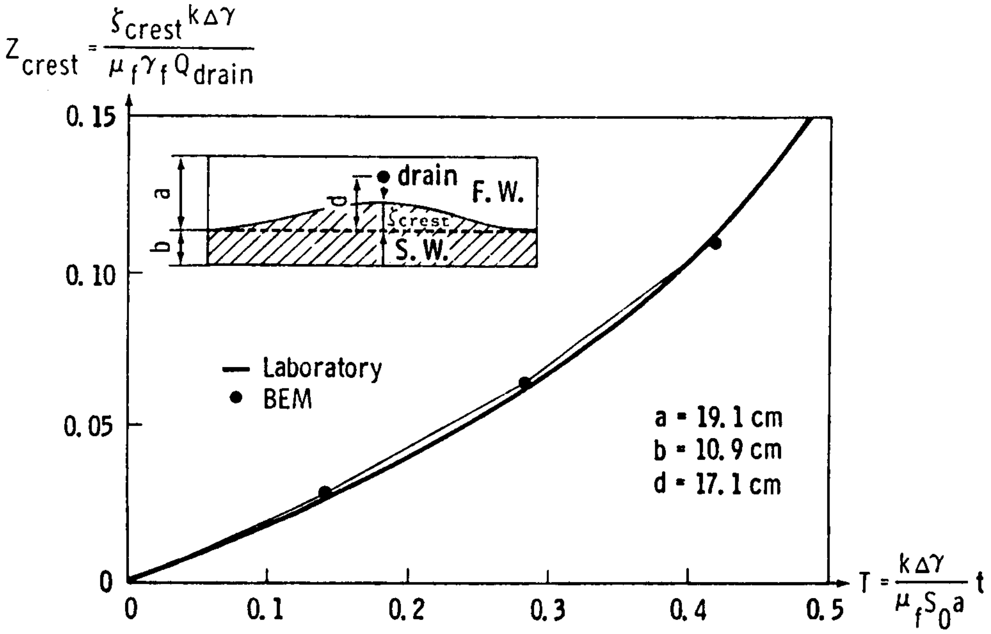

Figure 8.5 The rise of the interface as a function of time, Q = 0.66 cm^3/sec/cm.

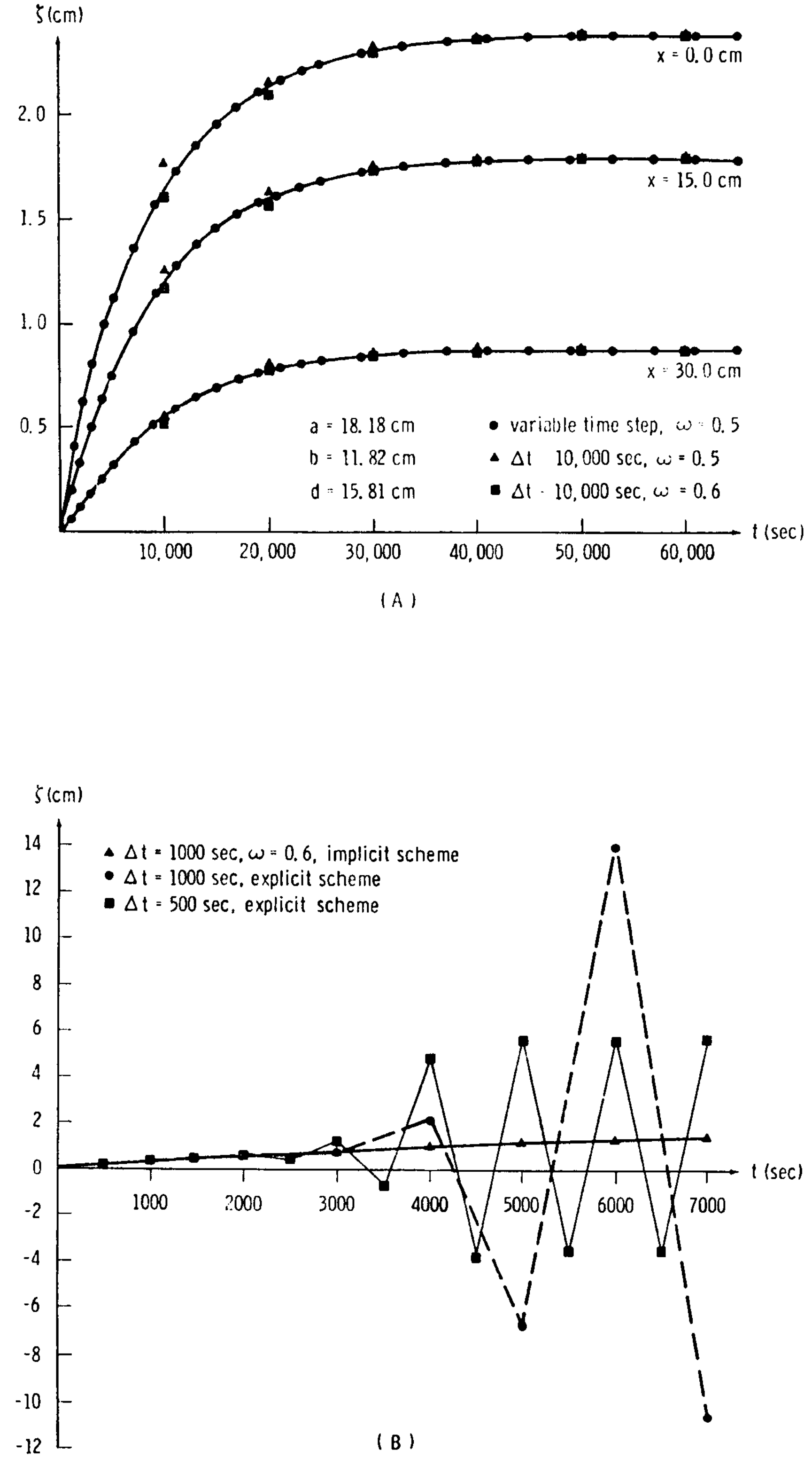

Figure 8.6 The rise of the interface as a function of time, $Q = .02\pi K_F$; a) implicit scheme, and b) implicit and explicit schemes.

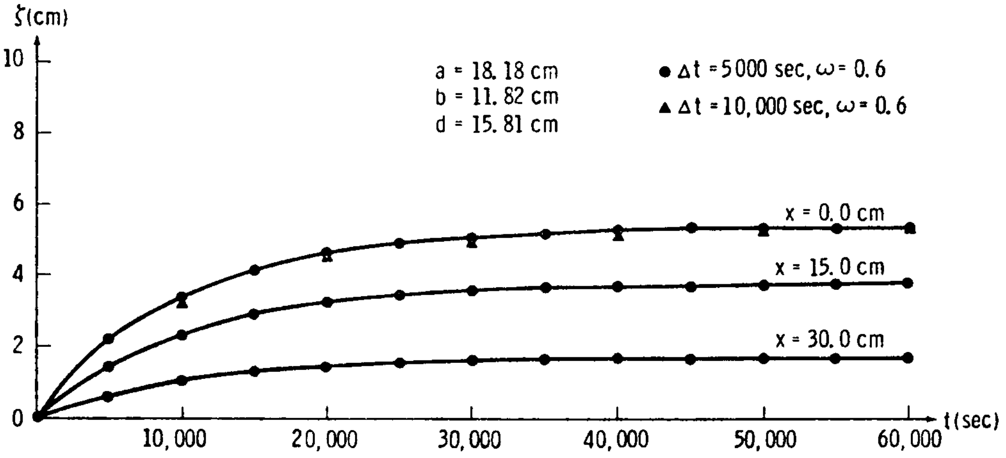

Figure 8.7 The rise of the interface as a function of time, $Q = .04\pi K_F$.

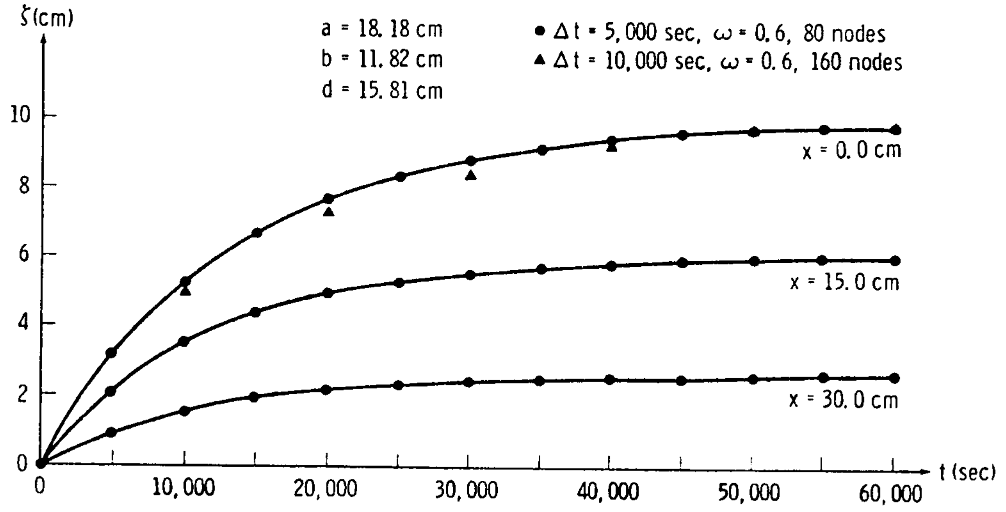

Figure 8.8 The rise of the interface as a function of time, $Q = .06\pi K_F$.

steps, for which the explicit scheme results in an unstable numerical solution (Figure 8.6B). A stable numerical solution for $Q = .02\pi K_F$ for the explicit scheme was obtained for $\Delta t = 200$ sec (for $\Delta t = 500$, the solution was unstable; Figure 8.6B), whereas the implicit scheme gives a stable solution for $\Delta t = 10{,}000$ sec (Figure 8.6A). The numerical model does not seem to be very sensitive to the node spacing (Figure 8.8).

The steady-state locations of the interface for the three pumpage rates are depicted in Figure 8.9. In Figure 8.10 we present the numerical results for two pumpage rates ($Q = .08\pi K_F$, $Q = .1\pi K_F$) that caused unstable upconing, i.e. the flow of saltwater into the drain.

8.4 Summary and Conclusions

The boundary-element method was developed and modified for solving saltwater-intrusion problems, assuming a sharp interface between freshwater and saltwater zones. The solution does not use the Dupuit approximation, thus providing a better model for the cases in which the vertical component of the flow is significant. For the simulation of the interface motion, a special implicit scheme was developed, which gives substantially better results than the explicit solution. The numerical model may be used to analyze steady and unsteady, stable and unstable, saltwater-upconing problems.

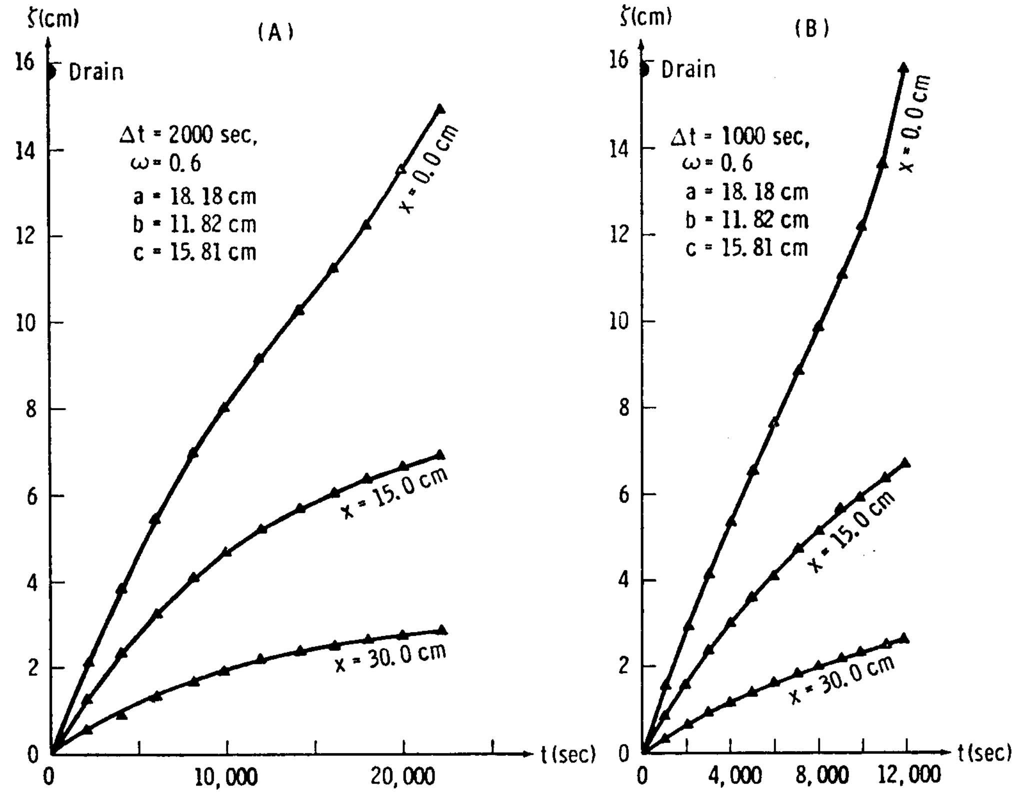

Figure 8.9 The rise of the interface as a function of time, A) $Q = .08\pi K_F$; B) $Q = .1\pi K_F$.

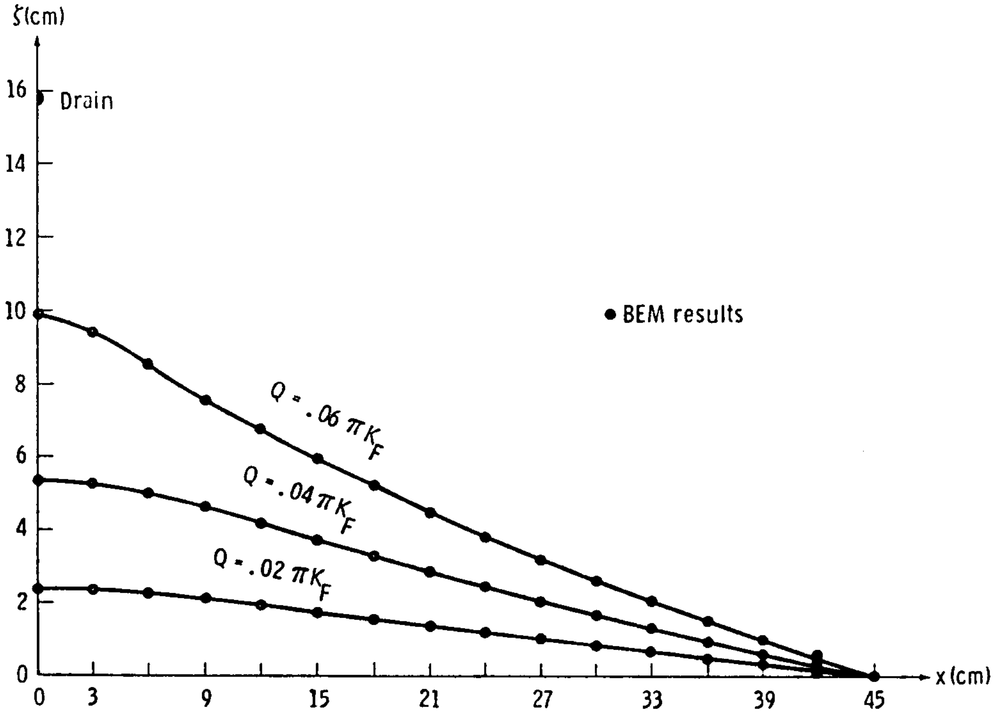

Figure 8.10 The shapes of the steady-state interfaces.

9. THE IMPACT OF THE DUPUIT-FORCHHEIMER APPROXIMATION ON SALTWATER-INTRUSION SIMULATION

The Dupuit approximation has been used extensively in the numerical analysis of saltwater upconing. It is important to establish under what circumstances the use of the Dupuit-Forchheimer approximation is acceptable and how the errors related to its use may be corrected. This analysis is performed by means of numerical simulation of two problems: 1) upconing under a sink of small size (drain), compared to the thickness of the freshwater zone, and 2) upconing under a river whose depth is of the same order as that of the freshwater zone.

9.1 Mathematical Formulation of the Problem Based on Dupuit-Forchheimer Approximation

In the previous section, we described the formulation of a sharp interface model which did not use the Dupuit-Forchheimer approximation. This description may be substantially simplified by assuming validity of the Dupuit-Forchheimer approximation. In this case the freshwater zone and saltwater zone continuity equations may be written for a confined aquifer as (Figure 9.1)

$$\frac{\partial}{\partial x}\left(K_F(b-\zeta)\frac{\partial \phi^F}{\partial x}\right) + S_o\frac{\partial \zeta}{\partial t} = Q \qquad (9.1)$$

$$\frac{\partial}{\partial x}\left(K_S(\zeta-d)\frac{\partial \phi^S}{\partial x}\right) + \frac{K_o}{b_o}(\phi_o^S - \phi^S) = S_o\frac{\partial \zeta}{\partial t} \qquad (9.2)$$

where K_o is the hydraulic conductivity of the semi-confining layer, Q is the unit withdrawal, and ϕ_o^S is the constant potential in the saltwater aquifer beneath the semi-confining layer. Equations 10.1 and 10.2 form a system of

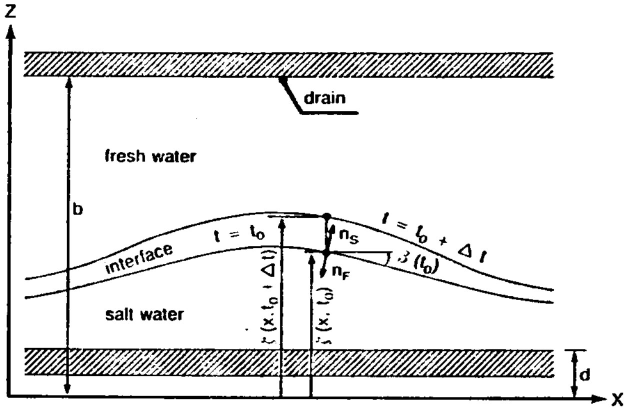

Figure 9.1 Scheme of saltwater upconing.

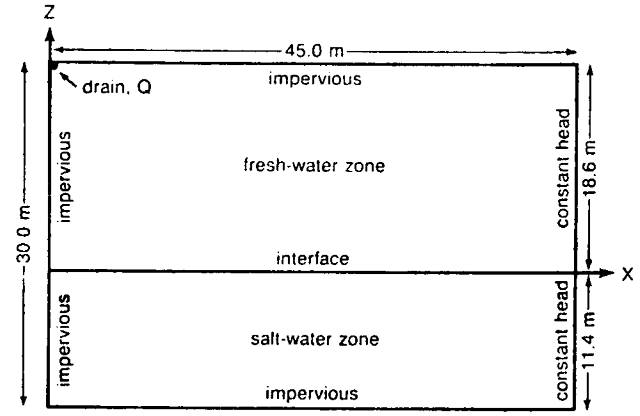

Figure 9.2 Scheme of hypothetical model.

coupled partial-differential equations with three dependent variables, namely ϕ^F, ζ, and ϕ^S. In order to eliminate one of them, e.g., ϕ^S, we use the interface relationship given by equation 8.3.

For an unconfined aquifer the continuity equation for the freshwater zone may be written as

$$\frac{\partial}{\partial x}\left(K_F\,(\phi^F-\zeta)\,\frac{\partial\phi^F}{\partial x}\right) = S_o\left(\frac{\partial\phi^F}{\partial t} - \frac{\partial\zeta}{\partial t}\right) + Q \tag{9.3}$$

Equations 9.1, 9.2, and 9.3 may be approximated using the finite-difference method for the spatial derivatives and the implicit finite-difference scheme for the time derivative. Application of this approximation to equation 9.3 leads to

$$\begin{aligned}
&(1-w)\,[Y^k_{J,J-1}\,\{(\phi^F_{J-1})^k - (\phi^F_J)^k\} + Y^k_{J,J+1}\,\{(\phi^F_{J+1})^k - (\phi^F_J)^k\}] \\
&\quad + w[Y^{k+1}_{J,J-1}\{(\phi^F_{J-1})^{k+1} - (\phi^F_J)^{k+1}\} + Y^{k+1}_{J,J+1} \\
&\qquad \{(\phi^F_{J+1})^{k+1} - (\phi^F_J)^{k+1}\}] \\
&\quad = \frac{s_o\Delta x}{\Delta t}\,[\{(\phi^F_J)^{k+1} - (\phi^F_J)^k\} - \{(\zeta_J)^{k+1} - (\zeta_J)^k\}] + Q_J
\end{aligned} \tag{9.4}$$

where $Y_{J,J-1}$ is the transmissibility of connection between nodes J and J-1 (Figure 9.3).

$$Y^K_{J,J-1} = \frac{\{(\phi^F_J)^k + (\phi^F_{J-1})^k - (\zeta_J)^k - (\zeta_{J-1})^k\}\;K_F}{2\Delta x} \tag{9.5}$$

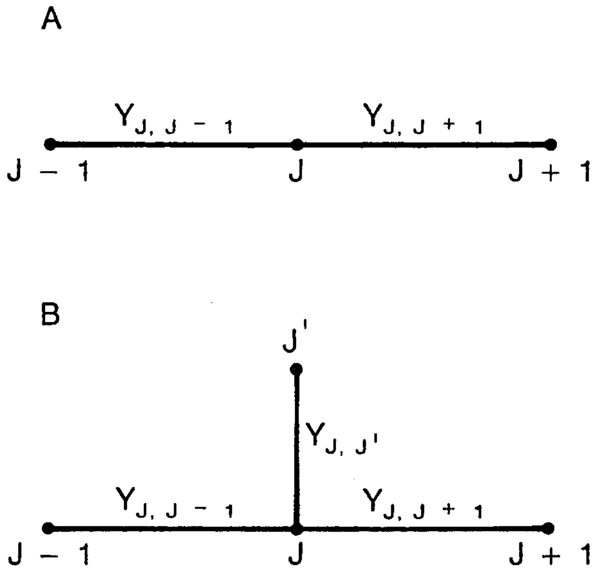

Figure 9.3 Numerical network in freshwater zone; A) without correction for partial penetration, B) with correction.

where,

w = weighting factor

k = time-step index

Δx = spatial step

Δt = time step

J = index of finite-difference node.

The finite-difference approximation of equations 9.1 and 9.2 leads to expressions similar to equation 9.4.

After formulating the finite-difference equation for each node in the freshwater and saltwater zone, we obtain a system of quasilinear equations. The Gauss-Seidel method was used in this paper to solve the resulting system of equations. The solution for each time step gives spatial and temporal distribution of ϕ^F and ζ (ϕ^S may be calculated from equation 9.3).

9.2 Upconing Under a Drain

The hydrogeologic situation of this problem is depicted in Figure 9.2. A semicircular drain ($r_0 = 0.5$ m) is located at the top of a confined aquifer occupied by fresh ($\gamma_F = 1.00$) and salt ($\gamma_S = 1.03$) waters. Because of the symmetry of the problem we consider only half of the region. The hydraulic conductivities are $K_F = 100$ meters/day and $K_S = 103$ meters/day. The boundary conditions of the problem are depicted in Figure 9.2; the potentials ϕ^F and ϕ^S on the right-hand side are equal to zero, and the potential at the drain, ϕ^F_D, was varied from one experiment to another.

The steady-state locations of the interface obtained by the "non-Dupuit" and "Dupuit" models for two different values of the potential at the drain ($\phi^F_D = -.175$ m and $\phi^F_D = -.36$ m) are shown in Figures 9.4 and 9.5. Clearly, the results obtained by the two models are quite different. This difference is caused by the potential loss between the interface and the sink, which is

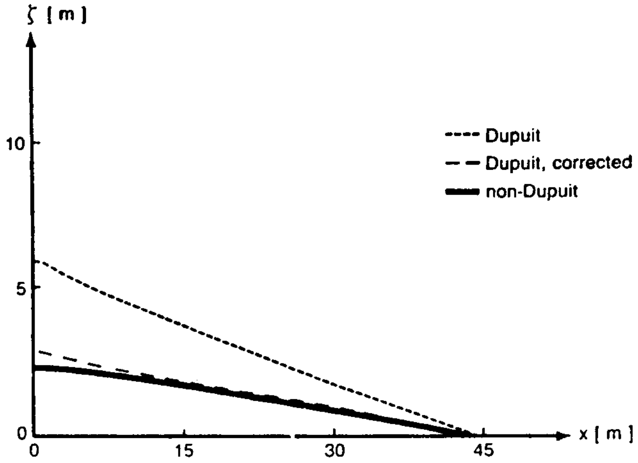

Figure 9.4 Location of steady-state interface, ϕ_D = -.175 m.

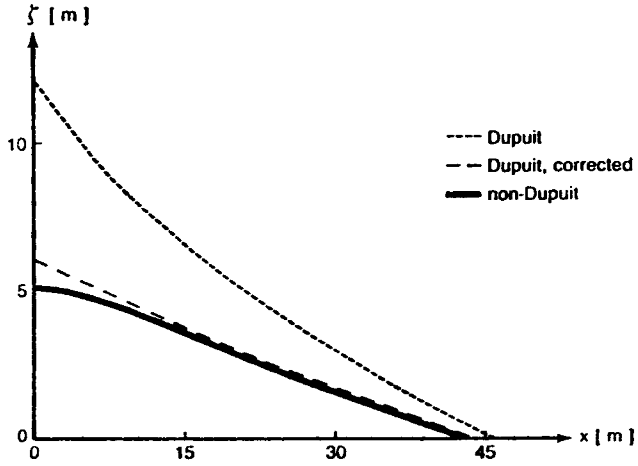

Figure 9.5 Location of steady-state interface, ϕ_D = -.36 m.

due to the partial penetration of the sink and is not accounted for by the "Dupuit" model. According to this model the interface elevation under the drain is given by (Bear, 1979)

$$\zeta_1 = \frac{-\gamma_F}{\gamma_S - \gamma_F} \phi_D^F \tag{9.6}$$

whereas the "non-Dupuit" model gives

$$\zeta_2 = \frac{-\gamma_F}{\gamma_S - \gamma_F} (\phi_D^F - \Delta\phi^F) \tag{9.7}$$

where $\Delta\phi^F$ is the additional potential loss between the interface and the drain. Notice that in this case, both ϕ_D^F and $\Delta\phi^F$ are negative, and therefore $\zeta_2 < \zeta_1$ (Figures 9.4 and 9.5). In addition to the error in estimating the location of the interface, the "Dupuit" model gives erroneous results with regard to the drain's withdrawal rate Q_o. This rate for the first case ($\phi_D^F = -.175$) was calculated to be $Q_o = 6.3$ m$^{\text{eters}2}$/day from the "non-Dupuit" model and $Q_o = 12.2$ m$^{\text{eters}2}$/day from the other model.

In order to correct this discrepancy, we use an analytic solution for calculating the additional potential loss due to the partial penetration. For this particular geometry, the analytic solution is given by (Huisman, 1972)

$$\Delta\phi^F = \frac{Q_o}{\pi K_F} \ln \left(\frac{b-\zeta}{\pi r_o}\right) \tag{9.8}$$

where r_o is the drain radius. Simulation of $\Delta\phi^F$ is provided by adding an extra node (J*) to the drain node (J; Figure 9.3). The transmissibility of the connection between node J and J*, which represents the ratio of the flow through the connection (Q_o) to the difference of potential between the two nodes, may be obtained

$$Y_{J,J*} = \frac{Q_o}{\Delta\phi^F} = \pi K_F\{\ell n(\frac{b-\zeta}{\pi r_o})\}^{-1} . \qquad (9.9)$$

The contribution of this connection may be easily added to equation 9.4 written for the "drain node." Notice that the boundary condition ϕ_D^F is now given at the additional node.

The results obtained by this correction method are presented in Figures 9.4, 9.5, and 9.6 and are in good agreement with the ones obtained by the "non-Dupuit" model. A small difference between the results just under the drain may be explained by the fact that the correction method assumes that the total difference of potential between the interface and the drain is due only to the partial penetration $(\Delta\phi^F)$, whereas in fact this difference is slightly bigger due to the curvature of the equipotential lines in the vicinity of the drain (Figure 9.6). The best agreement between the two solutions should be expected for the location of the drain in the middle of the freshwater zone. The flow rates obtained by this method were correct.

9.3 Upconing Under a River

The second problem is concerned with saltwater upconing under a river, which flows through an unconfined freshwater $(\gamma_F = 1.00)$ alluvial aquifer (Figure 9.7) underlain by a semi-impervious layer of conductivity K_o and thickness b_o, which separates the alluvial aquifer from a deep saltwater aquifer whose constant saltwater potential ϕ_o^S is equal to 49.56 meters (Kemblowski, 1985). The hydraulic conductivities K_F and K_S are 2.00 meters/day and 2.06 meters/day respectively. The saltwater $(\gamma_S = 1.03)$ flows through the semi-confining layer and upcones under the river. The geometry

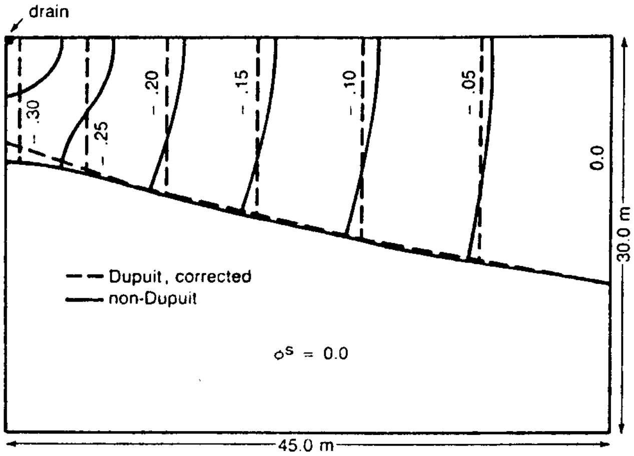

Figure 9.6 Interface location and freshwater flow net, $\phi_D = -.564$ m.

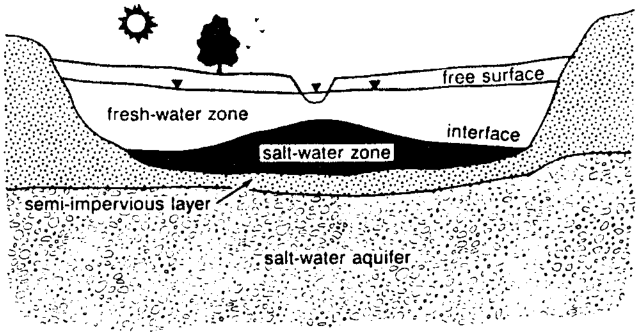

Figure 9.7 Hydrogeologic scheme of saltwater upconing under a river.

and boundary conditions of a simplified hydrologic scheme are shown in Figure 9.8. The location of the interface and the free surface, obtained by the "Dupuit" and "non-Dupuit" models for the rate of effective recharge Q equal to 2.6 X 10^{-3} meters/day, are shown in Figure 9.9. The results show good agreement, and apparently no correction for the Dupuit approximation is required. For the same hydrologic conditions, a transient simulation was performed. The initial conditions were those obtained for the steady state and Q = 2.0 X 10^{-3} meters/day. Then the recharge was increased to Q = 4.0 X 10^{-3} meters/day, and the behavior of the system was simulated for various ratios of K_0/b_0. The rise of the interface crest versus time, calculated by both methods, is shown in Figure 9.10. The methods produced close results, which may be attributed to the fact that the river is almost fully penetrating.

9.4 Summary and Conclusions

Investigation of the impact of the Dupuit-Forchheimer approximation on saltwater-upconing simulation has been presented. The results indicate that as long as the sinks or sources are of a vertical size comparable with the thickness of the freshwater zone, the location of the interface calculated by the "Dupuit" model gives satisfactory results, even though a strong vertical flow obviously occurs in some regions (above the semi-confining layer, below the free surface, along the river-valley boundaries, and under the river). However, when the size of the sink is small compared to the thickness of the freshwater zone, the use of the Dupuit approximation may cause substantial errors in the estimation of the interface location.

For one case of practical interest (a drain located at the top of an aquifer), a correction method was proposed and verified. The same correction method may be used to simulate partially penetrating rivers, ditches, and

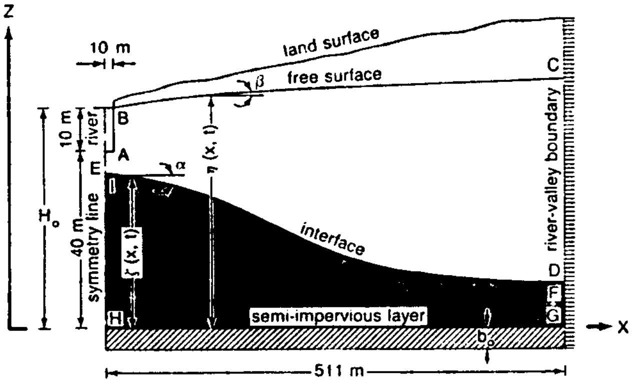

Figure 9.8 Geometry and boundary conditions of upconing under a river.

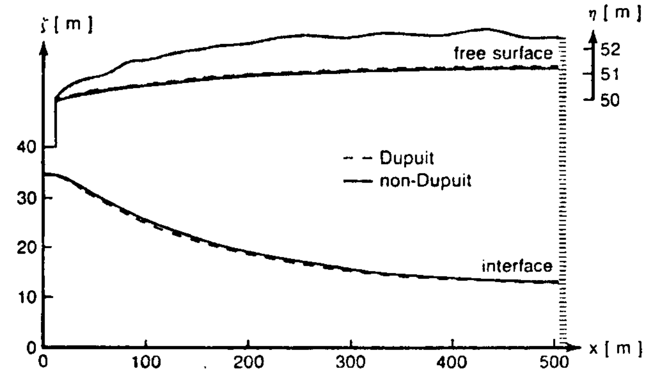

Figure 9.9 Steady-state location of free surface and interface.

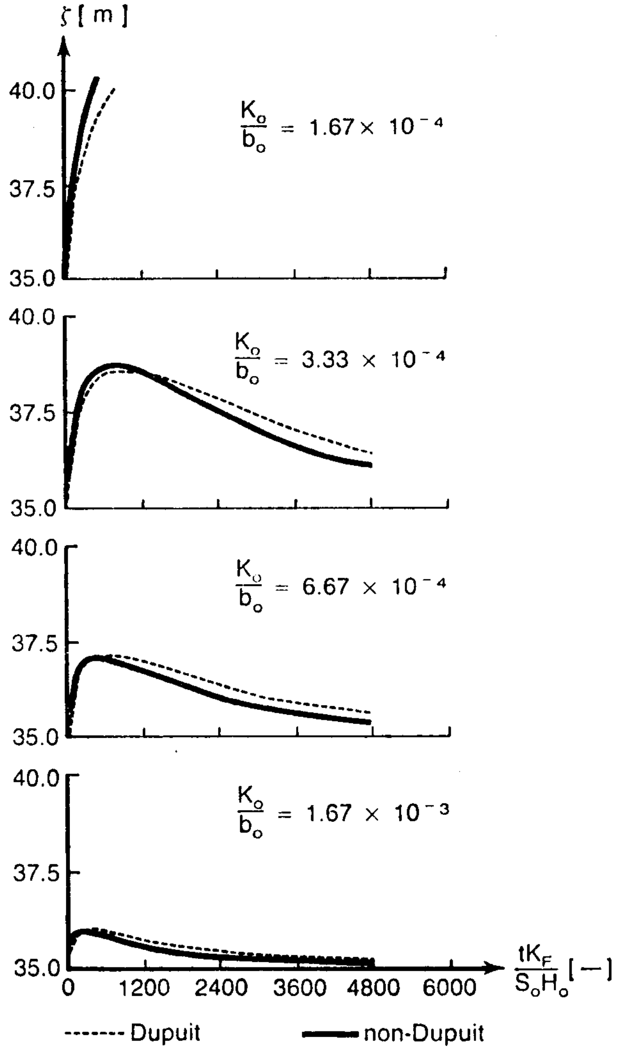

Figure 9.10 Rise of interface under a river.

skimming wells. The analytical solutions for the additional loss of the potential $\Delta\phi^F$ (Eq. 9.8) may be found in Huisman (1972). This procedure may be used in two-dimensional, confined or unconfined, horizontal-flow models.

Another conclusion that may be derived from the analysis of the numerical results is that the Ghyben-Herzberg approximation which assumes constant potential in the whole saltwater zone (and therefore no flow there) would lead to erroneous results for the upconing under a river problem. If this approximation were used, then both $\phi^F(\phi_R^F)$ and $\phi^S(\phi_o^S)$ would be kept constant in the river node, and no rise of the interface crest due to increased effective recharge would occur (see eq. 9.3). Therefore the Ghyben-Herzberg approximation should be used only after careful analysis of the simulated system; whenever the flow in the saltwater zone may be of some importance, this approximation should not be applied.

10. APPROXIMATE TRANSITION ZONE MODEL OF SALTWATER UPCONING IN AQUIFERS

Due to transient boundary conditions (pumpage, river-stage fluctuations), a relatively wide dispersive transition zone may develop between the freshwater and saltwater zones. A simplified description of the dispersive zone that uses the concept of the boundary layer was presented by Rubin and Pinder (1977) and Rubin (1983). In this study, we use this concept to develop a solution for saltwater upconing and to analyze the mechanism of the development of the transition zone.

10.1 Development of the Model

The solution development assumes several approximations; therefore, it is important to emphasize that all of them have to be verified if a practical problem is to be solved. It is assumed that the Dupuit-Forchheimer approximation is valid in the freshwater and saltwater zones, thus the Darcian velocities in both zones are horizontal. The velocity-distribution function (shape function) and the concentration-distribution function within the transition zone are also assumed to be known and are similar to finite-element basis functions. The velocity distribution is given by

$$V_T(\eta) = U\,F(\eta) + V\,G(\eta) \tag{10.1}$$

where U and V are, respectively freshwater and saltwater Darcian velocities, F and G are distribution functions and $V_T(\eta)$ is the ground-water velocity in the transition zone, η is a dimensionless vertical coordinate given by

$$\eta = \frac{Z - Z_b}{\delta} \tag{10.2}$$

Z is the vertical coordinate, Z_b is the elevation of the bottom of the transition zone, and δ is the transition-zone thickness.

The concentration distribution may be described in a similar manner by

$$C(\eta) = C_F K(\eta) + C_S L(\eta) \tag{10.3}$$

where C_F is the freshwater concentration, C_S is the saltwater concentration K and L are distribution functions and $C(\eta)$ is the concentration in the transition zone. Assuming that the freshwater concentration is equal to zero, equation 10.3 may be simplified to

$$C(\eta) = C_s L(\eta) \tag{10.4}$$

In the following development, we assume that the aquifer is unconfined. The analysis may be easily modified for confined conditions. Equation 10.4 may be used to derive a relationship between the freshwater and saltwater potentials (ϕ^f and ϕ^s), which are defined by

$$\phi^f = z + p/\gamma_f \tag{10.5}$$

and

$$\phi^s = z + p/\gamma_s \tag{10.6}$$

where p is the pressure and γ_f and γ_s are freshwater and saltwater specific weights.

Assuming that the flow in the transition zone is horizontal, we obtain the following relationship for the pressure difference between the top and the bottom of the transition zone:

$$\Delta p = p_t - p_b = -\int_{Z_b}^{Z_t} \gamma dZ \qquad (10.7)$$

Z_t is the elevation of the top of the transition zone. Using the following relation between the specific weight and the concentration (the equation of state)

$$\gamma = \gamma_f(1 + \alpha C), \qquad (10.8)$$

we may evaluate the pressure difference as follows:

$$\Delta p = -\int_{Z_b}^{Z_t} \gamma_f(1 + \alpha C)dz = -\gamma_f(\delta + \alpha C_s\delta\int_o^1 L(\eta)d\eta)$$

$$= -\gamma_f(\delta + \alpha\delta C_s\bar{L}) \qquad (10.9)$$

where $\bar{L} = \int_o^1 L(\eta)d\eta$.

This pressure difference also may be estimated from equations 10.5 and 10.6.

$$\Delta p = \gamma_f\phi^f - \gamma_s\phi^s - \gamma_f Z_t + \gamma_s Z_b \qquad (10.10)$$

Combining equations 10.8, 10.9, and 10.10 leads to

$$\gamma_f(1+\alpha C_s)\phi^s - \gamma_f\phi^f + \gamma_f Z_t - \gamma_f(1+\alpha C_s)Z_b = \gamma_f(\delta+\alpha\delta C_s\bar{L}) \qquad (10.11a)$$

or

$$(1+\alpha C_s)\phi^s - \phi^f - \alpha C_s Z_b = \alpha\delta C_s\bar{L} \qquad (10.11b)$$

Using equation 10.11b, the saltwater potential may be expressed as follows:

$$\phi^s = \frac{1}{1+a} (\phi^f + aZ_b + a\bar{I}\delta) \tag{10.12}$$

where $a = \alpha C_s$.

10.2 Flow Continuity for Freshwater and Transition Zones

We are considering unconfined ground-water flow in the freshwater and transition zones. The continuity equation for both zones as a unit may be written as follows:

$$\nabla(q) = - n \frac{\partial \phi^f}{\partial t} + n \frac{\partial Z_b}{\partial t} + N, \tag{10.13}$$

where:

q = horizontal flow rate in the freshwater and transition zones per unit width $(\frac{L^2}{T})$

n = effective porosity (dimensionless)

ϕ^f = freshwater potential (ground-water level for unconfined conditions) (L)

N = recharge (positive) or discharge (negative) $(\frac{L}{T})$

Vector q may be expressed by

$$q = U(\phi^f - Z_t) + \int_{Z_b}^{Z_t} V_T \, dZ \tag{10.14}$$

After substituting equation 10.1 into equation 10.14, we obtain

$$q = U(\phi^f - Z_t) + \delta U \int_0^1 F(\eta) d\eta + \delta V \int_0^1 G(\eta) d\eta . \tag{10.15}$$

When we define $\bar{F}$ and $\bar{G}$ as

$$\bar{F} = \int_{0}^{1} F(\eta)d\eta \text{ and } \bar{G} = \int_{0}^{1} G(\eta)d\eta, \tag{10.16}$$

equation 10.13 may be written as follows:

$$\nabla[(\phi^{f}-Z_{t}+\delta\bar{F})U + \delta\bar{G}V≋ = n(\frac{\partial Z_{b}}{\partial t} - \frac{\partial\phi^{f}}{\partial t}) + N \tag{10.17}$$

where

$$U = -k_{f}\nabla\phi^{f} \tag{10.18}$$

$$V = -k_{s}\nabla\phi^{s}. \tag{10.19}$$

k_f and k_s are hydraulic conductivities in the fresh and saltwater zones, respectively.

Substituting equations 10.12, 10.18, and 10.19 into equation 10.17, we obtain

$$\nabla[k_{f}(\phi^{f}-Z_{t}+\delta\bar{F})\nabla\phi^{f} + \frac{k_{s}\delta\bar{G}}{1+a}(\nabla\phi^{f} + a\nabla Z_{b} + a\bar{L}\nabla\delta)]$$

$$= n(\frac{\partial\phi^{f}}{\partial t} - \frac{\partial Z_{b}}{\partial t}) - N. \tag{10.20}$$

Defining

$$A_{1} = k_{f}(\phi^{f}-Z_{t}+\delta\bar{F}) + \frac{k_{s}\delta\bar{G}}{1+a}, \tag{10.21}$$

$$B_{1} = \frac{k_{s}\delta\bar{G}a}{1+a} \tag{10.22a}$$

and

$$C_1 = B_1\bar{L} \tag{10.22b}$$

equation 11.20 may be written as follows:

$$\nabla(A_1\nabla\phi^f + B_1\nabla Z_b + C_1\nabla\delta) = n\left(\frac{\partial\phi^f}{\partial t} - \frac{\partial Z_b}{\partial t}\right) - N. \tag{10.23}$$

10.3 Mass Transport in the Transition Zone

The solute transport in the transition zone is assumed to be of the advection type, with the exception of dispersive-saltwater flux at the bottom of the transition zone. Under such assumptions the horizontal mass-transport equation may be written as follows:

$$\nabla Q = -\frac{\partial M}{\partial t} - nD_T\frac{\partial C}{\partial Z}\bigg|_{Z_b} + P \tag{10.24}$$

where

Q = solute mass flux in the transition zone,

M = mass of the solute in the transition zone,

D_T = transverse-dispersion coefficient out the bottom of the transition zone and

P = a source or sink in the transition zone.

The transverse-dispersion coefficient is further defined as

$$D_T = \frac{\alpha_T}{n}\,|\,U\,| + D_f \tag{10.25}$$

α_T is the transverse dispersivity and D_f is the molecular-diffusion constant.

The solute mass flux in equation 10.24 may be calculated as follows:

$$Q = \int_{Z_b}^{Z_t} V_T C dz = C_s \delta [U \int_0^1 F(\eta) L(\eta) d\eta + V \int_0^1 G(\eta) L(\eta) d\eta]. \qquad (10.26)$$

Denoting

$$\overline{FL} = \int_0^1 F(\eta) L(\eta) d\eta, \text{ and } \overline{GL} = \int_0^1 G(\eta) L(\eta) d\eta, \qquad (10.27)$$

we obtain

$$Q = C_s (\delta U \overline{FL} + \delta V \overline{GL}) \qquad (10.28)$$

The second term in equation 10.24 may be expressed as follows:

$$\frac{\partial M}{\partial t} = \frac{\partial}{\partial t} (\int_{Z_b}^{Z_t} nCdz) = \frac{\partial}{\partial t} (\delta n C_s \int_0^1 L(\eta) d\eta)$$

$$= n C_s \bar{L} \frac{\partial \delta}{\partial t} \qquad (10.29)$$

The dispersive flow through the bottom of the transition zone may be written as

$$n D_T \frac{\partial C}{\partial Z}\Big|_{Z_b} = n D_T \left[\frac{\partial C}{\partial \eta} \frac{\partial \eta}{\partial Z}\right]_{\eta = 0} = \frac{n D_T C_s}{\delta} \frac{dL(\eta)}{d\eta}\Big|_{\eta = 0} \qquad (10.30)$$

Denoting

$$L'(0) = \left.\frac{dL(\eta)}{d\eta}\right|_{\eta=0}, \tag{10.31}$$

we obtain

$$nD_T \left.\frac{\partial C}{\partial Z}\right|_{Z_b} = nD_T C_s L'(0)/\delta . \tag{10.32}$$

In equation 10.24, P represents the solute mass flux due to a source or sink that is operative in the transition zone. Suppose Q_p is the strength of the source or sink that is evenly distributed vertically through the fresh and transition zones considered as a single unit. We will only consider a sink for P. In that case, the water pumped will have the appropriate concentration for the transition zone. The total solute mass flux is obtained by integrating over the transition zone:

$$P = \frac{Q_p}{(\phi^f - Z_b)} \int_{Z_b}^{Z_t} C dZ = \frac{Q_p \delta C_s}{(\phi^f - Z_b)} \int_0^1 L(\eta) d\eta$$

$$P = \frac{C_s Q_p \delta \overline{L}}{(\phi^f - Z_b)} . \tag{10.33}$$

Substituting equations 10.28, 10.29, 10.32, 10.33, 10.18, 10.19, and 10.12 into equation 10.24 we obtain

$$\nabla\left[\delta\left(k_f \overline{FL} + \frac{k_s \overline{GL}}{1+a}\right)\nabla\phi^f + \delta \frac{k_s \overline{GLa}}{1+a} \nabla Z_b + \delta \frac{k_s \overline{GLa}\,\overline{L}}{1+a} \nabla\delta\right]$$

$$= n\overline{L} \frac{\partial\delta}{\partial t} + nD_T L'(0)/\delta - \frac{Q_p \delta \overline{L}}{(\phi^f - Z_b)} \tag{10.34}$$

Equation 10.34 can be simplified by defining

$$A_2 = \delta\left(k_f\overline{FL} + \frac{k_s\overline{GL}}{1+a}\right) \tag{10.35}$$

$$B_2 = \delta\left(\frac{k_s\overline{GL}a}{1+a}\right) \tag{10.36}$$

$$C_2 = B_2\overline{L} \tag{10.37}$$

The resulting form for equation 10.34 is

$$\nabla(A_2\nabla\phi^f + B_2\nabla Z_b + C_2\nabla\delta) = n\overline{L}\frac{\partial\delta}{\partial t} + D_T L'(0)/\delta - \frac{Q_p\delta\overline{L}}{(\phi^f - Z_b)} \tag{10.38}$$

which is very similar to equation 10.23.

10.4 Flow Continuity in the Saltwater Zone

Saltwater flow continuity may be written as follows:

$$\nabla(q_s) = -n\frac{\partial Z_b}{\partial t} + Q_s \tag{10.39}$$

where

$$q_s = (Z_b - Z_B)\,V \tag{10.40}$$

Z_B = the elevation of the bottom of the aquifer.

Q_s = areal "recharge" of saltwater in the saltwater zone (from underlying formations), may be expressed as a function of the saltwater potential (leaky-aquifer conditions).

Substituting equations 10.12, 10.19, and 10.40 into equation 10.39, we obtain

$$\nabla (k_s(Z_b - Z_B)/(1+a)\ (\nabla \phi^f + a\nabla Z_b + a\bar{L}\nabla\delta) = n \frac{\partial Z_b}{\partial t} - Q_s \qquad (10.41)$$

Introducing the coefficients

$$A_3 = \frac{k_s(Z_b - Z_B)}{1+a} \qquad (10.42)$$

$$B_3 = A_3 a \qquad (10.43)$$

$$C_3 = B_3 \bar{L} \qquad (10.44)$$

allows equation 10.41 to be written as

$$\nabla (A_3 \nabla \phi^f + B_3 \nabla Z_b + C_3 \nabla \delta) = n \frac{\partial Z_b}{\partial t} - Q_s . \qquad (10.45)$$

Equations 10.23, 10.38, and 10.45 complete the mathematical description of the approximate model of saltwater upconing.

10.5 Shape Functions of Velocity and Concentration

The velocity distribution within the transition zone is approximated by equation 10.1. The boundary conditions, which shape functions $F(\eta)$ and $G(\eta)$ are to satisfy, are

$$F(0) = 0 \qquad F(1) = 1 \tag{10.46}$$

$$\frac{dF}{d\eta}(0) = 0 \qquad \frac{dF}{d\eta}(1) = 0 \tag{10.47}$$

$$G(0) = 1 \qquad G(1) = 0 \tag{10.48}$$

$$\frac{dG}{d\eta}(0) = 0 \qquad \frac{dG}{d\eta}(1) = 0. \tag{10.49}$$

The conditions given by equations 10.47 and 10.49 are not necessary; however, they assure the smoothness of the velocity distribution.

The lowest order polynomials that satisfy equations 10.46 through 10.49 are given by

$$F(\eta) = -2\eta^3 + 3\eta^2 \tag{10.50}$$

$$G(\eta) = 2\eta^3 - 3\eta^2 + 1\ . \tag{10.51}$$

The values of the integrals in equation 10.16 may now be calculated:

$$\overline{F} = \int_0^1 (-2\eta^3 + 3\eta^2) = 1/2 \tag{10.52}$$

$$\overline{G} = \int_0^1 (2\eta^3 - 3\eta^2 + 1)\ d\eta = 1/2 \tag{10.53}$$

The shape function of the concentration distribution ($L(\eta)$ in equation 10.4) has the following boundary conditions:

$$L(0) = 1 \qquad\qquad L(1) = 0 \tag{10.54}$$

$$\frac{dL}{d\eta}(1) = 0 \; . \tag{10.55}$$

The lowest order polynomial that satisfies this equation is given by

$$L(\eta) = \eta^2 - 2\eta + 1 \tag{10.56}$$

The derivative of this function at the bottom of the transition zone (which is related to the concentration gradient and therefore to the dispersion through the bottom of the transition zone, given by equation 10.32) can now be evaluated:

$$L'(0) = \left.\frac{dL(\eta)}{d\eta}\right|_{\eta=0} = -2 \tag{10.57}$$

The values of the integrals in equations 10.9 and 10.27 may now be calculated:

$$\overline{L} = \int_0^1 (\eta^2 - 2\eta + 1)\; d\eta = 1/3 \tag{10.58}$$

$$\overline{FL} = \int_0^1 F(\eta)L(\eta)\; d\eta = 1/15 \tag{10.59}$$

$$\overline{GL} = \int_0^1 L(\eta)G(\eta)\; d\eta = 4/15 \tag{10.60}$$

10.6 Numerical Solution

Equations 10.23, 10.38, and 10.45 form a set of three simultaneous equations which must be solved for ϕ^f, Z_b, and δ. For a complete solution, appropriate boundary conditions and initial conditions must also be given. The left-hand side of all three equations consists of terms of the following form:

$$\frac{\partial}{\partial X}\left(W\frac{\partial U}{\partial X}\right) \qquad (10.61)$$

In order to implement a numerical solution, a grid system with grid spacing ΔX is introduced in the X direction. Since the three equations are vertically averaged and since we are only considering a cross sectional model, no spatial derivatives other than X appear in ∇.

A centered finite-difference approximation to equation 10.61, located at node i, is given by

$$\left[\frac{\partial}{\partial X}\left(W\frac{\partial U}{\partial X}\right)\right]_i = [W_{i+1/2}U_{i+1} - (W_{i+1/2} + W_{i-1/2})U_i + W_{i-1/2}U_{i-1}]/\Delta X^2 \qquad (10.62)$$

The half-integer values of W are usually evaluated at node points by the approximation

$$W_{i+1/2} = \frac{1}{2}(W_{i+1} + W_i) \qquad (10.63)$$

Using this approximation, equation 10.62 becomes

$$\left[\frac{\partial}{\partial X}\left(W\frac{\partial U}{\partial X}\right)\right]_i = [(W_{i+1} + W_i)U_{i+1} - (W_{i+1} + 2W_i + W_{i-1})U_i + (W_i + W_{i-1})U_{i-1}]/2\Delta X^2 \qquad (10.64)$$

In equation 10.64, as applied to equations 10.23, 10.38, and 10.45, W may be A_1, A_2, A_3, B_1, B_2, B_3, C_1, C_2, or C_3 and U may be ϕ^f, Z_b, or δ.

In addition to spatial derivatives, the right-hand sides of equations 10.23, 10.38, and 10.45 involve various time derivatives. These time derivatives may be approximated several ways. We consider only two ways. Let time be discretized into invervals Δt and let n, when used as a superscript, denote the nth time step. If n is the current time step for which values are known (either from the initial conditions or a previous time-step solution), then n+1 represents the unknown values at a new time step which are to be solved for. The time derivative may be evaluated as

$$\left[\frac{\partial U}{\partial t}\right]_i^n = \frac{U_i^{n+1} - U_i^n}{\Delta t} \tag{10.65}$$

or

$$\left[\frac{\partial U}{\partial t}\right]_i^{n+1} = \frac{U_i^{n+1} - U_i^n}{\Delta t} . \tag{10.66}$$

Equation 10.65 implies the whole equation is evaluated at time n, and the end result is an explicit procedure with its attendant restriction on time-step magnitude. Equation 10.66 indicates the equation is evaluated at time n+1 and gives an implicit procedure. In equations 10.65 and 10.66, U may be ϕ^f, Z_b or δ.

Using an implicit procedure (equation 10.66) on equation 10.23 gives

$$\left(\frac{A_{1i+1}+A_{1i}}{2\Delta X^2}\right)^{n+1}\phi^{f\,n+1}_{i+1} - \left(\frac{A_{1i+1}+2A_{1i}+A_{1i-1}}{2\Delta X^2}+\frac{n}{\Delta t}\right)^{n+1}\phi^{f\,n+1}_{i}$$

$$+\left(\frac{A_{1i}+A_{1i-1}}{2\Delta X^2}\right)^{n+1}\phi^{f\,n+1}_{i-1} + \left(\frac{B_{1i+1}+B_{1i}}{2\Delta X^2}\right)^{n+1} Z^{n+1}_{bi+1}$$

$$+\left(\frac{n}{\Delta t}-\frac{B_{1i+1}+2B_{1i}+B_{1i-1}}{2\Delta X^2}\right)^{n+1} Z^{n+1}_{bi} + \left(\frac{B_{1i}+B_{1i-1}}{2\Delta X^2}\right)^{n+1} Z^{n+1}_{bi-1}$$

$$+\left(\frac{C_{1i+1}+C_{1i}}{2\Delta X^2}\right)^{n+1}\delta^{n+1}_{i+1} - \left(\frac{C_{1i+1}+2C_{1i}+C_{1i-1}}{2\Delta X^2}\right)^{n+1}\delta^{n+1}_{i}$$

$$+\left(\frac{C_{1i}+C_{1i-1}}{2\Delta X^2}\right)^{n+1}\delta^{n+1}_{i-1} = \frac{n}{\Delta t}\left(Z^{n}_{bi}-\phi^{f\,n}_{i}\right) - N^{n+1}_{i}. \qquad (10.67)$$

In equation 10.67 the new time-level values of the dependent variables have been collected on the left, while the known previous time-level values and the recharge (which should be known) have been kept on the right-hand side. If we consider A, B, and C known, then equation 10.67 has nine unknowns and can be written for each active node. For convenience, equation 10.67 can be written in more compact form:

$$\left[a^{(1)}_{i}\phi^{f}_{i-1}+a^{(2)}_{i}Z_{bi-1}+a^{(3)}_{i}\delta_{i-1}+b^{(1)}_{i}\phi^{f}_{i}+b^{(2)}_{i}Z_{bi}\right.$$

$$\left.+\,b^{(3)}_{i}\delta_{i}+c^{(1)}_{i}\phi^{f}_{i+1}+c^{(2)}_{i}Z_{bi+1}+c^{(3)}_{i}\delta_{i+1}\right]^{n+1}=d^{(1)}_{i}. \qquad (10.68)$$

The new coefficients in equation 10.68 (a, b, c) can be easily identified by comparison with equation 10.67 and then referring to the definition of A_1, B_1, and C_1 (equations 10.21 and 10.22) and using the values of F and G given by equations 10.52 and 10.53:

$$a_i^{(1)} = \{k_f[(\phi_i^f + \phi_{i-1}^f) - (Z_{bi} + Z_{bi-1}) - (\delta_i + \delta_{i-1})/2] + \frac{k_s}{2(1+a)}(\delta_i + \delta_{i-1})\}/2\Delta X^2 \quad (10.69)$$

$$a_i^{(2)} = \frac{k_s a}{4\Delta X^2(1+a)}(\delta_i + \delta_{i-1}) \quad (10.70)$$

$$a_i^{(3)} = a_i^{(2)}/3 \quad (10.71)$$

$$c_i^{(1)} = a_{i+1}^{(1)} \quad (10.72)$$

$$c_i^{(2)} = a_{i+1}^{(2)} \quad (10.73)$$

$$c_i^{(3)} = c_i^{(2)}/3 \quad (10.74)$$

$$b_i^{(1)} = -\frac{n}{\Delta t} - a_i^{(1)} - c_i^{(1)} \quad (10.75)$$

$$b_i^{(2)} = \frac{n}{\Delta t} - a_i^{(2)} - c_i^{(2)} \quad (10.76)$$

$$b_i^{(3)} = -a_i^{(3)} - c_i^{(3)} \quad (10.77)$$

$$d_i^{(1)} = \frac{n}{\Delta t}(Z_{bi} - \phi_i^f)^n \quad (10.78)$$

The same implicit procedure used to obtain equations 10.67 through 10.78 can be applied to the remaining two equations, 10.38 and 10.45. This results in two more equations with nine unknowns similar to equation 10.68.

$$[a_i^{(4)}\phi^f_{i-1} + a_i^{(5)}Z_{bi-1} + a_i^{(6)}\delta_{i-1} + b_i^{(4)}\phi^f_i + b_i^{(5)}Z_{bi} + b_i^{(6)}\delta_i$$

$$+ c_i^{(4)}\phi^f_{i+1} + c_i^{(5)}Z_{bi+1} + c_i^{(6)}\delta_{i+1}]^{n+1} = d_i^{(2)} \qquad (10.79)$$

$$a_i^{(7)}\phi^f_{i-1} + a_i^{(8)}Z_{bi-1} + a_i^{(9)}\delta_{i-1} + b_i^{(7)}\phi^f_i + b_i^{(8)}Z_{bi} + b_i^{(9)}\delta_i$$

$$+ c_i^{(7)}\phi^f_{i+1} + c_i^{(8)}Z_{bi+1} + c_i^{(9)}\delta_{i+1}]^{n+1} = d_i^{(3)}. \qquad (10.80)$$

The coefficients appearing in equations 10.79 and 10.80 are obtained in a manner similar to that used for equations 10.69 through 10.78:

$$a_i^{(4)} = [k_f + \frac{4k_s}{1+a}]\,(\delta_i + \delta_{i-1})/30\Delta X^2 \qquad (10.81)$$

$$a_i^{(5)} = \frac{2k_s a}{15\Delta X^2(1+a)}\,(\delta_i + \delta_{i-1}) \qquad (10.82)$$

$$a_i^{(6)} = a_i^{(5)}/3 \qquad (10.83)$$

$$c_i^{(4)} = a_{i+1}^{(4)} \qquad (10.84)$$

$$c_i^{(5)} = a_{i+1}^{(5)} \qquad (10.85)$$

$$c_i^{(6)} = c_i^{(5)}/3 \qquad (10.86)$$

$$b_i^{(4)} = -a_i^{(4)} - c_i^{(4)} \qquad (10.87)$$

$$b_i^{(5)} = -a_i^{(5)} - c_i^{(5)} \qquad (10.88)$$

$$b_i^{(6)} = \left(b_i^{(5)} - \frac{n}{\Delta t} \right) / 3 \tag{10.89}$$

$$d_i^{(2)} = - \frac{n}{3\Delta t} \delta_i^{n} - \frac{2D_{Ti}^{n+1}}{\delta_i^{n+1}} - \frac{Q_{pi}^{n+1} \delta_i^{n+1}}{3(\phi_i^{fn+1} - Z_{bi}^{n+1})} \tag{10.90}$$

$$a_i^{(7)} = \frac{k_s}{2\Delta X^2 (1+a)} \left(Z_{bi} + Z_{bi-1} - Z_{Bi} - Z_{Bi-1} \right) \tag{10.91}$$

$$a_i^{(8)} = (a)\ a_i^{(7)} \tag{10.92}$$

$$a_i^{(9)} = a_i^{(8)}/3 \tag{10.93}$$

$$c_i^{(7)} = a_{i+1}^{(7)} \tag{10.94}$$

$$c_i^{(8)} = a_{i+1}^{(8)} \tag{10.95}$$

$$c_i^{(9)} = c_i^{(8)}/3 \tag{10.96}$$

$$b_i^{(7)} = -a_i^{(7)} - c_i^{(7)} \tag{10.97}$$

$$b_i^{(8)} = (a)\ b_i^{(7)} - \frac{n}{\Delta t} \tag{10.98}$$

$$b_i^{(9)} = (a)\ b_i^{(7)}/3 \tag{10.99}$$

$$d_i^{(3)} = - \frac{n}{\Delta t} Z_{bi}^{n} - Q_{si}^{n+1} \tag{10.100}$$

Equations 10.68, 10.79, and 10.80 form a tri-tridiagonal system of equations. An efficient algorithm which takes advantage of the sparseness of the coefficient matrix should be used to solve the set of simultaneous equations. If we have N active nodes, it is seen that equations 10.68, 10.79, and 10.80 form a 3N x 3N set of matrix equations to be solved for the 3N unknowns. ϕ^f, Z_b and δ must be found for each of the N active nodes. However, it is clear from equations 10.68, 10.79, and 10.80 that only a maximum of nine unknowns appear in each equation. Therefore, in the 3N x 3N matrix, only a central band of nine diagonals is nonzero. In fact, the three equations (10.68, 10.79, and 10.80) only have six unknowns for the first and last active nodes. This is so because some type of boundary condition must be applied at the ends of the model and this eliminates three of the unknowns. We have written a program to implement von Rosenberg's tri-tridiagonal solution on equations 10.68, 10.79, and 10.80.

Unfortunately, a single solution of equations 10.68, 10.79, and 10.80 for a given time step does not give the correct answer, since the coefficients defined by equations 10.69-10.78 and 10.81-10.100 are themselves functions of ϕ_f, Z_b, and δ at the new time level n+1. In other words, we have a nonlinear set of equations in 10.68, 10.79, and 10.80. Therefore, an iterative scheme must be used at each time step until sufficient accuracy has been obtained. At the beginning of each time step, the preceding time-step values of ϕ^f, Z_b, and δ are used to evaluate the coefficients and start a new iteration. Iteration ceases when there is little change between iterations in ϕ^f, Z_b, and δ. This convergence criteria is specified by the user.

Alternatively, an explicit procedure for solving equations 10.23, 10.38, and 10.45 can be derived by using equation 10.65 for the time derivatives. If this is done, the evaluation of each equation is at time n. The only place where the new time-level values for ϕ^f, Z_b, and δ appear is in the time derivative. Therefore, we have only one unknown in each equation. In this case, the equations decouple and they can be solved sequentially for δ, Z_b, and ϕ^f with simple algebra; no simultaneous-equation solution or matrix solution is required. However, as mentioned earlier, the time step must be kept quite small with this technique to prevent stability problems.

The explicit technique can be implemented easily using the a, b, and c coefficients defined by equations 10.69-10.78 and 10.81-10.100 with only minor changes. First, the $n/\Delta t$ part in equations 10.75, 10.76, 10.89, and 10.98 must be dropped. Second, the time evaluations in equations 10.90 and 10.100 must all be at the old time-level n. With these changes, we can define a new set of coefficients (ac, bc, ce, and de) for the explicit procedure:

$$ae_i^{(m)} = a_i^{(m)} \qquad m = 1,2,3 \quad 9 \qquad (10.101)$$

$$ce_i^{(m)} = c_i^{(m)} \qquad m = 1,2,3 \quad 9 \qquad (10.102)$$

$$be_i^{(m)} = -a_i^{(m)} - c_i^{(m)} \qquad m = 1,2,3 \quad 9 \qquad (10.103)$$

$$de_i^{(1)} = d_i^{(1)} \qquad (10.104)$$

$$de_i^{(2)} = -\frac{n}{3\Delta t}\delta_i^n - \frac{2D_{Ti}^n}{\delta_i^n} - \frac{Q_{pi}^n \delta_i^n}{3(\phi_i^f - Z_{bi})^n} \qquad (10.105)$$

$$de_i^{(3)} = -\frac{n}{\Delta t} Z_{bi}^n - Q_{si}^n \qquad (10.106)$$

The explicit equations can then be written in the following form:

$$\phi_i^{fn+1} = Z_{bi}^{n+1} + \frac{\Delta t}{n}\Big[ae_i^{(1)}\phi_{i-1}^{f} + ae_i^{(2)}Z_{bi-1} + ae_i^{(3)}\delta_{i-1} + be_i^{(1)}\phi_i^{f} + be_i^{(2)}Z_{bi} + be_i^{(3)}\delta_i + ce_i^{(1)}\phi_{i+1}^{f} + ce_i^{(2)}Z_{bi+1} + ce_i^{(3)}\delta_{i+1}\Big]^n - \frac{\Delta t}{n}\, de_i^{(1)} \qquad (10.107)$$

$$\delta_i^{n+1} = \frac{3\Delta t}{n}\Big[ae_i^{(4)}\phi_{i-1}^{f} + ae_i^{(5)}Z_{bi-1} + ae_i^{(6)}\delta_{i-1} + be_i^{(4)}\phi_i^{f} + be_i^{(5)}Z_{bi} + be_i^{(6)}\delta_i + ce_i^{(4)}\phi_{i+1}^{f} + ce_i^{(5)}Z_{bi+1} + ce_i^{(6)}\delta_{i+1}\Big]^n - \frac{3\Delta t}{n}\, de_i^{(2)} \qquad (10.108)$$

$$Z_{bi}^{n+1} = \frac{\Delta t}{n}\Big[ae_i^{(7)}\phi_{i-1}^{f} + ae_i^{(8)}Z_{bi-1} + ae_i^{(9)}\delta_{i-1} + be_i^{(7)}\phi_i^{f} + be_i^{(8)}Z_{bi} + be_i^{(9)}\delta_i + ce_i^{(7)}\phi_{i+1}^{f} + ce_i^{(8)}Z_{bi+1} + ce_i^{(9)}\delta_{i+1}\Big]^n - \frac{\Delta t}{n}\, de_i^{(3)} \qquad (10.109)$$

It is clear that equations 10.108 and 10.109 may be solved in any order since they only depend on old time-level values. However, equation 10.107 can only be solved after equation 10.109 has been solved since Z_{bi}^{n+1} is needed on the right-hand side of 10.107.

10.7 Results and Conclusions

We have written implicit and explicit computer programs to implement the equations given in the previous section. In order to check the validity of the computer programs, several tests were run. In particular, analytical results can be obtained for simple cases. The simplest test was to see if initial horizontal surfaces for ϕ^f, Z_b and δ were maintained with no imposed stresses. Then the effects of constant areal recharge of freshwater, constant areal recharge of saltwater, and constant areal hydrodynamic dispersion were tested independently. The program results checked with known analytical behavior.

The area of interest in this study is the alluvial river valley of the Smoky Hill River between Salina and Solomon. McElwee (1985) has worked with this area using the sharp interface approximation. In applying the transition-zone model currently under investigation, we will use the same physical parameters he used. These are only gross averages for the area and cannot be considered site specific.

$k_f = 300$ ft/day

$n = .15$

$N = .00197$ ft/day

$a = .2$

$\gamma_f = 1.0$

$\gamma_s = 1.2$

$Q_s = .0000974$ ft/day

$\Delta x = 231$ ft

The model was set up with 79 active nodes. The river is at node 40 with a base flow from the ground-water system of $Q_p = .154$ foot/day. Barrier boundaries (zero slope) are assumed for all three quantities ϕ^f, Z_b, and δ at nodes 0 and 80. The maximum saturated thickness in this area is about 40 feet. Using this data McElwee (1985) found that unstable upconing was occurring under the river. The profile generated by this sharp-interface approximation is shown in Figure 10.1. The interface was assumed to intercept the bottom of the river when it was 10 feet below the water table at node 40.

As further checks on the validity of the new computer programs, a few other tests were run. The transition zone and saltwater zone can be disabled in the code so only the freshwater zone is modeled. We ran a few situations to verify that the freshwater zone was being modeled correctly. By setting $\delta = 0$, we have the sharp-interface approximation. We attempted to reproduce the sharp-interface result shown in Figure 10.1. The interface produced by the current programs was a little wider near the river than Figure 10.1, but was of acceptable accuracy. Lastly, the implicit and explicit programs were written separately using different numerical techniques. Therefore, a good comparison of results between the two would indicate both are working correctly. This was the case for several test runs. These transition-zone programs are still in the development stage and need further testing along with the addition of more useful features.

One of the objectives of this study was to see if the transition zone model developed here would significantly affect the previous sharp interface results. The new parameter to be introduced is the dispersivity α_T. This will control the amount of hydrodynamic dispersion that is occurring. We have run the transition zone model for a range of α_T letting it approach a steady state profile in each case. The profiles for two values of α_T are shown in Figures 10.2 and 10.3. It is seen that in both cases we still have unstable upconing under the river. Additional runs indicate that for all reasonable values of α_T we still get unstable upconing. This was a little surprising. We had originally supposed that for large enough α_T a stable upconing situation would occur. It appears that the saturated thickness in this area is just too thin for that to happen.

The conclusion seems to be that although dispersion has an effect on the ground-water concentration profile, it is not the major mechanism feeding saltwater to the river. The convective effect causes the unstable upconing and feeds the major part of the saltwater to the river. Field data collected for this project suggest that the concentrations fall off away from the river

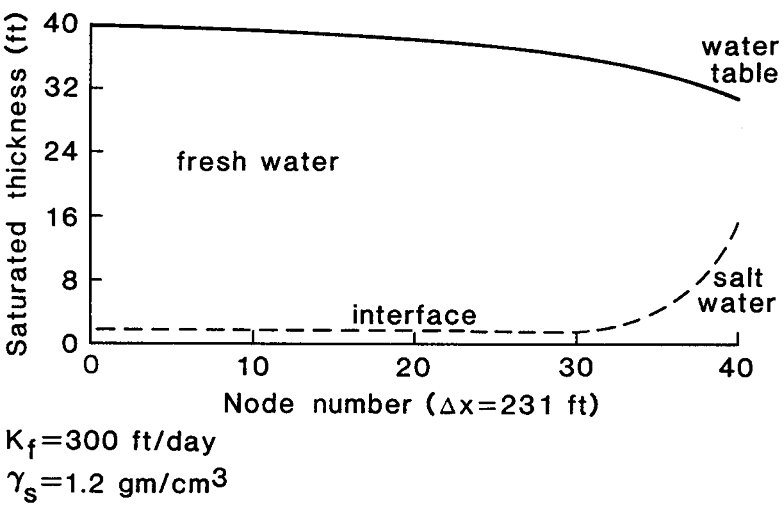

Figure 10.1 The sharp interface approximation of the Smoky Hill cross-section; after McElwee (1985).

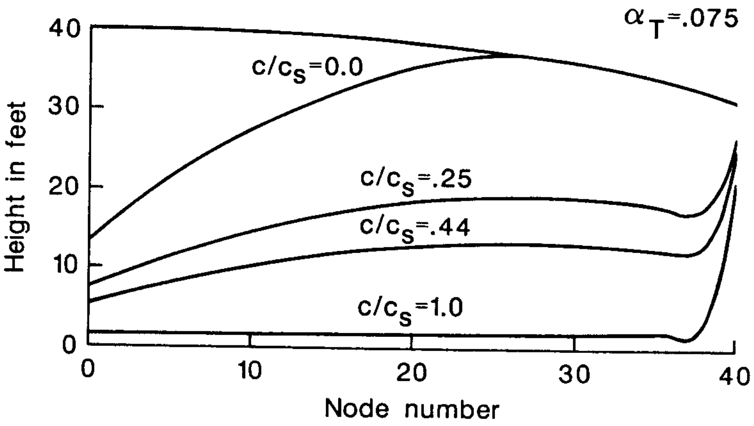

Figure 10.2 Salt concentration profile for $\alpha_T = 0.075$.

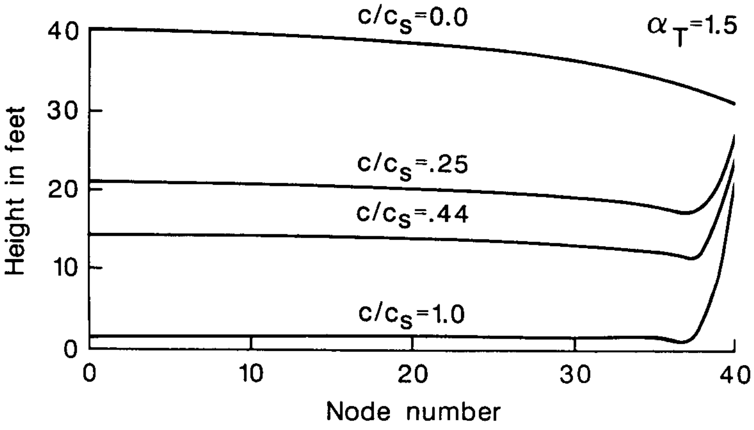

Figure 10.3 Salt concentration profile for $\alpha_T = 1.5$.

faster than shown in Figure 10.3. Therefore, one might expect an upper limit on α_T in this area to be about 1.0. If one is primarily interested in the concentration profile in the ground-water system, it is clear that the transition zone must be considered either by the present approximate model or a more rigorous model. However, it appears that the unstable upconing is a strong enough effect that the discharge of saltwater to the river can be understood mainly in terms of the sharp interface approximation (McElwee, 1985).

11. A DENSITY-DEPENDENT GROUND-WATER FLOW AND SOLUTE-TRANSPORT MODEL

The movement of saltwater in a density-dependent miscible flow system is described by the coupled equations of fluid continuity, Darcy velocity, solute transport and a state equation relating fluid density to the salt concentration. The solution of these equations is obtained here with the use of finite-element method. The specific characteristic of the proposed model is its improved accuracy and its capability in preserving the continuity of the velocity field, which are both essential in simulation of advective-dominated transport problems.

11.1 Governing Equations

The major components of the transport process in a miscible flow system are advection and dispersion (Bear, 1979). Advection is a process by which fluid particles are moved as a result of pressure and elevation differences while dispersion refers to the mixing and spreading of liquid particles caused by molecular diffusion, pore-size scale variations of velocity and large-scale heterogeneities. The effects of these processes is summarized in an equation of solute-mass continuity or the so-called advection-dispersion equation.

The distribution of solute (salt) concentration in a freshwater/saltwater system can be obtained by simultaneous solution of the coupled equations of fluid continuity, Darcy velocity and solute-mass continuity. The general form of these equations for two-dimensional cross sectional flow is expressed as

fluid continuity, $$\frac{\partial}{\partial x_i}(q_i) = 0 \qquad (11.1)$$

Darcy velocity, $$q_i = -\frac{k_{ij}}{\mu}\left(\frac{\partial p}{\partial x_j} + \rho g_j\right) \qquad (11.2)$$

solute transport, $\frac{\partial}{\partial x_i}(D_{ij}\frac{\partial c}{\partial x_j}) - \frac{\partial}{\partial x_i}(q_i c/\theta) = \frac{\partial c}{\partial t}$ (11.3)

where c represents the solute concentration; p is the pressure; q_i is the component of Darcy velocity in i-direction; ρ represents the fluid density; k_{ij}'s are components of the permeability tensor; D_{ij}'s are components of the dispersion coefficient; g_j is the component of gravitational vector in j-direction; μ is the fluid viscosity; θ is the effective porosity; $x_i (i=1,2)$ are the Cartesian coordinates; and t is the time variable. In derivation of the fluid-balance equation (11.1), the release of water from storage is assumed to have a negligible effect on movement of the saltwater front. This assumption is justified in the absence of heavy pumping activities. We have also assumed that porosity, θ, and dynamic viscosity, μ, are constant in time and space.

Note that there are four unknowns in equations (11.1)-(11.3); i.e. ρ, q_i, p and c, but only three equations. The additional equation required for solution of these equations is a relationship between fluid density and salt concentration. Such a relationship is obtained by writing the first order Taylor expansions of fluid density about a base density and concentration:

$$\rho = \rho(c) \simeq \rho_o + \frac{\partial \rho}{\partial c}(c - c_o) \qquad (11.4)$$

where ρ_o is the base fluid density at base-concentration c_o (the base condition is usually taken as that of freshwater in which case ρ_o = density of freshwater and $c_o = 0$); and $\frac{\partial \rho}{\partial c}$ is a constant value, representing variation in density with concentration which is obtained empirically.

The components of the dispersion coefficient, D_{ij}, are taken as functions of average pore velocity, and for a porous medium isotropic with respect to dispersivity, they are expressed as (Bear, 1979)

$$D_{ii} = \alpha_L \frac{v_i^2}{v} + \alpha_T \frac{v_j^2}{v} + D_d T_{ii} \quad (i = 1,2) \tag{11.5a}$$

$$D_{ij} = D_{ji} = (\alpha_L - \alpha_T) \frac{v_i v_j}{v} \tag{11.5b}$$

where α_L and α_T are respectively the longitudinal and transverse dispersivities; $v_i = \frac{q_i}{\theta}$ are components of the pore velocity lv, D_d is the molecular-diffusion coefficient and T_{ii} (i=1,2) are the principal components of the tortuosity tensor.

Solution of equations (11.1)-(11.4) requires additional information in the form of initial and boundary conditions. As initial condition we must be given the salt concentration at some initial time, t_o, at all spatial points, that is

$$c(x;t=t_o) = c_o(x) \qquad \text{for } x\varepsilon\Omega \tag{11.6}$$

where Ω indicates the spatial domain and c_o is a known function. c_o is used as a starting point to find the transient variations in solute concentration. The initial pressure distribution is not needed due to the elimination of the transient storage term in equation (11.1). In other words the propagation of pressure has been assumed to be instantaneous. However, the pressure can change temporally because of the changes in fluid density.

The boundary conditions associated with the ground-water flow equations (11.1) and (11.2) may be of either the Dirichlet (specified pressure) type or the Neumann (specified flux) type. The Dirichlet boundary condition requires that the pressure distribution at points along some portion of boundary, Γ_1, remain the same as certain prespecified values, i.e.

$$p(x,t) = p_d(x,t) \qquad \text{for } x \varepsilon \Gamma_1 \qquad (11.7a)$$

where P_d represents a given pressure distribution. This type of boundary condition is usually used as a far-field boundary where no appreciable change in piezometric surface is expected to take place.

The Neumann boundary condition specifies the flux normal to the boundary segment Γ_2 as

$$q(x,t) = q_n(x,t) \qquad \text{for } x \varepsilon \Gamma_2 \qquad (11.7b)$$

where q_n is the specified Darcy flux. $\Gamma = \Gamma_1 + \Gamma_2$ is the total boundary of the spatial domain. An impermeable boundary is a special case of Neumann boundary conditions. In the case of leakage through a semipervious boundary, the normal flux can be evaluated in terms of the hydraulic-head differential and the material properties of the leaky layer (Frind, 1982b).

As is obvious from equations (11.7a) and (11.7b), the Dirichlet and Neumann boundary conditions can be time-dependent. However, the transient variations of these terms are usually ignored for most practical situations.

In obtaining the solution of the solute-transport equation (11.3), the boundary conditions must be specified for all time periods. The types of conditions which are commonly encountered in actual field problems include the conditions of prescribed concentration and a more complicated form of prescribed flux. The prescribed concentration distribution is usually given in the form of

$$c(x,t) = c_d(x,t) \qquad \text{for } x\varepsilon\Gamma_3 \qquad (11.8a)$$

where c_d is the functional form of a specified concentration. The prescribed flux condition (also known as the Cauchy condition) is expressed by

$$\left(\frac{q_i}{\theta} c - D_{ij} \frac{\partial c}{\partial x_j}\right) n_i = \frac{q_n}{\theta} c_n \qquad \text{for } x\varepsilon\Gamma_4 \qquad (11.8b)$$

where n_i is the i-th component of the outward unit vector normal to the boundary c_n is the concentration of the inflowing fluid through the boundary and $\Gamma = \Gamma_3 + \Gamma_4$ is again the spatial-aquifer boundary. Equation (11.7b) is usually used in the case of an inflow boundary when the rate and concentration of the entering fluid, q_n and c_n, are given. If flow is leaving the boundary, q_n and c_n are unknown. In such case the advective flux normal to the boundary is assumed to remain the same on both sides of the boundary. As a result of this, the boundary condition (11.8b) degenerates into the Neumann-type boundary conditions of the form:

$$\frac{\partial c}{\partial n} = 0 \qquad \text{for } x\varepsilon\Gamma_4 \qquad (11.8c)$$

Equation (11.8c) also applies to an impermeable boundary in which case the normal flux, q_n, becomes zero.

With the specification of the governing equations along with the initial and boundary conditions, the mathematical description of a miscible-flow system is complete. The system of equations (11.1)-(11.4) are coupled by the fact that the solution of the solute-transport equation (11.3) requires an appropriate representation of velocity field which depends on the fluid density which, in turn, is evaluated on the basis of solute concentration. The solution of such a complex nonlinear system of equations can be obtained with an iterative numerical scheme and this will be described in the subsequent section.

11.2 Galerkin Finite-Element Solution

The Galerkin finite-element method is a combination of the Galerkin approach to generating approximate integral equations and the finite-element method of integration. The Galerkin approach has been shown to be extremely valuable, especially in connection with nonlinear problems. However, it is the ability of finite elements to accurately represent irregular geometry that has made this technique quite popular for analysis of ground-water problems. Although most of the previous work has been performed on linear ground-water problems, several studies have shown that finite-element techniques can also achieve a level of efficiency sufficient to handle large nonlinear transient problems (see Frind, 1982b; Voss, 1984).

Quite frequently, the numerical solution of the governing equations (11.1) and (11.2) is carried out by first writing the fluid-continuity equation in terms of pressure, incorporating the equations for velocity. The pressure distribution obtained from solution of the resulting equation is then used in the set of equations for velocity to determine the Darcy velocity components. For situations characterized by smooth variations of pressure, this approach indeed has been proven to be quite effective requiring minimal computational efforts. Inherent in this approach is, however, a discontinuity in the velocity field across the inter-elemental boundaries when zero-order continuous-basis functions are used to represent the pressure (Pinder and Gray, 1976). The discontinuity in velocity leads to a violation of conservation of mass in a local sense. This lack of continuity can distort the solution of the solute-transport equation for advective-dominated transport problems.

In an attempt to achieve a continuous-velocity field, Meissner (1973) suggested a mixed formulation for solving the fluid continuity and Darcy velocity equations simultaneously. This approach leads directly to the nodal values of pressure and velocity. Segol et al. (1975) used the mixed finite-element formulation within the context of a saltwater-intrusion model. The results of their analysis showed a significant improvement but at the expense of a considerable increase in computations. Consequently very few future applications of this technique have been reported in the ground-water literature. The use of mixed finite-element method has received a great popularity in problems of fluid mechanics.

A mixed finite-element formulation is utilized here for simultaneous solution of the fluid continuity and Darcy velocity equations. We will show that with careful construction of approximate equations, the efficiency of numerical computations can be improved substantially. Having obtained an appropriate velocity field we then proceed to demonstrate the solution of the solute-transport equation using a standard Galerkin finite-element method. As indicated before because of the nature of density-dependent flow conditions, the solution scheme involves an iterative process. At each time step the concentration solution is used in equation (11.4) to update the point values of the fluid density. The whole solution process is then repeated once more using the updated densities and accordingly a new set of pressures, velocities and salt concentrations are obtained. This operation continues until the solutions have converged at which time we proceed to solve the governing equations for the next time period.

11.2.1 Fluid Continuity and Darcy Velocity Equations

The first step in the Galerkin formulation of the approximate equations is to assume a set of trial solutions of the form:

$$p(x,z,t) \simeq \sum_{j=1}^{m} p_j\,(t)\,\phi_j\,(x,z) \tag{11.9a}$$

$$q_x(x,z,t) \simeq \sum_{j=1}^{n} q_{xj}\,(t)\,\varphi_j(x,z) \tag{11.9b}$$

$$q_z\,(x,z,t) \simeq \sum_{j=1}^{n} q_{zj}\,(t)\,\varphi_j(x,z) \tag{11.9c}$$

where $p_j(t)$, $q_{xj}(t)$ and $q_{zk}(t)$ are, respectively, the unknown nodal values of pressure, x-component of velocity and z-component of velocity; x and z are the Cartesian coordinates, and ϕ_j and φ_j are an appropriate set of basis function and m and n are the number of nodes used for approximation of pressure and velocity. Note that p, q_x and q_z are dependent on time due to the fact that the fluid density changes with concentration. The choice of basis functions, ϕ_j and φ_j are affected by the level of accuracy required. Optimum efficiency and accuracy are achieved only when the variation in pressure is approximated by basis functions of one order lower than those used for defining the velocity distributions. The common practice is to use quadrilateral elements with eight nodes to represent the velocity and then use only the corner nodes for approximating pressure.

The differential operators associated with equations (11.1) and (11.2) are written as

$$L(q_x, q_z) = \frac{\partial}{\partial x}(q_x) + \frac{\partial}{\partial z}(q_z) = 0 \qquad (11.10a)$$

$$L(q_x, p) = q_x + \frac{k_{xx}}{\mu}\left(\frac{\partial p}{\partial x}\right) = 0 \qquad (11.10b)$$

$$L(q_z, p) = q_z + \frac{k_{zz}}{\mu}\left(\frac{\partial p}{\partial x} - \rho g\right) = 0 \qquad (11.10c)$$

where, for simplicity, the two-dimensional x-z coordinate system is taken to be the horizontal and vertical directions and it is further assumed that the x-z axes are colinear with the principal directions of the permeability tensor. As a result of this latter assumption, the terms involving $k_{xz} = k_{zx} = 0$ have been eliminated from equations (11.10b) and (11.10c). Note also from equation (11.10b) that the body-force term which has zero component in the horizontal direction, x, has been eliminated.

The next step is to substitute the trial solutions in equations (11.10a), (11.10b) and (11.10c); the residuals of the equations are subsequently multiplied by the appropriate basis functions and are, then, integrated over the spatial domain. By the orthogonality condition of the Galerkin theory, the resulting set of algebraic equations must be set to zero. This operation will eventually lead to the following set of approximate equations to be solved for pressure and Darcy velocity components:

$$[K_x]\{q_x\} + [K_z]\{q_z\} = \{f_Q\} \qquad (11.11a)$$

$$[M_x]\{q_x\} + [L_x]\{p\} = \{f_x\} \qquad (11.11b)$$

$$[M_z]\{q_z\} + [L_z]\{p\} = \{f_z\} \qquad (11.11c)$$

where $\{p\} = (p_1, p_2, \ldots, p_m)^T$, $\{q_x\} = (q_{x1}, q_{x2}, \ldots, q_{xn})^T$, and $\{q_z\} = (q_{z1}, q_{z2}, \ldots, q_{zn})^T$ are vectors of unknown nodal variables; and the components of coefficient matrices $k_x(m*n)$, $k_z(m*n)$, $L_x(n*m)$, $M_x(n*n)$, $M_z(n*n)$ and the right-hand-side vectors $f_Q(m*1)$, $f_x(n*1)$ and $f_z(n*1)$ are expressed by

$$K_x(i,j) = \int_\Omega\int \frac{\partial}{\partial x} (\psi_j)\, \phi_i \, d\,\Omega \qquad i=1,m;\ j=1,n$$

$$K_z(i,j) = \int_\Omega\int \frac{\partial}{\partial z} (\psi_j)\, \phi_i \, d\,\Omega \qquad i=1,m;\ j=1,n$$

$$L_x(i,j) = \int_\Omega\int \left(\frac{k_{xx}}{\mu}\right) \frac{\partial}{\partial x} (\phi_j)\, \psi_i \, d\,\Omega \qquad i=1,n;\ j=1,m$$

$$L_z(i,j) = \int_\Omega\int \left(\frac{k_{zz}}{\mu}\right) \frac{\partial}{\partial z} (\phi_j)\, \psi_i \, d\,\Omega \qquad i=1,n;\ j=1,m$$

$$M_x(i,j) = M_z(i,j) = \int_\Omega\int \psi_j\, \psi_i \, d\,\Omega \qquad i=1,\ n;\ j=1,n$$

$$f_Q(i) = 0 \qquad i=1,m; \quad f_x(i) = 0 \quad i=1,n$$

$$f_z(i) = \int_\Omega\int \left(\frac{k_{zz}}{\mu}\right) \rho g \psi_i \, d\,\Omega \qquad i=1,n$$

Incorporation of boundary conditions in the set of equations (11.11) is carried out simply by moving the terms including the known values of p_j, q_{xj} and q_{zj} to the right-hand sides. The equations corresponding to the nodes with prescribed pressure and prescribed flux conditions are subsequently eliminated from further analysis. The remaining set of equations ready to be solved will look very similar to (11.11) and will not be rewritten; however, to reflect the modification made by incorporation of boundary conditions, hereafter we use $\overline{K}_x$, $\overline{K}_z$, $\overline{L}_x$, $\overline{L}_z$, $\overline{M}_x$ and $\overline{M}_z$ as coefficient matrices; $\overline{f}_Q$, $\overline{f}_x$ and $\overline{f}_z$ as right-hand-side vectors; and $\overline{p}$, $\overline{q}_x$ and $\overline{q}_z$ as unknown terms. Note that the dimensions of these terms are smaller than their original counterparts in the set of equations (11.1). Moreover, certain components of the right-hand-side vectors that were previously zero, may now contain non-zero contributions of the boundary conditions.

The set of linear equations (11.11) or its modified version can be solved simultaneously as was shown by Segol et al. (1975). This approach, however, takes a considerable amount of computer time and storage. An alternative approach is to decompose the system into three separate equations to be solved for $\overline{P}$, $\overline{q}_x$ and $\overline{q}_z$. The decomposition is carried out by elimination of $\overline{q}_x$ and $\overline{q}_z$ from equation (11.11a) using the relationship (11.11b) and (11.11c). The resulting set of equations to be solved for pressure is derived to be

$$[A]\{\overline{p}\} = \{Q\} \tag{11.12}$$

where $[A] = [\overline{K}_x]\,[\overline{M}_x]^{-1}\,[\overline{L}_x] + [\overline{K}_z]\,[\overline{M}_z]^{-1}\,[\overline{L}_z]$

and $\{Q\} = [\overline{K}_x]\,[\overline{M}_x]^{-1}\,\{\overline{f}_x\} + [\overline{K}_z]\,[\overline{M}_z]^{-1}\,\{\overline{f}_z\} - \{\overline{f}_Q\}$.

The pressure distribution, $\overline{p}$, calculated from equation (11.12) is substituted in the following equations for computation of velocity components:

$$[\overline{M}_x]\{\overline{q}_x\} = \{\overline{f}_x\} - [\overline{L}_x]\{\overline{p}\} \tag{11.13a}$$

$$[\overline{M}_z]\{\overline{q}_z\} = \{\overline{f}_z\} - [\overline{L}_z]\{\overline{p}\} \tag{11.13b}$$

The sets of equations (11.12) and (11.13) represent the final numerical approximation of the fluid continuity and Darcy velocity equations. The solution process for these equations is sequential and starts by solving equation (11.12) for pressure and then poceeding to construct the right-hand sides of equations (11.13) and solving these equations for velocities. The velocity values will be used in the numerical approximation of the solute-transport equation which is the subject of the next section.

11.2.2 Solute-transport Equation

The standard Galerkin finite-element approach is used for solution of the solute-transport equation (11.3). As mentioned before, at this stage of the solution process, the Darcy velocity components, q_x and q_z, are given from the solution of the ground-water flow equations. The values of velocities are used beforehand to determine the velocity-dependent components of the Dispersion coefficient tensor, D_{ij}, using the relationships (11.5). The advective-transport term in equation (11.3) is also dependent on the velocities, but this dependence is directly included in the subsequent numerical formulations.

Following an approach analogous to the previous section, we approximate the unknown solute concentration in terms of a trial solution of the form:

$$c \simeq \sum_{j=1}^{n} c_j(t)\, \phi_j(x,z) \qquad (11.14)$$

where c_j's represent the unknown nodal concentrations and ϕ_j's are the basis functions that are selected as a matter of simplicity to be the same as the basis functions used for representation of velocity. The known components of Dispersion coefficient can also be expressed in the form of finite series, for example:

$$D_{xx} \simeq \sum_{j=1}^{n} D_{xxj}(t)\,\phi_j(t) \qquad (11.15)$$

where D_{xxj}'s are the nodal Dispersion values. Similar expressions can be written for D_{zz}, D_{xz} and D_{zx}. Note that the aquifer porosity, θ , is a constant.

The differential operator of the solute-transport equation (11.3) is written in its expanded form as

$$L(c) = \frac{\partial}{\partial x}(D_{xx}\frac{\partial c}{\partial x}) + \frac{\partial}{\partial x}(D_{xz}\frac{\partial c}{\partial z}) + \frac{\partial}{\partial z}(D_{zx}\frac{\partial c}{\partial x}) + \frac{\partial}{\partial z}(D_{zz}\frac{\partial c}{\partial z})$$

$$- \frac{\partial}{\partial x}(v_x c) - \frac{\partial}{\partial z}(v_z c) - \frac{\partial c}{\partial t} = 0 \qquad (11.16)$$

where $v_x = q_x/\theta$ and $v_z = q_z/\theta$ are pore velocities.

Utilizing the Galerkin approach, the approximate integral equations are obtained by making the residual arising from substitution of equation (11.14) into (11.16) orthogonal to each of the basis functions, ϕ_j . A set of ordinary differential equations will eventually result from this operation which in matrix form, is expressed as

$$[R]\,\{c\} + [T]\,\{\frac{dc}{dt}\} = [F] \qquad (11.17)$$

where R(n*n) is the advective-dispersive transport matrix T(n*n) is the solute-mass matrix and F(n*1) contains the dispersive-mass fluxes at the boundary. The typical elements of R, T and F are defined by

$$R(i,j) = \sum_{k=1}^{n} \int_{\Omega}\int \{D_{xxk}\, \phi_k \frac{\partial \phi_j}{\partial x} \frac{\partial \phi_i}{\partial x} + D_{xzk}\, \phi_k \frac{\partial \phi_j}{\partial x} \frac{\partial \phi_i}{\partial z}$$

$$+ D_{zxk}\, \phi_k \frac{\partial \phi_j}{\partial z} \frac{\partial \phi_i}{\partial x} + D_{zzk}\, \phi_k \frac{\partial \phi_j}{\partial z} \frac{\partial \phi_i}{\partial x} + v_{xk}\, \phi_k \frac{\partial \phi_j}{\partial x}\, \phi_i$$

$$+ v_{zk}\, \phi_x \frac{\partial \phi_j}{\partial z}\, \phi_i\}\; d\,\Omega \qquad (11.18a)$$

$$T(i,j) = \int_{\Omega}\int \phi_j\, \phi_i\; d\,\Omega \qquad (11.18b)$$

$$F(i) = \int_{\Gamma} (D \frac{\partial c}{\partial n})\, \phi_i d\,\Gamma \qquad (11.18c)$$

In formulating these equations, Green's theorem is applied to break up the second derivatives. Moreover, the components of the flux-derivatives resulting from expansion of the advective terms in equation (11.16) were assumed to be negligible and, therefore, were eliminated during the development of the approximate equations. This assumption is acceptable in the absence of fluid sources and sinks (Frind, 1982a). Note also that the boundary-flux term, equation (11.18c), is non-zero only at an inflow boundary in which case it is evaluated with the use of equation (11.8b).

We can now proceed to solve the set of ordinary differential equations (11.17) by finite-difference time stepping. Employing a finite-difference approximation of the temporal derivatives, equation (11.17) can be written in a time-weighted form as

$$[P]\,\{c\}_{t\,+\,\Delta t} = [S]\,\{c\}_t + \{G\} \qquad (11.19)$$

where the coefficient matrices P and S and the vector G are given by

$$[P] = \varepsilon[R] + \frac{1}{\Delta t}[T] \tag{11.20a}$$

$$[S] = -(1-\varepsilon)[R] + \frac{1}{\Delta t}[T] \tag{11.20b}$$

$$\{G\} = \varepsilon\{F\}_{t+\Delta t} + (1-\varepsilon)\{F\}_t \tag{11.20c}$$

in which $1/2 \leq \varepsilon \leq 1$ is the time-weighting factor, and Δt represents the time interval. A value of $\varepsilon = 1/2$ results in the Crank-Nicolson approximation which is second order accurate in time. This choice is known, however, to occasionally produce oscillatory solutions. On the other hand, a value $\varepsilon=1$ (implicit scheme) provides good stability but may result in greater smearing of the solute distribution. Depending on the problem being analyzed, an appropriate choice of ε can usually be obtained within a few trials.

Starting from some initial values, equation (11.19) will determine the transient variations in solute concentration. For advective-dominated transport problems, numerical difficulties in the form of artificial dispersion and overshooting may be encountered. An improved estimate of velocities as obtained in this study may alleviate some of these difficulties. Mesh refinement is known to reduce the tendency of overshooting. The upstream-weighted technique presented by Huyakorn and Nilkuha (1979) is another way of avoiding numerical dispersions but at the expense of smearing the concentration front.

11.3 Solution Strategy and Computational Framework

Because of the nonlinearity involved, equations (11.1), (11.2) and (11.3) or their numerical approximations, equations (11.12), (11.13) and (11.19), have to be solved in combination with equation (11.4) in an iterative manner. The solution procedure for each time step begins with an estimate of fluid density obtained from equation (11.4) using the concentration distribution from the previous time step. The coefficients in the equations for pressure and velocity, equations (11.12) and (11.13), are determined on the basis of this estimate of fluid density and then equations (11.12) and (11.13) are solved in a sequential approach. The nodal values of velocities obtained from solution of equation (11.13) are used to define the advective and dispersive components in equation (11.19). Subsequently, equation (11.19) is solved to yield the salt-concentration distribution. Without advancing in time, the fluid densities are updated using the new estimate of concentration in equation (11.4), and the whole cycle is repeated once more. This process continues until the successive concentration values are within a specified tolerance. At this stage we can proceed to perform the computations for the next time step.

The iterative process described above usually converges rather rapidly, provided the time interval is not too large. According to Frind (1982a), the choice of an appropriate time interval is controlled in most problems by the need to keep the numerical dispersion to an acceptable level rather than the convergence criteria. A time-lagged approach suggested by Segol et al. (1975) has also been shown to be very effective for long-term transient simulation of problems with densities lower than that of sea water. In this case, the elapsed time between solutions of the flow equations is much larger than the time interval for computation of solute concentration.

During the course of model development, care must be taken in reducing the computer-storage requirement and in increasing the computational efficiency. Considerable saving was achieved in our model by storing the computed values of the elemental-basis functions and their derivatives at the Gaussian points on an input/output file. Consequently future reference to these values was obtained rather easily without the need to repeat any computation. The model takes full advantage of the specific structure of the coefficient matrices. For matrices $\bar{M}_x$ and $\bar{M}_z$ in equation (11.13) that are banded and symmetric, only the elements within the upper band-width are stored. The banded portions of the non-symmetric matrices $\bar{K}_x$, $\bar{K}_z$, $\bar{L}_x$, $\bar{L}_2$, P and S are retained in rectangular two-dimensional arrays. The construction of coefficient matrices in equations (11.12) and (11.13), i.e. A, $\bar{M}_x$ and $\bar{M}_z$, are needed only once. At each time step only the right-hand-side vectors of these equations have to be updated. The coefficient matrix in equation (11.19), i.e. P, is reconstructed whenever the time interval, Δt, changes or the velocities are updated. Solution of the equations are carried out efficiently using a Gauss solver for equation (11.12), a Cholesky solver for equation (11.13) and a Gaussian routine for non-symmetric coefficient matrices in equation (11.19).

11.4 Numerical Results

A computer model was developed on the basis of the formulation presented in this study. Here we demonstrate the usefulness of this model for simulation of variable-density flow problems.

The analytic solution to the example problem devised by Henry (1964) is usually used as a benchmark against which other solutions are compared. The problem involves the intrusion of saltwater into a confined coastal aquifer. The configuration of the vertical cross section of this aquifer is depicted in Figure 11.1. Inland freshwater recharges the aquifer from the left boundary while as the same time the denser sea water is moving inland from under the freshwater. At equilibrium a dispersive zone develops at the contact of the two fluids through which the mixed water circulates and returns back to the sea.

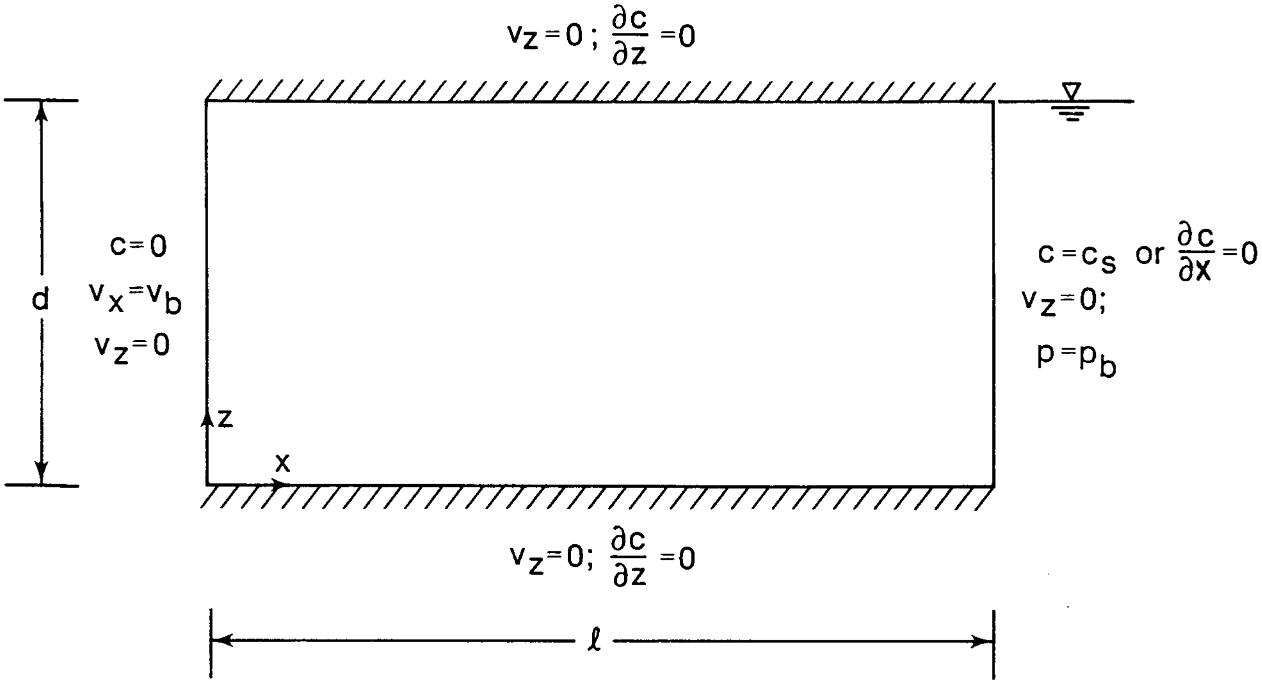

Figure 11.1 Schematic representation of the Henry's example.

The aquifer is assumed to be homogeneous and isotropic. The dispersion coefficient is assumed constant although, in reality, it changes with variations in velocity. Initially, the aquifer is occupied only with freshwater. The prescribed flux and prescribed pressure-boundary conditions are assumed, respectively, along the left and right vertical boundaries. The upper and lower boundaries are impermeable. The hydrogeologic parameters associated with this problem are as follows

aquifer porosity	$\theta = 0.35$
hydraulic permeability	$k = 1.020408 \text{ X } 10^{-9} \text{ m}^2$
fluid viscosity	$\mu = 10^{-3}$ Kg/(m.sec)
Dispersion coefficient	$D = 6.6 \text{ X } 10^{-10} \text{ m}^2/\text{sec}$
left-boundary influx velocity	$\upsilon = 6.6 \text{ X } 10^{-5}/0.35 = 1.885 \text{ X } 10^{-4}$
right-boundary pressure distribution	$p_b = \rho_x g$ (depth)
sea-water density	$\rho_s = 1\text{-}25 \text{ Kg/m}^3$
freshwater density	$\rho_f = 1000 \text{ Kg/m}^3$
sea-water salt concentration	$c_s = 35 \text{ K}_g$ (dissolved solids)/K_g (sea water)
acceleration of gravity	$g = 9.8 \text{ m/sec}^2$
rate of density change w/concentration	$\frac{\partial\rho}{\partial c} = 700 \frac{\text{K}_{g(\text{sea water})}^2}{\text{K}_g(\text{TDS}) \quad \text{m}^3}$
aquifer thickness	$d = 1.0$ m
aquifer length	$\ell = 2.0$ m

During the course of numerical experiments, approximations of pressure, p; velocity, v; and salt concentration, c, were obtained over the aquifer domain using three types of interpolation scheme: (1) linear interpolations for p, v and c (Figure 11.2-a); (2) quadratic interpolations for p, v and c (Figure 11.2-b); and (3) mixed interpolations, i.e. quadratic interpolations for v and c (Figure 11.2-b) and linear interpolation for p (using corner nodes in Figure 11.2-b). The mixed interpolation scheme, as indicated before, is consistent with the form of the governing equations and is expected to provide the most accurate solution among the three schemes.

The first analysis was performed to check the accuracy of the model results using only the mixed interpolation scheme. The computed 0.5 isochlor is displayed in Figure 11.3 with the similar contour lines from the steady-state solution of Henry (1964) and the transient solution of Segol et al. (1975). The comparison of our transient solutions for the elapsed time of 30 and 100 minutes with the solutions obtained by Segol et al. (1975) is excellent (see Figure 11.3). For the most part, the two sets of isochlors are located in close proximity to each other. One interesting observation is that due to the existence of incorrect vertical velocities along the right boundary in the Segol et al. formulation, the top portion of the dispersive zone tends to be narrow and the tip of the saltwater zone calculated by their model always stays higher than that determined by our model. This difficulty was removed in our analysis by explicitly setting these velocities to zero.

To obtain the steady-state solution, the simulation time was extended to 500 minutes. After the elapsed time of 200 minutes, the top portion of the dispersive zone remained relatively stable while the bottom portion moved only slightly. The 0.5-isochlor line for the 200-minute .time period shown in Figure 11.3 can be considered to be representative of the quasi-steady-state

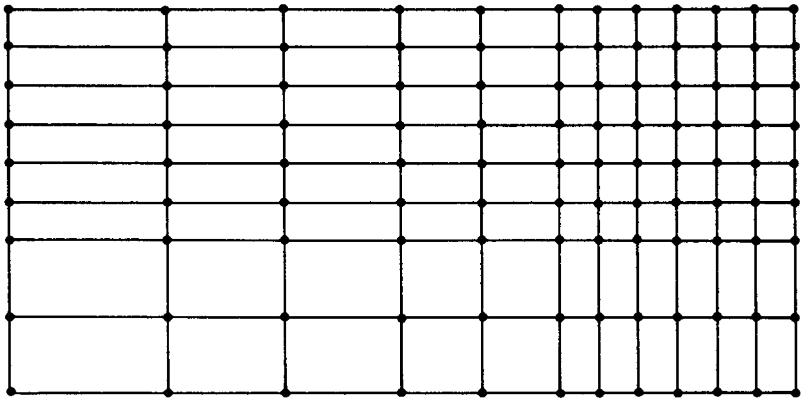

(a) linear elements

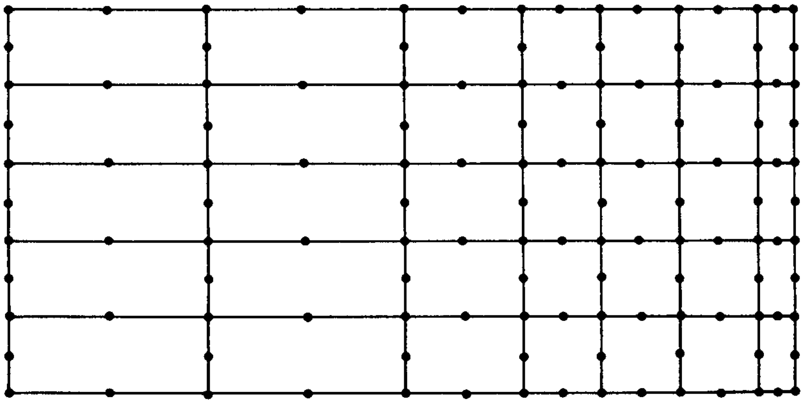

(b) quadratic elements

Figure 11.2 Finite-element discretization of the aquifer domain for the Henry's problem.

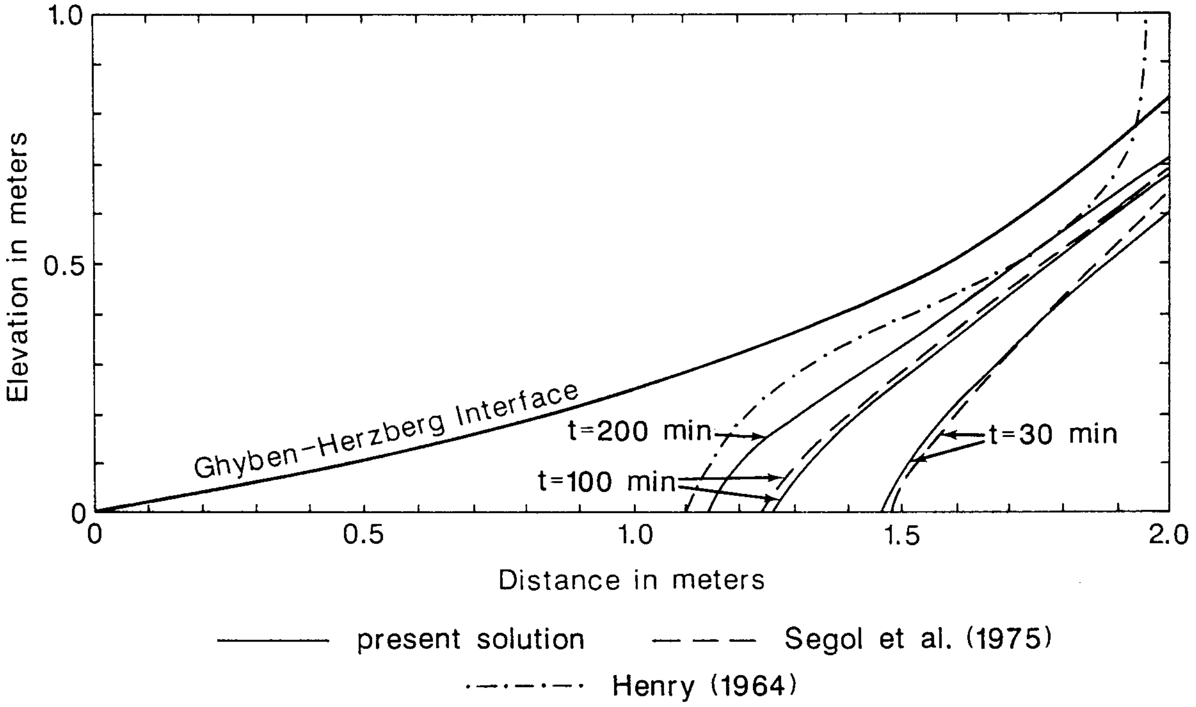

Figure 11.3 The comparison of 0.5 isochlors computed by the present model using mixed interpolations with several available solutions.

solution of Henry's problems. Again the agreement between Henry's solution and the model results is reasonably good.

Figure 11.3 also depicts the Ghyben-Herzberg interface obtained based on the assumption of immiscible-fluid flows (Frind, 1982a). An important observation is the extensive location of the saltwater toe which obviously overestimates reality by as far as twice the actual distance. This is a good indication of inappropriateness of sharp-interface models for situations characterized by significant dispersion. This point is clarified even further in Figure 11.4 where the whole spectrum of the dispersive zone is demonstrated for the elapsed time of 200 minutes. Note again the large extent of the top portion of the dispersive zone created by removal of artificial vertical velocities.

To gain insight into the hydrodynamics of the flow in a density-dependent system, the nodal velocities were plotted in Figure 11.5 for three different time periods. As seen in Figure 11.5, the vertical components of velocities within the saltwater-freshwater mixing zone were affected significantly by the variations in density. The changes in velocities become less important during latter time steps. In most problems, after reaching a certain quasi-stabilization point in time, the changes in vertical velocities are minimal and in fact the calculation of velocities can be carried out much less frequently than that of salt concentration. In our analysis we updated the velocities at all time steps although it could have been avoided. The velocity vectors demonstrate clearly the whole circulation process of the saltwater-intrusion phenomenon.

The last experiment involved using all three different interpolation schemes for solution of Henry's problem. The 0.2 and 0.5 isochlors obtained for the elapsed time of 100 minutes are depicted in Figure 11.6. The top of

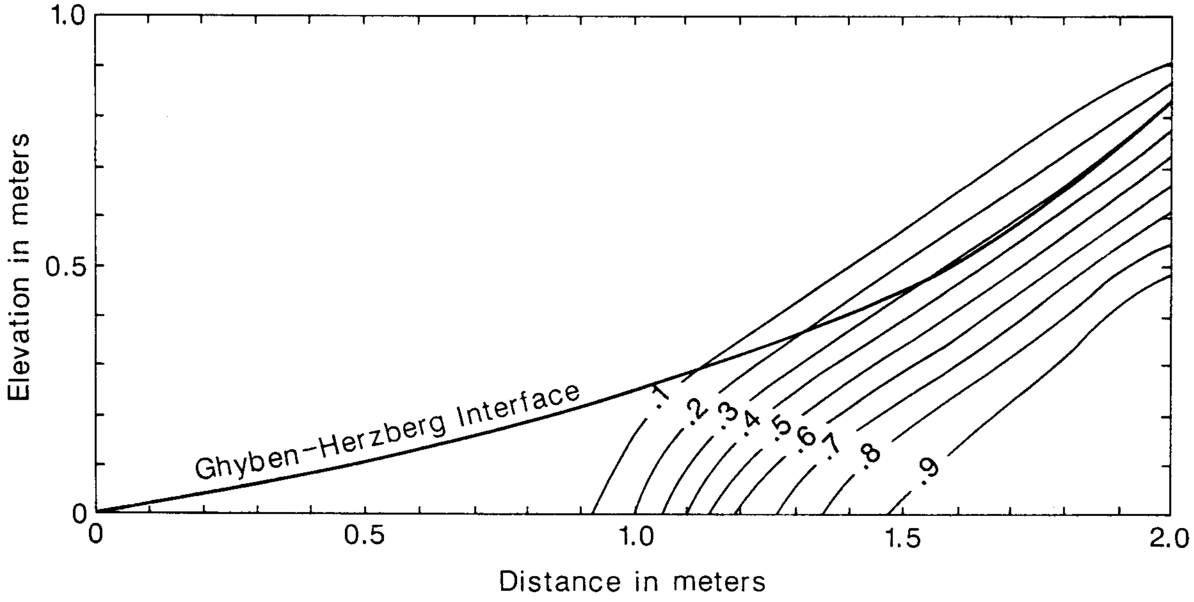

Figure 11.4 Set of isochlors at the elapsed time of 200 min resulted from the use of mixed interpolations.

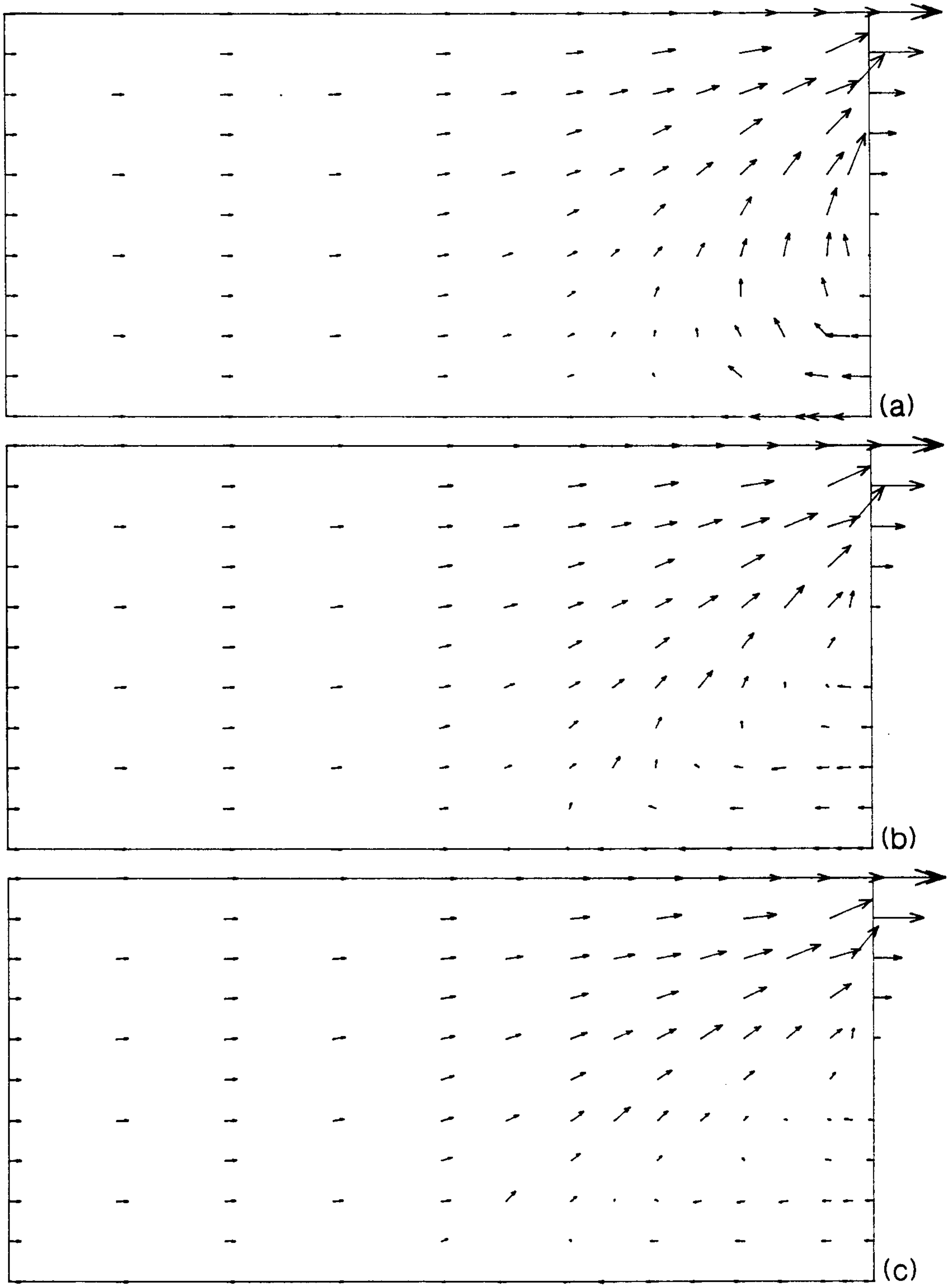

Figure 11.5 Velocity field at different times resulted from the use of mixed interpolations; (a) elapsed time = 5 min., (b) elapsed time = 30 min. and (c) elapsed time = 100 min.

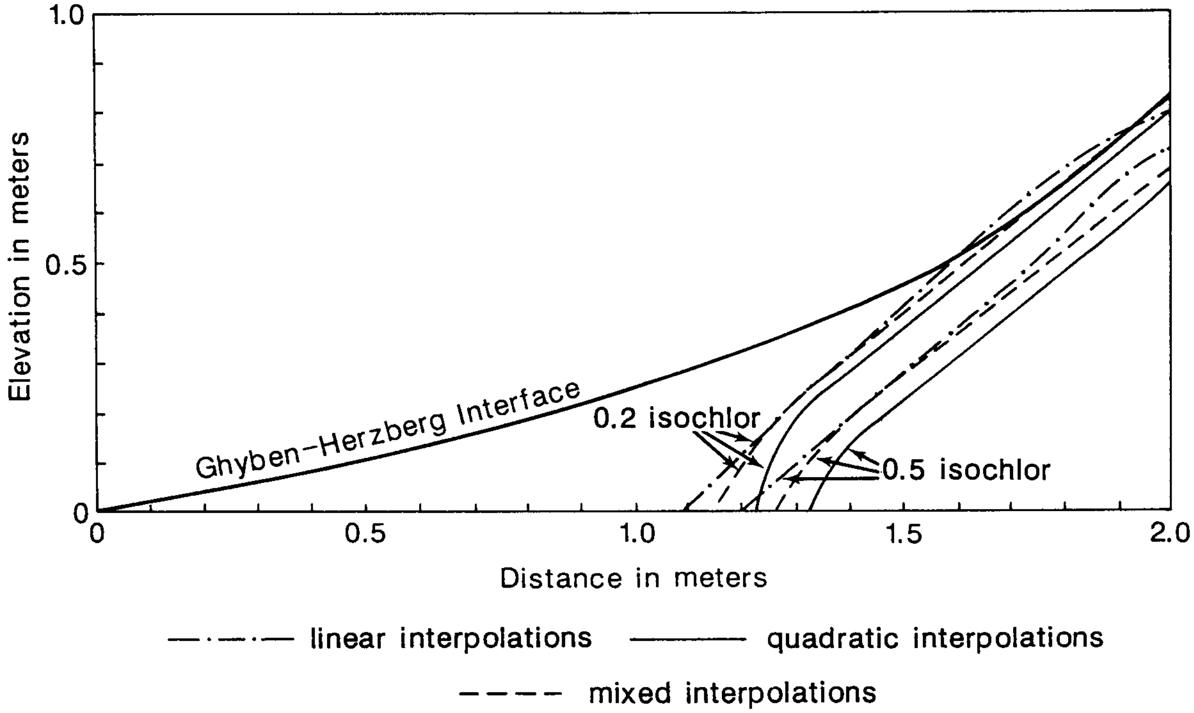

Figure 11.6 Comparison of concentration profiles resulted from the use of different interpolation schemes.

the isochlor from the linear-interpolation scheme is extended further inland while that from the quadratic-interpolation scheme is sharper and shorter. The isochlors calculated with mixed interpolations are smooth and for the most part are located in between the two other sets of solutions.

11.6 Summary and Conclusions

A finite-element model was developed for sequential solution of the fluid continuity, Darcy velocity and solute-transport equations. The model, while preserving the continuity of the velocity field, results in accurate estimates of model velocities which are very important in the analysis of advective-dominated transport problems. Several other features of the model such as the storage of basis functions and their derivatives at Gaussian points on an input-output file have improved the efficiency of the computations substantially.

Applied to the Henry's sea-water intrusion problem, the model was shown to reach a state of dynamic equilibrium with minimal computational efforts. The model is designed specifically for simulation of saltwater intrusion under the miscible-flow environments. Application of the model to the field problems with limited available data may encounter difficulty mainly because of the lack of sufficient information and also because of the poorly defined transport theory in complex hydrogeologic systems.

APPENDIX A
Chemical-quality Data

Log #	Cl (ppm)	TDS (ppm)	Site	Collection Data
84502	66,390	119,567	C-2	9/6/84
84503	56,150	102,408	C-3	9/6/84
84504	4,995	9,161	C-4	9/6/84
84505	17,410	34,600	D-3	9/6/84
84506	2,042	4,156	D-4	9/6/84
84507	60,930	110,740	D-1	9/4/86
84508	1,531	3,273	F-2	9/6/84
84509	62,880	112,774	F-1	9/6/84
84517	219	996	F-4	9/12/84
84518	14,680	27,853	G-1	9/12/84
84519	1,108	2,496	G-3	9/12/84
84520	7,126	13,343	H-1	9/12/84
84521	737	1,854	H-2	9/12/84
84527	67,260	120,740	Permian Well	9/12/84
84527	67,260	120,740	Permian Well	9/13/84
85019	67,560	118,880	A-1	3/15/85
85020	66,640	118,850	A-2	3/15/85
85021	56,200	99,670	A-3	3/15/85
85022	63,990	114,750	A-4	3/15/85
85023	35,420	63,220	A-5	3/15/85
85024	54,760	97,510	B-1	3/15/85
85025	61,930	110,520	C-1	3/15/85
85026	66,980	118,330	C-2	3/15/85
85027	58,540	102,880	C-3	3/15/85
85028	4,002	7,860	C-4	3/15/85
85029	65,940	118,520	D-1	3/15/85
85030	21,820	39,690	D-3	3/15/85
85031	2,318	4,573	D-4	3/15/85
85032	1,248	2,717	E-1	3/15/85
85033	405	1,318	E-2	3/15/85
85034	2,543	4,896	E-3	3/15/85
85035	67,100	118,530	E-4	3/15/85
85036	64,100	45,070	F-1	3/15/85
85037	1,216	2,633	F-2	3/15/85
85038	54,100	96,950	F-3	3/15/85
85039	298	1,094	F-4	3/15/85
85040	17,920	32,357	G-1	3/15/85
85041	499	1,430	G-3	3/15/85
85042	10,290	18,713	G-4	3/15/85
85043	7,955	14,980	H-1	3/15/85
85044	597	1,532	H-2	3/15/85
85045	3,495	6,907	H-3	3/15/85
85046	6,193	11,713	I-1	3/15/85
85047	1,102	2,382	I-2	3/15/85

APPENDIX A
Chemical-quality Data

85048	4,973	9,667	J-1	3/15/85
85049	3,607	6,997	J-2	3/15/85
85050	1,526	3,067	J-3	3/15/85
85051	51,800	93,460	K-1	3/15/85
85052	504	1,432	K-2	3/15/85
85053	66,640	120,360	K-3	3/15/85
85054	207	1,104	K-4	3/15/85
85246	64,320	119,020	A-1	7/22/85
85247	66,920	120,120	A-2	7/22/85
85248	56,880	102,850	A-3	7/22/85
85249	65,790	115,400	A-4	7/22/85
85250	41,070	74,860	A-5	7/22/85
85251	58,523	106,050	B-1	7/24/85
85252	64,990	119,240	B-2	7/24/85
85253	60,180	107,650	B-3	7/24/85
85254	10,900	20,130	B-4	7/24/85
85255	62,520	116,770	C-1	7/17/85
85256	64,880	119,510	C-2	7/16/85
85257	52,660	95,850	C-3	7/16/85
85258	3,835	7,287	C-4	7/16/85
85259	58,080	104,360	C-5	7/15/85
85260	63,870	117,890	D-1	7/17/85
85261	61,620	108,920	D-2	7/17/85
85262	18,190	32,310	D-3	7/16/85
85263	2,212	4,419	D-4	7/16/85
85264	65,790	119,100	D-5	7/16/85
85284	4,830	9,303	J-1	7/26/85
85285	3,374	6,883	J-2	7/26/85
85286	1,605	3,240	J-3	7/26/85
85287	52,010	91,680	K-1	7/18/85
85288	1,264	2,709	K-2	7/18/85
85289	68,980	120,350	K-3	7/18/85
85290	1,976	4,026	K-4	7/18/85
85291	35,010	61,900	L-1	7/26/85
85292	4,003	7,813	L-2	7/26/85
85293	714	1,716	L-3	7/26/85
85294	62,520	111,490	L-4	7/26/85
85295	59,850	105,570	M-2	7/22/85
85296	63,520	114,400	M-2	7/24/86
85297	42,480	77,640	M-3	7/24/85
85298	62,010	116,980	M-5	7/15/85
85299	64,910	117,660	M-5	7/24/86
85300	4,025	7,903	MP-1	7/17/85
85301	4,526	8,780	MP-3	7/17/86
85265	66,580	118,220	D-5	7/17/85
85266	11,460	21,293	D-6	7/17/85
85267	2,151	4,282	E-1	7/18/85
85268	1,471	3,152	E-2	7/18/85
85269	2,510	4,910	E-3	7/17/85
85270	66,580	119,380	E-4	7/17/85

APPENDIX A
Chemical-quality Data

85271	65,450	115,840	F-1	7/19/85
85272	1,588	3,325	F-2	7/19/85
85273	59,830	106,940	F-3	7/19/85
85274	672	1,543	F-4	7/19/85
85275	21,150	37,100	G-1	7/19/85
85276	20,680	36,710	G-1	7/29/85
85277	579	1,524	G-3	7/29/85
85278	50,840	89,920	G-4	7/29/85
85279	7,540	13,847	H-1	7/25/85
85280	638	1,558	H-2	7/25/85
85281	5,503	10,153	H-3	7/25/85
85282	5,384	10,063	I-1	7/25/85
85283	1,042	2,284	I-2	7/25/85
85418	65,400	118,720	A-1	11/12/85
85419	64,250	116,000	A-2	11/12/85
85420	46,760	83,840	A-3	11/12/85
85421	43,700	77,410	A-5	11/12/85
85422	66,320	117,490	B-2	11/13/85
85423	54,130	96,750	B-3	11/13/85
85424	7,338	14,283	B-4	11/13/85
85425	66,670	119,710	C-2	11/13/85
85426	49,770	87,460	C-3	11/13/85
85427	3,287	6,533	C-4	11/13/85
85428	61,730	113,340	C-5	11/13/85
85429	65,170	119,420	D-1	11/13/85
85430	7,643	14,297	D-3	11/13/85
85431	1,856	3,777	D-4	11/13/85
85432	64,560	117,000	D-5	11/13/85
85433	3,608	6,827	D-6	11/13/85
85434	237	908	E-2	11/13/85
85435	1,217	2,650	E-3	11/13/85
85436	54,020	98,170	E-4	11/13/85
85437	65,280	118,320	F-1	11/13/85
85438	762	1,806	F-2	11/13/85
85439	101	567	F-4	11/13/85
85440	15,250	27,610	G-1	11/13/85
85441	470	1,289	G-3	11/13/85
85442	7,399	13,667	H-1	11/13/85
85443	677	1,665	H-2	11/13/85
85444	15	589	H-4	11/13/85
85445	4,068	7,600	I-1	11/13/85
85446	904	2,083	I-2	11/13/85
85447	64,480	114,700	M-2	11/12/85
85448	38,930	70,540	M-3	11/12/85
85449	2,537	5,062	M-4	11/12/85
85450	59,470	106,370	M-5	11/12/85
85462	89	596	K-2	11/20/85
85463	65,520	118,840	K-3	11/12/85
85464	64	436	K-4	11/12/85

APPENDIX B
Description of the Geologic Units at the Field Cross Section

Pleistocene alluvium, approximately 60 feet thick, unconformably overlies the Wellington Formation throughout the study area. The alluvium consists of gravel, sand, silt, and clay deposits in a fining-upwards sequence of five interbedded lithofacies. Irregularities in the contact between the alluvium and the Wellington (see Figure 6.1) are the results of dissolution and collapse of the underlying gypsum layers in the Wellington Formation (Gillespie and Hargadine, 1981). Following is a description of these five units.

Unit 1: Fine sand and silt lithofacies. This lithofacies ranges in thickness from 1 to 8 feet and occurs as discontinuous thin layers and pods of fine-grained quartz sand and silt. Locally, lenses of medium-grained quartz sand are present.

Unit 2: Silt and clay lithofacies. The silt and clay lithofacies underlie nearly all of the land surface in the study area and occurs in 1- to 8-feet-thick discontinuous layers. It is characterized by variable proportions of brown to light-brown silt, clay, and carbonized plant debris with interspersed lenses of medium sand. One of these layers spans much of the study area and can be identified in the subsurface by its gray color and the presence of carbonized plant debris near its base. This lithofacies is easily recognized on gamma-ray logs because of its high organic content.

Unit 3: Fine- to medium-grained sand lithofacies. This unit is present in the subsurface throughout the study area and usually occurs beneath the silt and clay lithofacies. The mud and gamma-ray logs show that the upper boundary with unit 2 is gradational but the lower boundary is quite sharp. This unit is interbedded with the silt and clay lithofacies in the western part of the study area. The sand is arkosic and locally is coarse grained with pea-size gravel especially near the base of the unit. Thickness ranges from featheredge to 11 feet.

Unit 4: Medium- to coarse-grained sand and gravel lithofacies. This lithofacies ranges in thickness from 10 feet beneath the west side of the study area near well site I to approximately 30 feet beneath the east side of the study area at well site B. The sand-sized fraction consists of medium- to coarse-grained arkosic sand. Gravel consists of subangular to subrounded clasts ranging in size from pebbles to small cobbles. Clast composition is arkosic and includes fragments of Lower Cretaceous sandstones and Upper Cretaceous limestones. Locally, the sand and gravel are cemented together with calcite cement near the base of the alluvium and possibly in cracks and fissures in the underlying Wellington Formation.

Unit 5: Sand and gravel with clay-silt lenses and matrix. This lithofacies is largely the same as the medium- to coarse-grained sand and gravel lithofacies, but it contains much larger amounts of silt and clay in the matrix and as discrete lenses. It is best developed west of the river beneath sites E, K and F where it attains a thickness of 6 to 8 feet and it is easily identifiable on gamma-ray logs from sites A and K.

The lower member of the Wellington Formation overlies the Herrington Member and consists of brown to olive-green and gray dolomitic mudstone with abundant gypsum and dolomite (Unit 6 in Figure 6.1). Fractures and small solution cavities are probably filled with gypsum and some calcite. Calcite-cemented sand and gravel are known to fill many of the fractures in the mudstone (Gillespie, personal communication, 1985). Individual fracture fills were traced on outcrop exposures of the Wellington Formation near Abilene for several feet vertically and horizontally. Near the contact with the overlying alluvial deposits, the Wellington is highly weathered and is more of an olive-gray color.

Within the lower member of the Wellington Formation, gamma-ray logs indicate the presence of a 2- 6-foot-thick layer of gypsum or gypsum with shale intercalations (Unit 7 in Figure 6.1). Although no core material was recovered from this interval, drilling mud logs for the test-holes drilled for piezometers M-5 and A-1 indicate that small clumps of gypsum were observed in the drill cuttings. Some loss of circulation during drilling was noted at approximately this level, but it is not known if fluid passed into solution cavities in the gypsum layer, into fractures in the surrounding mudstone or into the overlying alluvium since the hole was not cased.

The Herrington Member of the Nolans Limestone consists of yellow to gray gypsiferous cryptalgal dolomitic limestone with interbedded layers of bivalve and brachiopod packstone (unit 8 on Figure 6.1). Dissolution of original shell material within the bivalve packstone has created zones of high porosity. Fracture and solution cavities are also present in the core samples. The fractures are oriented in a near-vertical direction whereas the solution cavities tend to be oriented horizontally. Some of the moldic porosity fractures and solution cavities have been filled by gypsum precipitation, virtually occluding all porosity.

REFERENCES

Badon-Ghyben, W., 1888, Nota in Verband met de Voorgenomen Putboring Nabij Amserdam (Notes on the probable results of well drilling near Amsterdam): The Hague, Netherlands, Tijdschr. Kon. Inst. Ing.

Bear, J., 1979, Hydraulics of groundwater: New York, McGraw-Hill, 569pp.

Bear, J., and Dagan, G., 1964, Moving interface in coastal aquifers: A.S.C.E., Journal of Hydraul. Division, HY4, p. 193-216.

Bear, J., and Kapuler, II., 1981, A numerical solution for the movement of an interface in a layered coastal aquifer: Journal of Hydrology, 50, p. 273-298.

Benz, L. C., Mickelson, R. H., Sandoval, F. M., and Carlson, C. W., 1961, Ground-water investigations in a saline area of the Red River valley, North Dakota: J. Geophys. Res., 66(8), p. 2435-2443.

Cedergren, H. R., 1967, Seepage, drainage, and flow nets: John Wiley and Sons, New York, 534p.

Cobb, P. C., 1980, The distribution and mechanisms of saltwater intrusion in the freshwater aquifer and in Rattlesnake Creek, Stafford County, Kansas: Unpublished M.S. thesis, University of Kansas, 176 pp.

Cooper, H. H., Jr., 1959, A hypothesis concerning the dynamic balance of freshwater and saltwater in a coastal aquifer: Jour. Geophys. Research, 64(4), p. 461-467.

Cooper, H. H., Jr., Kohout, F. A., Henry, H. R., and Glover, R. E., 1964, Sea water in coastal aquifers: U.S. Geological Survey Water-Supply Paper 1613-C, Washington, D.C.

Dagan, G., and Bear, J., 1968, Solving the problem of local interface upconing in a coastal aquifer by the method of small perturbations: Journal of Hydraulic Resarch, 6(1), p. 15-44.

Doveton, J. H., 1986, Log analysis of subsurface geology, concepts and computer methods: Wiley Interscience, New York, 273 pp.

Freeze, R. A. and Cherry, J. A., 1979, Groundwater: Prentice Hall Inc., Englewood Cliffs, New Jersey, 604 pp.

Frind, E. O., 1982a, Simulation of long-term transient density-dependent transport in groundwater: Advances in Water Resources, 5(1), p. 73-88.

Frind, E. O., 1982b, Sea-water intrusion in continuous coastal aquifer-aquitard systems: Advances in Water Resources, 5(1), p. 89-97.

Gillespie, J. B., and Hargadine, G. D., 1981, Saline groundwater discharge to the Smoky Hill River between Salina and Abilene, central Kansas: U.S. Geological Survey, Water-Resources Investigations 81-43, 71pp.

Gogel, T., 1981, Discharge of saltwater from Permian rocks to major stream-aquifer systems in central Kansas; Kansas Geological Survey, Chemical Quality Series 9, 60pp.

Herzberg, A., 1901, Die Wasserversorgung einigen Nordeseebaden (The water supply on parts of the North Sea coast in Germany): Z. Basbelencht, Wasserversorg, p. 44.

Hubbert, M. K., 1940. The theory of ground-water motion: J. Geology, 48(8), part 1, p. 785-944.

Huyakorn, P. S., and Nilkuha, K. 1979, Solution of transient transport equation using an upstream finite element scheme: Applied Mathematical Modeling, v. 3, p. 7-17.

Huisman, L., 1972, Groundwater Recover, Winchester Press, New York.

Huyakorn, P.S., and Taylor, C. 1976, Finite element models for coupled groundwater flow and convective dispersion: Proc. 1st Int. Conf. on Finite Elements in Water Resources, Princeton University, Princeton, New Jersey, p. 1.131-1.151.

Hvorslev, M. J., 1951, Time lag and soil permeability in groundwater observations: U.S. Army Corps of Engineers, Waterways Experiment Station, Bulletin 36.

INTERA, 1976, A model for calculating effects of liquid waste disposal in deep saline aquifer: U.S. Geological Survey, Water-Resources Investigation, 76-61, 253 pp.

Kawatani, T., 1980, Behavior of seawater intrusion in layered coastal aquifers: Proceedings of the Third International Conference on Finite Elements in Water Resources, University of Mississippi, U.S.A.

Kemblowski, M. A., 1985, Saltwater-freshwater transient upconing - an implicit boundary-element solution: J. Hydrol., 78, p.35-47.

Kemblowski, M. A., in edit, The impact of the Dupuit-Forchheimer approximation on saltwater intrusion simulation: Submitted to Ground Water.

Kohout, F. A., 1960, Cyclic flow of saltwater in the Biscayne aquifer of southeastern Florida: J. Geophys. Res., 64(4), p.461-167.

Kohout, F. A., 1980, Differing positions of saline interfaces in aquifers and observation boreholes-comments: J. Hydrol., 48, p.191-195.

Kovar, K., 1980, Calculation of the regional variation of the saline-fresh groundwater interface by means of the finite element method: The Netherlands, National Institute for Water Supply.

Latta, B. F., 1949, Ground-water conditions in the Smoky Hill Valley in Saline, Dickenson, and Geary Counties, Kansas: Kansas Geological Survey, Bulletin 84, 152pp.

Lazrey, H., 1972, Application of surface resistivity methods to the detection of salt-water intrusion in Shippegan, New Brunswick: CIM Transactions, 75, 3.

Lee, D. R., 1977, A device for measuring seepage flux in lakes and estuaries: Limnol. Oceanogr., 22(1), p.140-147

Lee, C-H., and Cheng, R. T-S., 1974, On seawater encroachment in coastal aquifers: Water Resources Research, 10(5), p. 1039-1043.

Lee, D. R., and Cherry, J. A., 1978, A field exercise on groundwater flow using seepage meters and minipiezometers, J. Geol. Educ.

Liggett, J. A., 1977, Location of free surface in porous media: Journal of Hydraulics, Div. Amer. Soc. Civil Eng. 103(HY4), p.353-365.

Liggett, J. A. and Liu, P.L-F., 1983, The Boundary Integral Equation Method for porous media flow: George Allen & Unwin, London.

Lusczynski, N. J., 1961, Head and flow of groundwater variable density: J. Geophys. Res., 66(12), p.4247-4256.

Macfarlane, P. A. and Ackerman, J., 1983, The detection of natural brines by vertical electrical soundings in the Great Bend Prairie, south-central Kansas: Kansas Geological Survey, Open-File Report 83-6, 24pp.

Macfarlane, P. A., Kemblowski, M. W., Costanzo, G. V., and Sadeghipour, J., 1986, On the use of pressure differential measurements to map chemical-quality variations in a variable-density ground water system: Proceedings and Ground Water Monitoring, Columbus, Ohio.

McElwee, C. D., 1985, A model study of saltwater intrusion to a river using the sharp interface approximation: Ground Water, 23(4), p.465-475.

McElwee, C. D., and Macfarlane, P. A., 1980, Notes on the determination of flow between wells in variable-density confined systems: Unpublished, Kansas Geological Survey.

McElwee, C. D., Severini, T., Cobb, P., Fleming, A., Paschetto, J., Butt, M. A., and Watson, P., 1981, A study of the saltwater intrusion problem between Salina, Kansas, and Solomon, Kansas, in the Smoky Hill River valley: Kansas Geological Survey, Open File Report 81-3, 108 pp.

McWhorter, D. B., 1972, Steady and unsteady flow of freshwater in saline aquifers: Fort Collins, Colorado, Colorado State University, Water Management Technical Report no. 20.

Meissner, U., 1973, A mixed finite element model for use in potential flow problems, Int. J. Numer. Methods Eng., 6, 467-473.

Mercer, J. W., Larson, S. P., Faust, G. R., 1980, Simulation of saltwater interface motion: Ground Water, v. 18 (4), p. 374-385.

Muskat, M.,, 1937, The flow of homogeneous fluids in porous media: New York, McGraw-Hill, 763 pp.

Neuman, S. P., and Witherspoon, P. A., 1969, Theory of flow in a confined two-aquifer system: Water Resources Research, 5(4), p. 803.

Pinder, G. F., and Cooper, H. H., 1970, A numerical technique for calculating the transient position of the saltwater front: Water Resources Research, 6(3), p. 875-882.

Pinder, G. F., and Page, R. H., 1976, Finite element simulation of saltwater intrusion on the south Fork of Long Island: Proc. of the First International Conference on Finite Elements in Water Resources, Princeton University.

Pinder, G. F., and Gray, W. G., 1977, Finite element simulation in surface and subsurface hydrology, Academic Press, New York.

Rubin, H., and Pinder, G. F., 1977, Approximate analysis of upconing: Advances in Water Resources, v. 1, no. 2, p.97-101.

Rubin, H., 1983, On the application of the boundary layer model for the simulation of density stratified flows in aquifers: Advances in Water Resources, v. 6, p.96-105.

Rushton, K. R., 1980, Differing positions of saline interfaces in aquifers and observation boreholes: J. Hydrol., 48, p.185-189.

Schalla, R., 1986, A comparison of the effects of rotary wash and air rotary drilling techniques on pumping test results: Proceedings Sixth National Symposium and Exposition on Aquifer Restoration and Ground Water Monitoring, Columbus, Ohio.

Schoewe, W. A., 1949, The geography of Kansas, part II-physical geography: Trans. Kansas Academy of Science, 52, p.261-333.

Segol, G., and Pinder, G. F., 1976, Transient simulation of saltwater intrusion in southeastern Florida: Water Resources Research, 12(1), p. 65-70.

Segol, G., Pinder, G. F., and Gray, W. G., 1975, A Galerkin finite element technique for calculating the transient position of the saltwater front: Water Resources Research, 11(2), p. 343-347.

Shamir, U., and Dagan, G., 1971, Motion of the seawater interface in coastal aquifers: a numerical solution: Water Resources Research, 7(3), p. 644-657.

Tellam, J. H., Lloyd, J. W., and Walters, M., 1986, The morphology of a saline groundwater body: its investigation, description, and possible explanation: J. Hydrol., 83, p.1-21.

Van Dam, J. C. and Meulenkamp, J. J., 1976, Some results of the geo-electrical resistivity method in ground water investigations in The Netherlands. Geophys. Prospect. XV(1).

Van Dam, J. C., and Sikkema, P. C., 1982, Approximate solution of the problem of the shape of the interface in a semi-confined aquifer: Journal of Hydrology, 56, p. 221-237.

Voss, C. I., 1984, A finite element simulation model for saturated-unsaturated fluid-density-dependent ground-water flow with energy transport or chemically reactive single-species solute transport: U.S. Geological Survey Water Resources Investigations Report 84-4369.

Whittemore, D. O., Basel, C. L., Galle, O. K., and Waugh, T. C., 1981, Geochemical identification of saltwater sources in the Smoky Hill River valley, McPherson, Saline, and Dickinson counties, Kansas: Final report for U.S. Army Corps of Engineers, Kansas City District.

Zeller, D. E. (ed), 1968, The stratigraphic succession of Kansas: Kansas Geological Survey, Bulletin 189, 81 pp.

Zohdy, A. A. R., 1973, A computer program for the automatic interpretation of Schlumberger sounding curves over horizontally stratified media: U.S. Department of Commerce, NTIS Report USGS-GD-74-017, 31pp.

Zohdy, A. A. R., and Jackson, D. B., 1973, Recognition of natural brine by electrical soundings near the Salt Fork of the Brazos River, Kent and Stonewall counties, Texas: U.S. Geological Survey, Prof. Paper 809-A, 14pp.